AD________________

Award Number: W81XWH-04-1-0554

TITLE: A New Flat-Panel Digital Mammography Detector with Avalanche Photoconductor and High-Resolution Field Emitter Readout

PRINCIPAL INVESTIGATOR: Wei Zhao, Ph.D.

CONTRACTING ORGANIZATION: The Research Foundation of the
State University of New York
Stony Brook, NY 11794-3362

REPORT DATE: June 2005

TYPE OF REPORT: Annual

PREPARED FOR: U.S. Army Medical Research and Materiel Command
Fort Detrick, Maryland 21702-5012

DISTRIBUTION STATEMENT: Approved for Public Release;
Distribution Unlimited

REPORT DOCUMENTATION PAGE

Form Approved
OMB No. 074-0188

1. AGENCY USE ONLY

2. REPORT DATE
June 2005

3. REPORT TYPE AND DATES COVERED
Annual (15 May 2004 - 14 May 2005)

4. TITLE AND SUBTITLE
A New Flat-Panel Digital Mammography Detector with Avalanche Photoconductor and High-Resolution Field Emitter Readout

5. FUNDING NUMBERS
W81XWH-04-1-0554

6. AUTHOR(S)

Wei Zhao, Ph.D.

7. PERFORMING ORGANIZATION NAME(S) AND ADDRESS(ES)
The Research Foundation of the
State University of New York
Stony Brook, NY 11794-3362

E-Mail: wei.zhao@sunysb.edu

8. PERFORMING ORGANIZATION REPORT NUMBER

9. SPONSORING / MONITORING AGENCY NAME(S) AND ADDRESS(ES)
U.S. Army Medical Research and Materiel Command
Fort Detrick, Maryland 21702-5012

10. SPONSORING / MONITORING AGENCY REPORT NUMBER

11. SUPPLEMENTARY NOTES

12a. DISTRIBUTION / AVAILABILITY STATEMENT
Approved for Public Release; Distribution Unlimited

12b. DISTRIBUTION CODE

13. ABSTRACT (Maximum 200 Words)

A new concept of flat-panel imager (FPI) with avalanche gain and high resolution (with 50 micron pixel size) is being investigated for improving the imaging performance of digital mammography at low dose and high spatial frequencies, which are critical for the detection of subtle breast abnormalities and the development of digital tomosynthesis. The detector employs an avalanche photoconductor - amorphous selenium (a-Se), called HARP, to detect and amplify the optical signal generated by a structured scintillator - cesium iodide (CsI), and form a charge image that is read out by a high-resolution field emitter array (FEA). We call the proposed detector SAPHIRE (Scintillator-Avalanche Photoconductor with High Resolution Emitter readout). Our investigation showed that the avalanche gain of SAPHIRE permits the use of high resolution (HR) type CsI, which has not been used in existing FPI due to its low light output. HR CsI can provide better imaging performance at high spatial frequencies than existing digital mammography detectors. We also investigated the factors affecting the resolution of the FEA readout method. Our results showed that the dominant source of image blur is the spread of the FEA electron beam. The results of our calculation showed that an effective pixel size of 50 microns is feasible.

14. SUBJECT TERMS
digital mammography, tomosynthesis, three-dimensional mammography

15. NUMBER OF PAGES
80

16. PRICE CODE

17. SECURITY CLASSIFICATION OF REPORT	**18. SECURITY CLASSIFICATION OF THIS PAGE**	**19. SECURITY CLASSIFICATION OF ABSTRACT**	**20. LIMITATION OF ABSTRACT**
Unclassified	Unclassified	Unclassified	Unlimited

NSN 7540-01-280-5500

Standard Form 298 (Rev. 2-89)
Prescribed by ANSI Std. Z39-18
298-102

Table of Contents

INTRODUCTION:

A new concept of flat-panel imager (FPI) with avalanche gain and high resolution (with 50 micron pixel size) is being investigated for improving the imaging performance of digital mammography at low dose and high spatial frequencies, which are critical for the detection of subtle breast abnormalities and the development of digital tomosynthesis. The detector employs an avalanche photoconductor – amorphous selenium (a-Se), which is called HARP, to detect and amplify the optical signal generated by an x-ray scintillator with needle structure - cesium iodide (CsI), and form a charge image that is read out by a high-resolution field emitter array (FEA). We call the proposed detector SAPHIRE (Scintillator-Avalanche Photoconductor with High Resolution Emitter readout). Our objective is to investigate the feasibility of SAPHIRE and demonstrate its potential advantages over existing detector technology.

BODY:

The following tasks were proposed in the approved Statement of Work. The results of our investigation in the first year are summarized as follows:

TASK 1: Determine the optimal CsI-HARP combination for mammography, Month 1-24

a. Develop a linear system model for SAPHIRE, so that the imaging performance of different CsI-HARP combination can be predicted. Month 1-6

A cascaded linear system model was developed for SAPHIRE in order to determine whether it is advantageous to use high resolution (HR) type CsI, which has not been used in existing FPI due to its low light output. Since the avalanche gain of HARP can compensate for the low light output, HR CsI can potentially provide better imaging performance at high spatial frequencies than the high light (HL, optimized for light output) CsI used in existing digital mammography detectors. Experimental measurements of HR and HL type CsI samples with the same thickness (150 micorns for mammography) showed that HR CsI has higher resolution and less depth dependent image blur, at the cost of lower light output (60 % of HL). This resulted in superior detective quantum efficiency (DQE) at high spatial frequencies for the HR CsI. This work is described in detail in a Med. Phys. paper (manuscript 1).

b. Make a test system for experimental measurement of the imaging performance of CsI-HARP combination using a HARP tube with fiber optic faceplate. Month 1-12

We made progress in the following two aspects: 1. the first HARP tube with FOP faceplate was built, which allows us to put a CsI in direct contact with HARP without loss of light or spatial resolution for investigating the imaging performance of the scintillator (CsI)-HARP combination. The first FOP-HARP has a HARP layer thickness of 4 μm. Figure 1 (a) shows the microscopic view of the FOP target surface after optical polishing (which cleans the surface but does not remove the surface variation, i.e. bumps). The "chicken-wire" pattern of FOP is clearly visible. Figure 1 (b) shows the first optical image made with the FOP-HARP tube under an avalanche gain of 20. The result from the first FOP-HARP tube is very encouraging despite the large number of defects. We expect significant reduction in the number of defects after mechanical polishing is applied to the FOP for the next prototype. 2. Theoretical investigation of the imaging performance of the scintillator HARP (SHARP) combination is performed to determine the optimal design parameters and operational conditions for the HARP layer. We found that a HARP layer with thickness of 4-8 μm will provide adequate avalanche gain and quantum efficiency for x-ray quantum noise limited performance down to a single x-ray photon. We also showed that a HARP layer thickness variation of < 2 % is desirable to maintain a uniform avalanche gain. Direct x-ray interaction in HARP was shown not to affect image quality. This work was presented at the 2005 SPIE Medical Imaging Conference (manuscript 2). A reprint of the paper is attached to this report. An expanded version of this paper has been submitted to Med. Phys. for review. (manuscript 3).

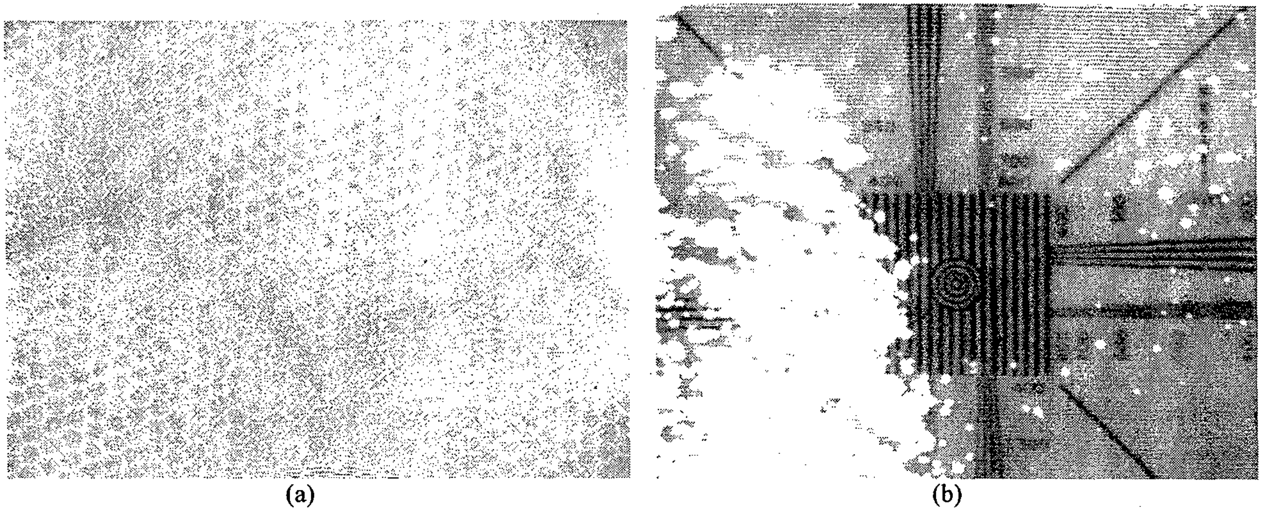
(a) (b)

Figure 1: (a) Micrograph of the FOP target surface after optical polishing. The surface variation is estimated to be 0.6 μm. (b) Optical image of a resolution target made by the FOP-HARP tube. Defects are most likely due to surface variations on the FOP that caused local high field and breakdown of the blocking layer. Mechanical polishing or planarization techniques are under development.

c. Measure the x-ray imaging performance of CsI-HARP using CsI of different types and thickness, and determine the optimal CsI-HARP combination. Month 13-24

TASK 2: Investigate the factors affecting the spatial resolution of the FEA readout method, Month 1-36

a. Develop an electric field simulation for the electron optics of SAPHIRE to calculate the electron beam trajectory for FEA readout method. Month 1-12

We performed preliminary theoretical investigation of the factors affecting the resolution of the FEA readout method. Our results showed that the dominant source of image blur for the FEA readout method is the spread of the electron beam. The magnitude of electron spreading depends on the following factors of the SAPHIRE design: (1) emission angle of the electrons from the FEA; (2) design of electron-optics for focusing of electron beam; (3) operating potential of the FEA; and (4) the distance between the FEA and the HARP layer. The results of our preliminary calculation showed that incorporating a mesh electrode half way between the FEA and the HARP target can reduce the electron beam spread, and an effective pixel size of 50 - 100 microns is possible. Shown in Figure 2 are the calculated electron beam spread as a function of: (a) the distance between the gate of the FEA and the HARP target; and (b) the bias potential on the mesh electrode. It shows that to minimize blur for a pixel size of 50 μm, an electron beam spread of 20 μm or less is desirable. This translate to a HARP to FEA distance of 0.4 mm and a meash electrode bias potential of 350 V. This short distance with high potential on the mesh will pose tremendous challenge to the assembly of the detector. We are currently exploring new electron optics design that permits larger distance between FEA and HARP through electron optical simulation. This work will be presented at the upcoming AAPM annual conference.

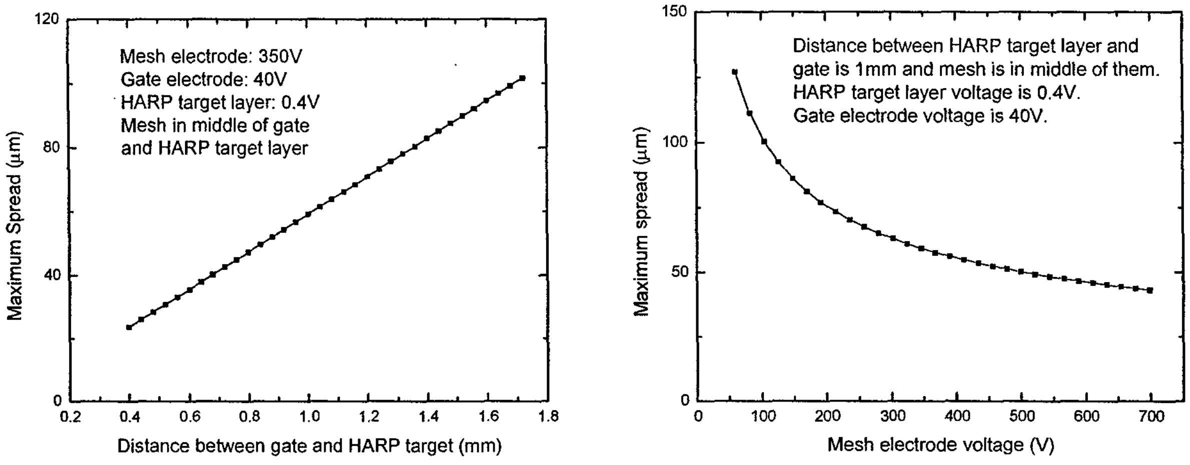

(a) (b)

Figure 2 Calculated maximum electron beam spread as a function of: (a) distance between the gate of the FEA and the HARP target, and (b) the bias potential for the mesh electrode.

b. Determine the optimal mesh electrode configuration that results in the highest spatial resolution. Month 13-18
c. Refine optimal mesh electrode configuration in connection with the noise model. Month 19-21
d. Calculate the spatial resolution due to FEA readout for the prototype detector to verify experimental measurement. Month 25-36

TASK 3: Investigate the factors affecting the electronic noise and readout speed, Month 1-21

a. Investigate the factors affecting the readout speed of SAPHIRE and determine the readout time as a function of the number of ITO stripes and characteristics of charge amplifier ASIC. Month 7-12
b. Investigate the factors affecting the electronic noise and develop a noise model based on the properties of charge amplifiers, the number of divided ITO stripes, the readout speed and the electron optics design. Month 13-18
c. Optimize the number of stripes and the mesh electrode configuration so that the best noise performance and adequate readout speed can be achieved. Month 19-21

TASK 4: Demonstrate the practical feasibility of SAPHIRE by building a small area prototype detector, Month 22-36

a. Construct the small area prototype detector according to the optimal mesh electrode configuration determined from TASK 3. Month 22-24
b. Evaluate the optical imaging performance of the prototype detector without CsI at the input. Month 25-27
c. Evaluate the x-ray imaging performance of the prototype detector with CsI coupled to the input. Month 28-36

KEY RESEARCH ACCOMPLISHMENTS:

- Developed a cascaded linear system model for SAPHIRE.
- Investigated the imaging performance of CsI layers made with different manufacturing techniques, and determined that the CsI optimized for high resolution (HR) can provide better DQE at higher spatial frequencies required for mammography.
- Investigated the HARP design parameters that affect the imaging performance of CsI-HARP combination, and determined the avalanche gain required to produce x-ray quantum noise limited performance for digital tomosynthesis.
- Performed preliminary investigation of the factors affecting the image resolution of SAPHIRE.

REPORTABLE OUTCOME:

Manuscripts:

1. Wei Zhao, G. Ristic and J. A. Rowlands, "Inherent Imaging Performance of Cesium Iodide Scintillators", Med. Phys. **31**, 2594-2605 (2004)
2. Wei Zhao, Dan Li, Alla Reznik, B. J. M. Lui, D. C. Hunt, Kenkichi Tanioka and J. A. Rowlands, "Indirect flat-panel detectors with avalanche gain: Design and operation of the avalanche photoconductor", Proc. SPIE **5745**, 352-360 (2005)
3. Wei Zhao, Dan Li, Alla Reznik, B. J. M. Lui, D. C. Hunt, J. A. Rowlands, Yuji Ohkawa and Kenkichi Tanioka, "Indirect flat-panel detector with avalanche gain: Fundamental feasibility investigation for SHARP-AMFPI (Scintillator HARP Active Matrix Flat Panel Imager)", Med. Phys. (submitted)

Conference presentations:

1. Wei Zhao, K. Tanioka, D. C. Hunt and J. A. Rowlands, "A new flat-panel detector for low dose digital x-ray imaging", IEEE Medical Imaging Conference, October, 2004, Rome, Italy

CONCLUSIONS

During the first year of our research support by Army BCRP, we have focused our investigation on the understanding of the factors affecting the imaging performance of SAPHIRE. The imaging performance of different CsI layers demonstrated that CsI optimized for HR can provide between DQE at high spatial frequencies and is more suitable for mammography. Investigation using our cascaded linear system model of SAPHIRE showed that the avalanche gain of a 4-8 μm thick HARP layer is sufficient to provide x-ray quantum noise limited performance for digital tomosynthesis (using the HR CsI layers). Our preliminary calculation of the maximum electron beam spreading of the FEA readout shows that a pixel size of 50 – 100 μm is possible.

REFERENCES

APPENDIX 1

X-ray imaging performance of structured cesium iodide scintillators

Wei Zhao[a]
Department of Radiology, State University of New York at Stony Brook, L-4 Health Sciences Center, Stony Brook, New York 11794-8460

Goran Ristic and J. A. Rowlands
Imaging Research, Sunnybrook and Women's College Health Sciences Centre, Department of Medical Biophysics, University of Toronto, 2075 Bayview Avenue, Toronto, Ontario M4N 3M5, Canada

(Received 16 March 2004; revised 20 May 2004; accepted for publication 23 June 2004; published 26 August 2004)

Columnar structured cesium iodide (CsI) scintillators doped with Thallium (Tl) have been used extensively for indirect x-ray imaging detectors. The purpose of this paper is to develop a methodology for systematic investigation of the inherent imaging performance of CsI as a function of thickness and design type. The results will facilitate the optimization of CsI layer design for different x-ray imaging applications, and allow validation of physical models developed for the light channeling process in columnar CsI layers. CsI samples of different types and thicknesses were obtained from the same manufacturer. They were optimized either for light output (HL) or image resolution (HR), and the thickness ranged between 150 and 600 microns. During experimental measurements, the CsI samples were placed in direct contact with a high resolution CMOS optical sensor with a pixel pitch of 48 microns. The modulation transfer function (MTF), noise power spectrum (NPS), and detective quantum efficiency (DQE) of the detector with different CsI configurations were measured experimentally. The aperture function of the CMOS sensor was determined separately in order to estimate the MTF of CsI alone. We also measured the pulse height distribution of the light output from both the HL and HR CsI at different x-ray energies, from which the x-ray quantum efficiency, Swank factor and x-ray conversion gain were determined. Our results showed that the MTF at 5 cycles/mm for the HR type was 50% higher than for the HL. However, the HR layer produces $\sim$36% less light output. The Swank factor below K-edge was 0.91 and 0.93 for the HR and HL types, respectively, thus their DQE(0) were essentially identical. The presampling MTF decreased as a function of thickness L. The universal MTF, i.e., MTF plotted as a function of the product of spatial frequency f and CsI thickness L, increased as a function of L. This indicates that the light channeling process in CsI improved the MTF of thicker layers more significantly than for the thinner ones. © *2004 American Association of Physicists in Medicine.* [DOI: 10.1118/1.1782676]

Key words: indirect detection, flat-panel detectors, digital radiography, cesium iodide, Swank factor

I. INTRODUCTION

Indirect flat-panel imagers (FPI) have been in widespread clinical use for digital x-ray imaging for several years. They use a scintillator to convert the incident x-ray energy to optical photons, which are then converted to electronic signal and read out with a large area integrated circuit with an amorphous silicon (a-Si) photodiode and a thin film transistor (TFT) at each pixel.[1] Although the majority of indirect FPIs use structured cesium iodide (CsI) layers as the x-ray converter, powder phosphor screens are also being used because of its lower cost. Unlike the sodium (Na) doped CsI used in x-ray image intensifiers (XRII), the CsI layers used in FPI are exclusively doped with Thalium (Tl) because they are less hygroscopic and the emission spectrum (green) is better matched to the spectral sensitivity of the a-Si photodiodes. In the remainder of this paper, CsI refers to Tl doped layers unless otherwise specified.

Comparative studies between CsI and powder phosphor based FPI have been performed for both general radiographic[2] and mammographic[3] imaging applications. The results demonstrated that CsI provides better detective quantum efficiency (DQE) than powder phosphors over all spatial frequencies. This is because the columnar structure of CsI helps channel light in the forward direction. Hence the thickness can be increased while maintaining a modulation transfer function (MTF) comparable to phosphors. Although the imaging performance of complete detectors incorporating CsI has been reported,[4,5] there is a lack of systematic study of the imaging performance of CsI alone as a function of its design parameters, e.g., thickness. Understanding the relationship between physical parameters of CsI and its imaging performance is paramount for optimization of indirect flat-panel detectors for different x-ray imaging applications. The reason for pursuing a fundamental understanding of the imaging performance of CsI is that although CsI has been widely used in commercial flat-panel detectors, the techniques for making the layers and their relationship with imaging properties have largely remained trade secrets. There is a lack of physical characterization of CsI layers (without

TFT arrays) and basic understanding of its image formation process, which is needed to determine the optimal CsI thickness for a particular x-ray imaging application. In addition to the different thicknesses, commercially available CsI layers are of two different types: one optimized for high resolution (HR) and the other for high light output (HL).[6] The overall imaging property of CsI is best measured by its spatial frequency dependent DQE, which is mainly determined by five factors: (1) The quantum detection efficiency (QDE), which depends on the thickness of the layer and the incident x-ray energy; (2) the x-ray-to-photon conversion gain, which governs the detector performance at low dose; (3) the Swank factor, which describes the added noise in the conversion process and is directly proportional to DQE(0);[7] (4) the overall spatial resolution expressed as MTF; and (5) the depth dependent blur, which arises because light generated at the x-ray entrance side of the scintillator experiences more scatter before reaching the exit surface and more blur results. Lubberts showed that depth dependent blur results in degradation of DQE(*f*) at high spatial frequencies for powder phosphors.[8] Compared to powder phosphors, the columnar structure in CsI helps channel light in the forward direction which may result in less depth dependent blur. However, the light channeling in CsI is not perfect as implied by a fiber optic-like model. It has been shown that blurring in CsI is increased with thickness just as in powder phosphor screens,[6] albeit not as much. We have performed preliminary work on developing a model for the light scatter/channeling process in CsI so that its depth dependent blur can be predicted.[9] Compared to the isotropic scatter in powder phosphor, the structured phosphor layer was modeled to have nonisotropic scatter with a preferred direction normal to the surface of the phosphor layer. We found that the MTF of a structured phosphor was comparable to a powder phosphor screen of half the thickness. Thus the established analytical models for powder phosphors by Swank[10] can be used for structured phosphors provided the effective thickness is modified appropriately. We found reasonable agreement between modeled and previously published experimental measurements of MTF. Others have developed Monte Carlo techniques to simulate the light channeling process in CsI.[11] In order to validate these modeling and simulation techniques, systematic investigation of the imaging performance of CsI with different thicknesses and light output is needed. For our present investigation, we obtained CsI samples of four different thicknesses from the same manufacturer (Hamamatsu Photonics Corporation) for maximum consistency in material properties. Only one of the thicknesses was available in both HR and HL types, and the rest were of HL type. In this paper, we will present our experimental measurements of these CsI samples. The imaging properties measured include: (1) The mass loading which determines the QDE; (2) the Swank factor and x-ray conversion gain obtained using pulse height spectroscopy (PHS); (3) MTF; and (4) DQE as a function of spatial frequency. We also developed a simplified linear systems model for CsI which did not include the Lubberts effect, i.e., depth dependent blur. By comparing the modeled results with experiments, we obtained qualitative information on the significance of the Lubberts effect in different CsI samples. We believe these results will facilitate fundamental understanding of the light channeling process in CsI; aid in the validation of different modeling and simulation techniques; and eventually lead to optimization of CsI parameters for different x-ray imaging applications.

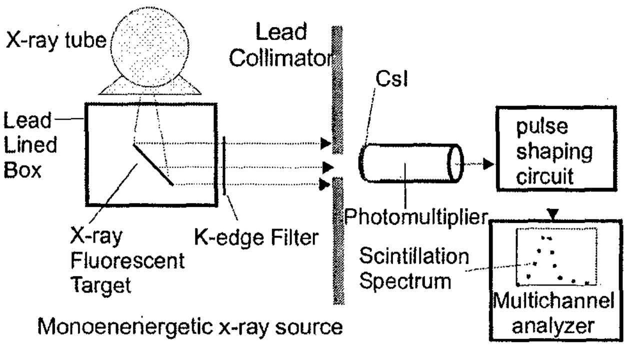

FIG. 1. Experimental setup for the pulse height spectroscopy (PHS) measurements of CsI samples.

II. MATERIAL AND METHODS

A. X-ray absorption and Swank factor

1. X-ray absorption and determination of mass loading

The density of structured CsI layers is not well documented, and it varies between manufacturers. Based on existing documentation, the packing density of structured CsI is ~75%.[12] The nominal thicknesses of the samples used in our experiments were 150, 300, 450, and 600 μm. Both HL and HR types were obtained for 150 μm thick samples. The CsI layers were deposited on fiber optic faceplates (FOP), and are referred to as fiber optic scintillator (FOS) plates. The FOP substrates have a fiber diameter of 6 μm, and they are identical for the HL and HR type CsI. The top surface of each CsI layer is coated with a protective layer to seal it from moisture.[6] In order to accurately determine the x-ray absorption of the samples, we measured PHS of the CsI layers for incident x-ray photons of different energies, the results of which were also used to determine the Swank factor. Shown in Fig. 1 is our experimental apparatus, which includes a photomultiplier tube (PMT) to detect the light output of the FOS plates. The electronic signal at the output of the PMT (Model R6095, Hamamatsu Photonics Corporation) was fed to a charge amplifier followed by a pulse-shaping amplifier. The final output signal was fed to a multi-channel analyzer so that a PHS could be obtained. Monoenergetic x-rays were used, which were generated by K-fluorescence from selected elements. Each PHS was integrated to obtain the total number of x-rays detected by a CsI sample. We also measured the PHS of a 4 mm NaI (Tl) crystal, which absorbs essentially all the incident x-ray photons and provided an estimate of the number of incident x-ray photons. The ratio between the number of photons obtained using each CsI sample and using the NaI crystal gave the QDE η. The η values for each x-ray incident energy E was then fitted to the expression

$$\eta = 1 - \exp\left[-\frac{\mu(E)}{\rho} d \right], \tag{1}$$

where $\mu(E)/\rho$ is the mass attenuation coefficient of CsI for energy E and d is the mass loading or surface density of the CsI layer given in g/cm^2. Since experimental error with bigger η values (with lower E) results in a greater error in the determination of d than for lower η, a weighting function of $1/\eta$ was used in the curve fitting procedure. The best fitted d value gives the mass loading of the CsI sample.

2. Conversion gain and Swank factor

It has been shown previously that the conversion gain of HR type CsI is less than that of the HL type.[3] This has a significant impact on the imaging performance of flat-panel detectors at low dose. Hence we focused on the gain difference between the HR and HL type CsI layers. Since the x-ray conversion gain in NaI crystals is known, by comparing the PHS of CsI and NaI at the same incident x-ray energy E, we can obtain the conversion gain of the CsI samples. The Swank factor A_S can be obtained from the PHS measurements using[7,13]

$$A_S = \frac{m_1^2}{m_0 m_2}, \tag{2}$$

where m_0, m_1, and m_2 are the zeroth, first, and second moments of the PHS, respectively.

The Swank factor describes the distribution of the number of optical light photons produced by x-ray photons for a given incident x-ray energy distribution and characterizes the noise associated with the x-ray to light conversion process. At each x-ray energy, the Swank factor can be separated into two multiplicative factors:[13]

$$A_S = I_{\mathrm{OPD}} I_{\mathrm{AED}}, \tag{3}$$

where I_{OPD} describes the optical component of A_S due to unequal light losses from different parts of the CsI layer because of different propagation lengths, and I_{AED} describes the absorbed energy distribution for the incident x-ray photons, which is mainly due to K-fluorescent escape and reabsorption. I_{OPD} can usually be assumed to be x-ray energy independent, whereas I_{AED} depends strongly on incident x-ray energy.[13] While we assume I_{OPD} in our FOS samples depends mainly on the properties of the CsI layer, the FOP could also affect I_{OPD} if the acceptance angle of the FOP is small and the angular distribution of light from CsI is depth dependent. Since the FOP used in our FOS samples has a numerical aperture of 1,[6] we expect the effect of FOP to be negligible. I_{AED} for a given x-ray detector material can be calculated numerically by dividing the thickness of the material into many thin layers.[14] The K-fluorescent photons generated from each sub-layer are assumed to be isotropic, so that the probability of reabsorption can be calculated by integrating the number of reabsorbed photons at each solid angle and depth. Then a simulated PHS can be generated with the main peak representing the total energy absorption in the material (including K-fluorescence reabsorption) and a second (lower) peak representing K-fluorescent escape. A Poisson distributed noise can then be added to each peak. Then the moments (m_0, m_1, and m_2) of the simulated PHS are calculated and I_{AED} determined using Eq. (2). This method has been used in the theoretical calculation of I_{AED} for phosphor screens,[15] CsI in image intensifiers[7] and amorphous selenium x-ray photoconductors.[16] After I_{AED} is calculated, we can obtain an estimate of I_{OPD} from the measured Swank factor A_S. This information is important for understanding the optical properties of different CsI layers.

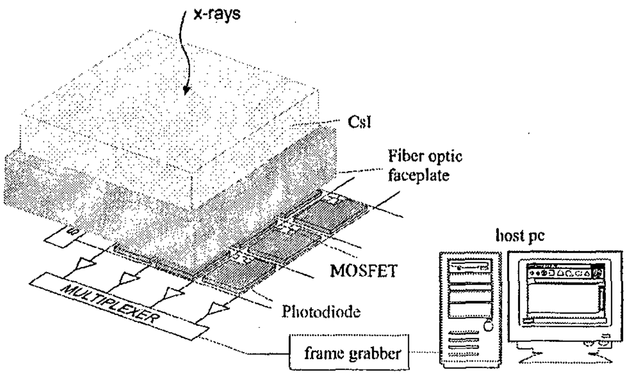

FIG. 2. Diagram showing the CMOS image sensor and image acquisition system used to measure the MTF, NPS, and DQE of CsI layers. The FOP side the CsI samples were placed in direct contact with the CMOS sensor (thickness of different layers not drawn to scale).

3. DQE at zero spatial frequency

It is difficult to obtain a precise measurement of DQE(0) from the measurement of spatial frequency dependent DQE(*f*) (Sec. II C). This is because the DC component of the noise images used to compute NPS is subtracted before the Fourier transformation is applied. An estimate of DQE(0) is usually obtained by extrapolation of the DQE(*f*) curve near zero spatial frequency. Our independent measurement of η and A_S provided a more straightforward method for determining DQE(0) using

$$\mathrm{DQE}(0) = \eta A_S. \tag{4}$$

The DQE(0) obtained using this method is for monoenergetic x-rays. DQE(0) for a broad x-ray spectrum can then be estimated using the mean energy of the entire spectrum.

B. MTF

The MTF of CsI samples was measured using a two-dimensional array of CMOS optical sensor with a MOSFET switch and a photodiode at each pixel. The design and performance of the CMOS sensor were described in detail elsewhere.[17] It has a pixel pitch of 48 μm and an active area of 24.5 mm×49.0 mm. The active area of each photodiode is 43 μm×43 μm, yielding a pixel fill-factor of ~80%. The FOP side of each CsI sample was placed in direct contact with the surface of the CMOS sensor, as shown in Fig. 2. Hence the imaging geometry is similar to an indirect flat-panel detector. The FOP substrate for each CsI sample is

3 mm thick. It absorbs 99% of the radiation that transmits through the CsI layer,[6] hence direct x-ray interaction in the CMOS sensor is negligible. The output of the CMOS sensor was fed to a frame grabber in a PC. The presampling MTF of the CsI-CMOS combination was measured using the slanted slit technique.[18] A 10 μm wide slit made of 1.5 mm thick tungsten sheet was used in the experiments. The slit was placed at an angle ~2° from the gate- or data-lines of the CMOS sensor. An x-ray image of the slit was taken, and the image was corrected for offset and gain nonuniformity, as well as nonresponsive pixels. The maximum pixel value of each image line (perpendicular to the slit) was determined so that those pixels centered on the slit could be located. Their location was then fitted to a straight line in order to determine the position of the slit on the image. Depending on the point of intersection between the slit and the pixels, the image data for each line of the image were placed into four different bins. The image data from the four bins were then interleaved to produce a four times oversampled line spread function LSF. Then the data for the baseline of the LSF, i.e., data less than 1% of the maximum value of the LSF, were fitted with a single exponential decay function. This reduces the noise for subsequent Fourier transform of the LSF, which produces the MTF. In order to determine the MTF of the CsI samples alone, the slanted slit was also imaged directly with the CMOS sensor (without CsI in place) using x-rays. This allows determination of a correction MTF due to the focal spot blur, the width of the slit and the aperture function of the CMOS sensor. The correction MTF was then divided into the presampling MTF of the entire imaging system to obtain the MTF due to CsI alone.

C. DQE measurement

The 2D NPS of the CsI-CMOS imaging system was measured as a function of x-ray exposure. An RQA5 x-ray spectrum was used, which was generated with a Tungsten tube operated at 70 kVp (using a high frequency generator) and filtered with 21 mm of aluminum (Al). The measured HVL of the beam was 7.1 mm of Al. The linearity of the detector was measured within the exposure range of 0.14–20.9 mR, from which the x-ray sensitivity k_0 was determined. At each x-ray exposure level, 100 x-ray images and dark frames were acquired. The average of the dark frames formed the offset image, which was subtracted from the average of the 100 x-ray images to obtain a gain correction table. A defect-free region of interest (ROI) containing 128×128 pixels was chosen for the NPS calculation. Each of the 100 x-ray images was offset and gain corrected, and the mean of each noise image subtracted. A two-dimensional (2D) Fourier transform was then performed on each corrected noise image and the results were averaged to obtain a 2D NPS.[19] Seven lines on either side of the central axes (not including the axes) of the 2D NPS were used to compute the one-dimensional (1D) NPS.[19] The frequency of each data point within this region was calculated using $f = \sqrt{u^2+v^2}$. Although our method of gain correction introduced a small amount of correlation between each noise image and the gain correction table (~1%), it is within the experimental error of the determination of NPS and is therefore neglected.[20]

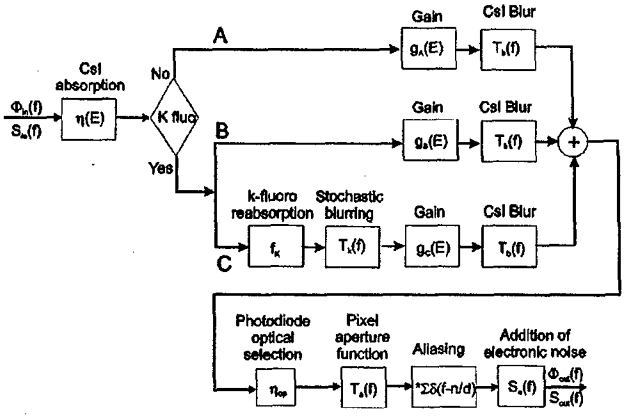

FIG. 3. Imaging stages of the simplified cascaded linear system model for the CsI-CMOS combination.

D. DQE model

We adapted a linear system model developed for indirect flat-panel detectors.[21] Since the x-ray spectrum used in our experiments was 70 kVp, we added the effect of K-fluorescence reabsorption.[22] The imaging stages involved in the model are shown in Fig. 3. The path corresponding to K-fluorescence reabsorption included fluorescent photons from both Cs and I atoms. We assumed that if a K-fluorescence photon interacts with the material, the energy is completely reabsorbed at the interaction site. Since the K-Beta fluorescence photon for Cs is above the K-edge of I, 3% and 4% of the photons above the K-edge of Cs could generate a second K-fluorescence depending on the thickness of CsI, however, this was ignored in our calculations. The overall error caused by the omission on the MTF and DQE should be negligible. For the present paper, we also ignored the Lubberts effect in our linear system model. By comparing modeled results to experimental measurement of DQE, we can obtain a qualitative assessment of the importance of Lubberts effect in different CsI layers.

III. RESULTS AND DISCUSSION

A. X-ray absorption and Swank factor

1. X-ray absorption and determination of mass loading

Shown in Fig. 4 is the measurement of QDE η of the 150 μm HL type CsI layer as a function of the incident x-ray energy E. Plotted in the same graph is the calculated QDE using the fitted mass loading d of the same CsI layer, which was determined as 55 mg/cm^2. The quality of fitting is excellent. Table I summarizes the fitted mass loading d for all the CsI layers used in our experiments. Shown in the same table is the mass loading determined from weight measurements provided by the manufacturer for each CsI sample.

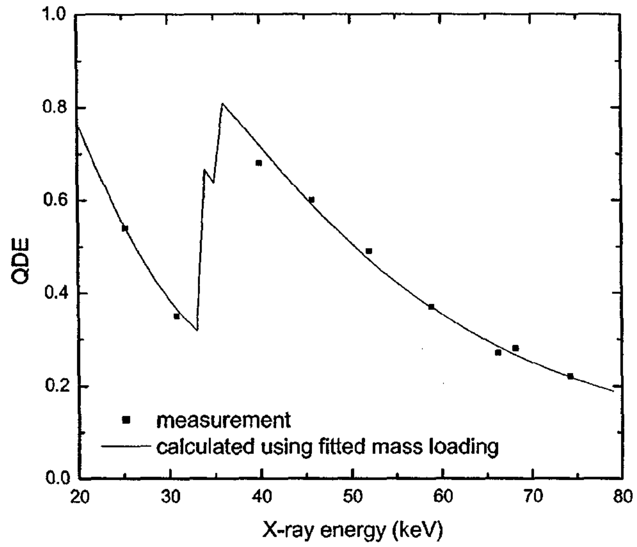

Fig. 4. Comparison of experimentally measured quantum detection efficiency (QDE) as a function of x-ray energy for the 150 HR CsI layer and the calculated QDE using the fitted mass loading 55 mg/cm^2.

The mass loading determined from our x-ray measurement is in good agreement with the manufacturer's weight measurement. Compared to the 150 μm layers, the mass loading for the 300 μm layer is less than what is expected from its doubled thickness. The most noticeable fact is that the 450 and 600 μm layers have very little difference in their mass loading. This is, however, within the manufacturers tolerance of ±10%. If we assume a constant density of 3.38 g/cm^3 (i.e., 75% packing density), the thickness L of different samples can be estimated from the measured mass loading and the results are shown in Table I.

2. Conversion gain and Swank factor

Shown in Fig. 5 are the PHS measured at $E = 31$ keV for the 150 μm HR and HL CsI layers, as well as the NaI crystal. The relative position of the peak of each PHS determines the conversion gain difference between these three samples. Since E is lower than the K-edge of CsI, there is only one peak in the PHS of CsI. The conversion gain of the HR type is ~64% of the HL type. This ratio is higher than that (~50%) observed in a previous study,[3] which could simply be due to variation between samples. The position of the PHS peak for the HL type CsI is ~47% of that for the NaI crystal but before direct comparison this has to be corrected for the different spectral outputs of the NaI and CsI. The accepted light yield in NaI for gamma rays is ~40 photons/keV,[23] which means that the energy required to generate a light photon is $W = 25$ eV. Shown in Fig. 6 are previously published emission spectra for both NaI (Tl) and CsI (Tl).[24] The peak of the spectra is 415 nm and 530 nm for NaI and CsI, respectively.[23] The quantum efficiency (QE) of the PMT used in our experiments[25] is also plotted as a function of wavelength in Fig. 6. It shows that the optical QE of PMT is better matched to the emission spectrum of NaI. We calculated the average QE of the PMT for each emission spectrum by integrating the product of light intensity and QE over the whole spectrum and normalized it to the total number of integrated light photons. Our results showed that the average QE of the PMT for the emission spectra of NaI and CsI are 20.3% and 10.8%, respectively. This information combined with the positions of the PHS peak for NaI and CsI in Fig. 5 leads to the conclusion that the effective W for the HL CsI FOP is ~28 eV. Since the FOP substrate of the CsI transmits only ~60% of the light emitted from CsI,[6] the W associated with the inherent conversion gain of HL CsI is ~17 eV. This is in good agreement with previously published values for columnar CsI.[26]

Shown in Fig. 7 are the PHS of the 150 μm HR CsI layer at different x-ray incident energies. For E above the K-edge of CsI, there are two peaks on the PHS, with the lower one corresponding to the x-ray interaction events with the escape of K-fluorescence. The moments of the PHS were calculated so that the Swank factor could be determined using Eq. (2). Shown in Fig. 8(a) is the calculated Swank factor A_S plotted as a function of E for the 150 μm HR layer and also the calculated I_{AED} using its measured mass loading of 55 mg/cm^2. The I_{AED} is unity below the K-edge because there is no K-fluorescence escape. Above the K-edge, the values for I_{AED} increase as a function

Table I. Nominal thickness, measured weight and type of CsI samples used in our experiments as specified by the manufacturer. The measured mass loading was determined from x-ray quantum detection efficiency of each sample using x-ray pulse height spectroscopy. The estimated thickness for each sample was calculated by assuming a constant density of 3.38 g/cm^3, which means a packing density of 75%.

Nominal thickness (μm)	150	150	300	450	600
Mass loading from weight (mg/cm^2)	50	51	88	142	181
Type	HR	HL	HL	HL	HL
Mass loading from attenuation (mg/cm^2)	55	57	83	143	166
Estimated thickness (μm)	163	169	246	423	491
I_{OPD}	0.88	0.90	0.91	0.93	0.95

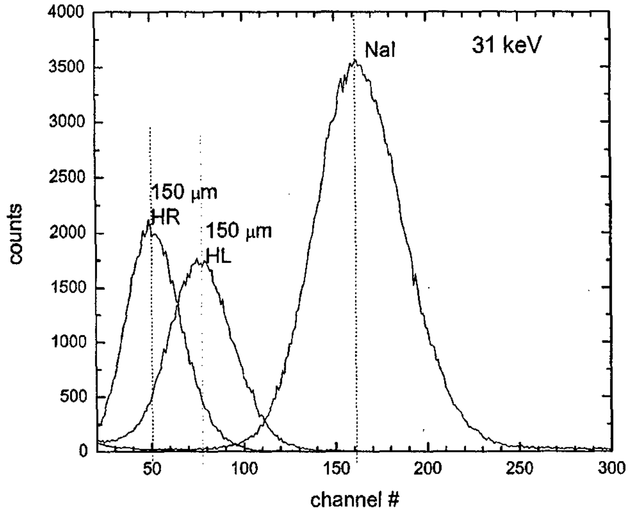

FIG. 5. PHS measurements at 31 keV for the 150 μm HR and HL CsI layers, as well as the NaI crystal.

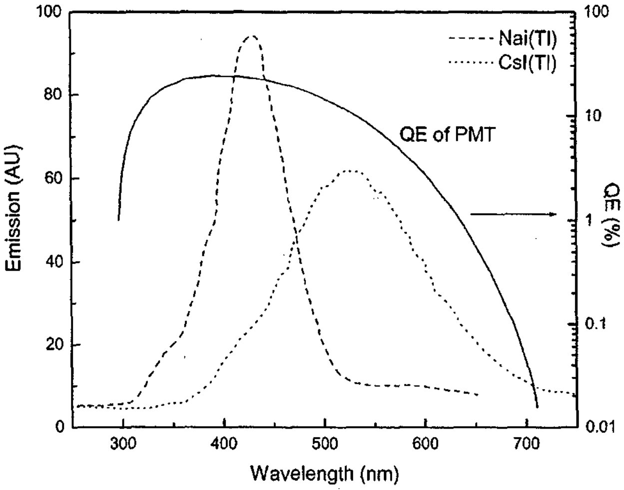

FIG. 6. The emission spectra of both NaI and CsI (Tl) scintillators plotted as a function of the wavelength of light. Plotted in the same graph is the quantum efficiency of the PMT (Hamamatsu Model R6095) (scale shown with the y-axis on the right) as a function of wavelength.

of x-ray energy E. This is because the relative position of the escape peak is closer to the main peak as E increases. The calculated I_{AED} was then multiplied by a constant I_{OPD} until the result matched well with the measured A_S. This provided a theoretical estimate of A_S and is shown in Fig. 8(a), and corresponds to a constant I_{OPD} of 0.88. Although the calculated A_S matches the measurements very closely above the K-edge, it underestimates the A_S below the K-edge ($A_S=0.91$) by ~3%. Considering that I_{OPD} is energy independent is an approximation, this is a reasonable agreement. Figure 8(a) shows that below the K-edge, optical factor I_{OPD} is the only mechanism for degradation in A_S. K-fluorescence escape, i.e., I_{AED} becomes the dominant factor for A_S just above the K-edge, and then becomes less important as E increases. In Fig. 8(b) is the measured A_S for all CsI layers used in our experiments, calculated from the PHS measurements using Eq. (2). Plotted in the same graph is a theoretical estimate of A_S obtained by multiplying the calculated I_{AED} for each layer by a constant. This produced an estimate for I_{OPD} for each CsI layer, and the values are summarized in Table I. In addition to the energy dependence, Fig. 8(b) also shows an increase in A_S for thicker CsI layers. This is because of the increased probability of K-fluorescence reabsorption, which results in a higher I_{AED}. Also, as shown in Table I, the estimated I_{OPD} values increase as a function of thickness, and the I_{OPD} for all the HL layers are higher than that for the HR. This suggests a difference in optical properties between different CsI layers, e.g., the number of light photons escaping from different depths. It is important to note that the Swank factors for the 150 μm HR and HL CsI layers are very close (0.91 and 0.93, respectively, below the K-edge). This differs from powder phosphors, where high resolution is usually achieved by replacing the reflective backing with an absorber, resulting in additional gain fluctuation noise and a much lower Swank factor which can approach 0.5.[15] The high Swank factor of HR CsI suggests that even if an absorptive backing is used, the light output from deep within the layer is not reduced, i.e., there is very little variation in the amount of light emitted per absorbed x-ray photon from different depth of the CsI layer. This needs to be considered when developing physical models for different types of CsI layers. Another possibility is that both the HR and HL CsI layers have the same reflective backing, but the HR layers have light absorbing materials between the CsI columns to minimize lateral spreading of light.

Although HR CsI has been developed for some time, it has not been used in commercial flat-panel detectors (including mammography). This is perhaps due to its lower conversion gain, which makes the FPI more susceptible to electronic noise and reduces DQE at low exposure levels.[3,27] Hence the resolution advantage of the HR type CsI has not yet been realized in the clinical products. Development of new indirect flat-panel detectors with avalanche gain can potentially compensate for the gain loss in HR CsI,[28] so that it can be used for high resolution x-ray imaging applications, e.g., mammography, in order to boost the DQE at high spatial frequencies.

3. DQE at zero spatial frequency

From the experimentally measured η and A_S, DQE(0) for different CsI samples was calculated using Eq. (4). In order to obtain a smooth curve, the fitted mass loading d shown in Table I and the corresponding η for different incident x-ray energy E were used. Shown in Fig. 9 is the measured DQE(0) as a function of incident x-ray energy for all the CsI samples used in our experiments. DQE(0) for the 150 μm HR and HL layers are essentially identical, which is to be expected from their similar thickness and Swank factor. DQE(0) increases as a function of the thickness due to increases in both η and A_S. Below the K-edge for each CsI layer, DQE(0) decreases as a function of x-ray energy E due to the drop in η. DQE(0) exhibits a

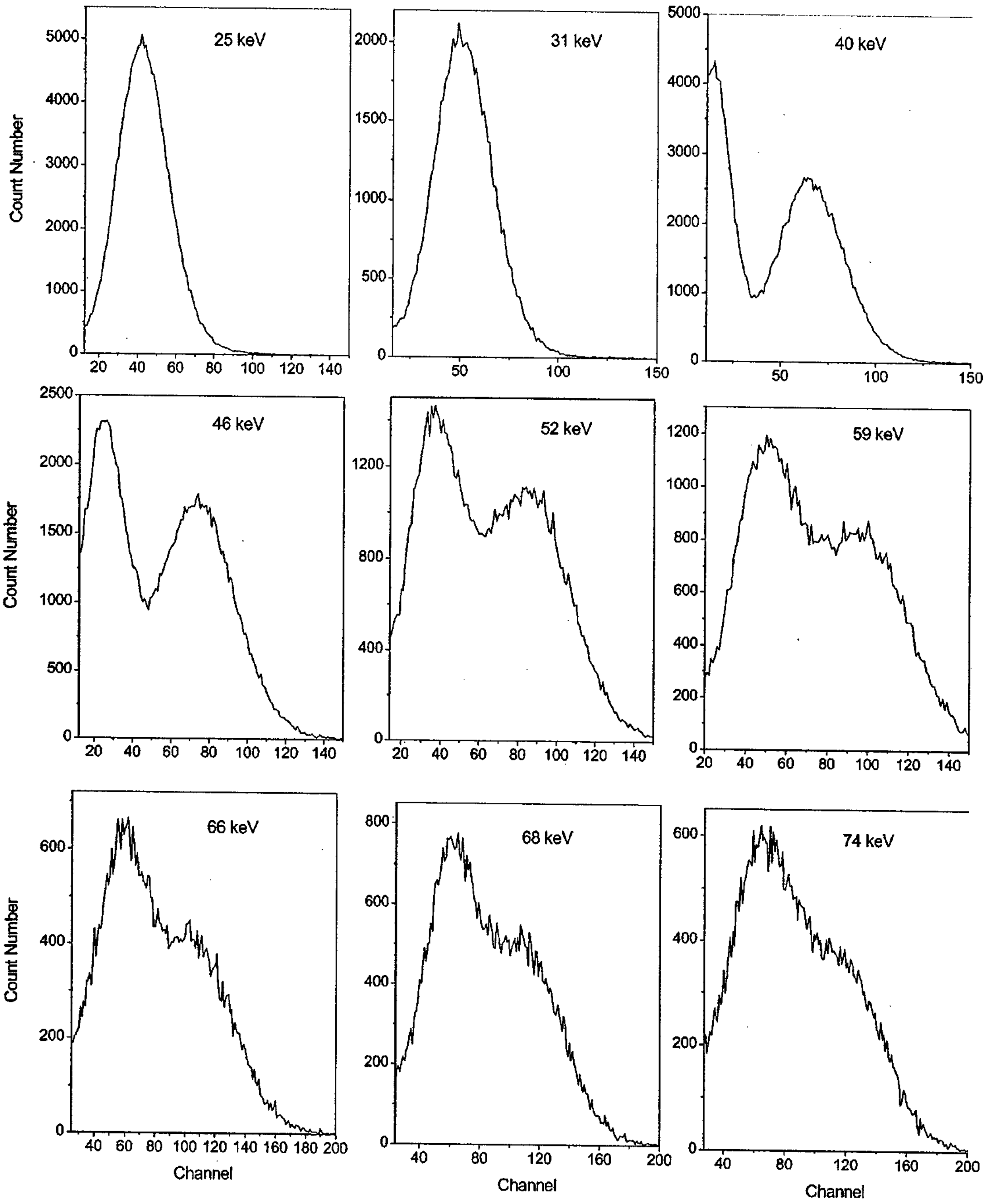

FIG. 7. PHS measured at nine different x-ray energies ranging from 25 to 74 keV for the 150 μm HR CsI layer.

significant jump just above the K-edge due to the increase in η, despite the decrease in A_S. However, DQE(0) decreases again as a function of E for energies farther above the K-edge.

B. MTF

Shown in Fig. 10(a) is the measured MTF of different CsI samples. This is after the correction MTF (i.e., pixel aperture function, slit width and the effect of focal spot size), which is also shown in Fig. 10(a) for reference, has been removed from the presampling MTF of the CsI-CMOS combination. The 150 μm HR CsI layer has the highest MTF, as expected. The MTF at 5 cycles/mm for the 150 μm HR layer is 50% higher than that of the 150 μm HL. The MTF of the HL type CsI layers decreases as a function of thickness.

There is another factor affecting the thickness dependence of MTF in Fig. 10(a), the blur caused by K-fluorescence reabsorption. It has been shown from the consideration of A_S that K-fluorescence reabsorption depends on CsI thickness. Since the spectrum used in our experiment (RQA5) has the majority of its x-ray energy above the K-edge of Cs and I, K-fluorescence plays a role in the MTF. In order to obtain a

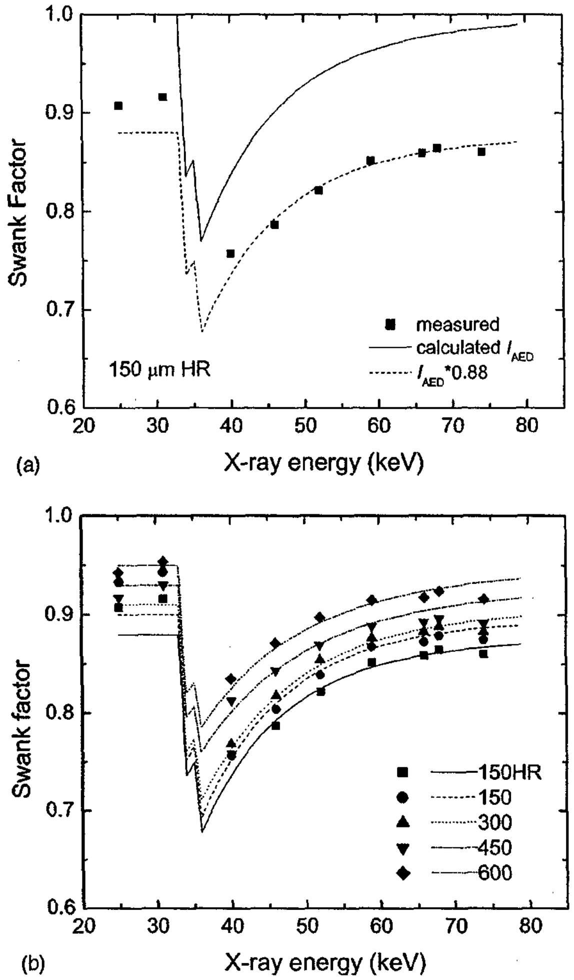

FIG. 8. (a) Swank factor for the 150 μm HR layer: The solid squares show the experimentally measured A_S from the PHS, the solid line is the calculated I_{AED}, and the dashed line is the I_{AED} scaled by a constant of 0.88. (b) Swank factors for all the CsI samples: The solid symbols represent experimentally determined A_S, and the lines represent calculated A_S values by scaling the I_{AED} due to K-fluorescence reabsorption by a constant representing the estimated I_{OPD}. The thickness values shown in the label are the nominal thickness given in μm for each layer. The type of the CsI layer is HL unless specified as HR.

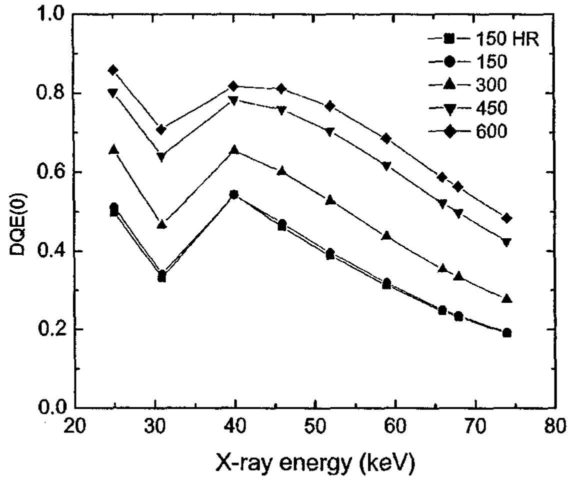

FIG. 9. Calculated DQE(0) from the measured Swank factor A_S and x-ray quantum detection efficiency η (used fitted mass loading shown in Table I).

reasonable estimate of the MTF due to optical factors alone, we computed the MTF due to K-fluorescence reabsorption for each CsI layer using a numerical method developed previously.[29] The resulting MTF_K are shown in Fig. 10(b). The MTF shown in Fig. 10(a) were then divided by the MTF_K so that the MTF_O, i.e., MTF due to optical factors alone could be estimated. The results for MTF_O are shown in Fig. 10(c) for each CsI layer. Since MTF_K decreases in thicker layers due to higher probability of K-fluorescence reabsorption, the correction is more important in the MTF_O for thicker layers than the thinner ones. As shown in Fig. 10(c), MTF_O for the 600 μm HL sample is essentially the same as that for the 450 μm sample. This is partially because there is very little difference between their estimated thicknesses. Similarly, the MTF for the 300 μm HL layer is very close to the 150 μm HL. After communicating the results to the manufacturer, we were informed that the 300 and 600 μm HL samples were manufactured in a different deposition system and had a slightly thinner columnar diameter than the rest of the samples. This also explains why the MTF of these two layers are so close to the next thinner layer.

As shown in Fig. 10(c), although the MTF for CsI layers of different thickness (HL type) differ significantly at medium and high spatial frequencies, their MTF below 1 cycles/mm are surprisingly similar. Our hypothesis is that a fraction of the CsI layer lacks the columnar structure. The most likely place for this layer to occur is at the beginning of deposition (the layer closest to the FOP in our samples). This is because the FOP substrate of our samples was not patterned prior to CsI deposition, and the columnar crystal structure only starts to form after a nominal thickness of a structureless layer is deposited.[30] We speculate this structureless CsI scintillator layer may act as a transparent layer (or at best as a powder phosphor), both of which are known to have poorer MTFs than structured scintillators. This explains why the MTF of all the CsI layers, regardless of their thickness, drops rapidly at low spatial frequency. Given that each CsI layer is composed of a fixed thickness of structureless layer in addition to the columnar structure, the fraction of structured CsI increases as a function of thickness. Figure 11 shows the MTF data in Fig. 10(c) plotted as a function of the dimensionless quantity fL, where f is the spatial frequency and L is the physical thickness of the CsI layers. In order to reflect the actual mass loading of different CsI layers, the estimated thickness shown in Table I was used instead of the nominal thickness. The universal MTF plot was first introduced by Swank in order to show that when plotted this way, the MTF is the same for all powder phosphor screens of the same design.[10] Also plotted in Fig. 11 is the universal MTF of a powder phosphor screen (Kodak Lanex Regular) which has a thickness of 167 μm.[1] It shows that the MTF for CsI of the same thickness is

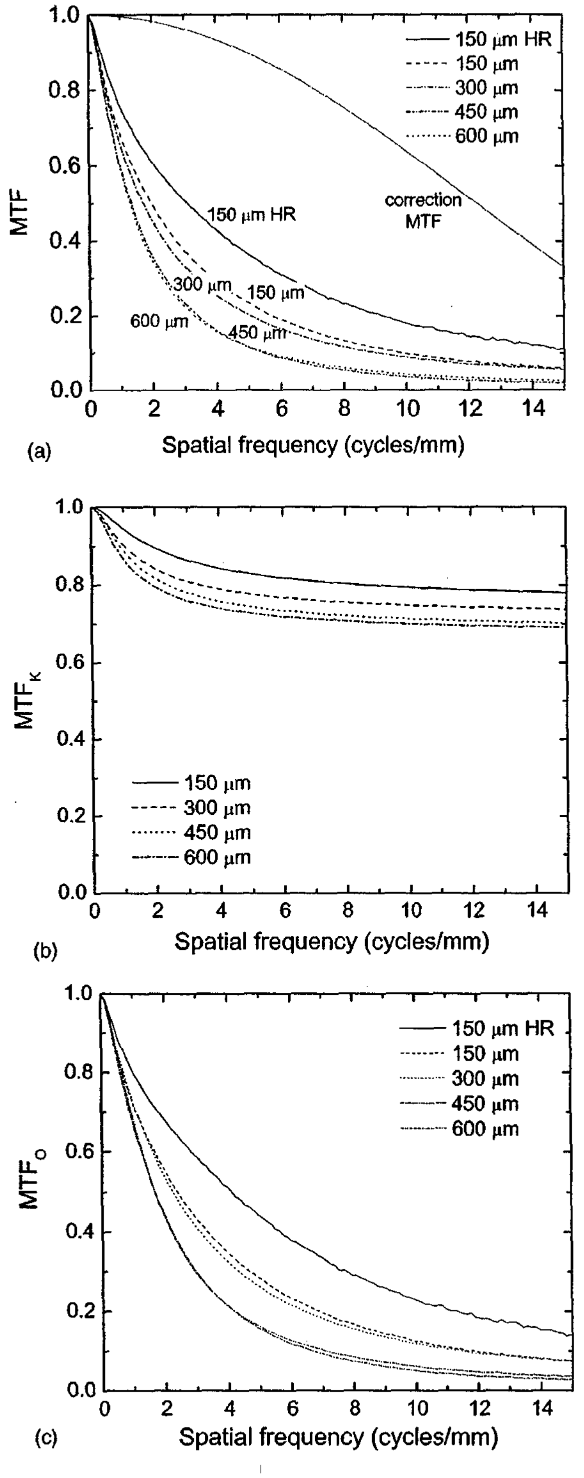

FIG. 10. (a) Presampling MTF of the CsI layers for all the CsI samples; (b) Theoretical calculation of MTF_K, i.e., MTF due to K-fluorescence reabsorption for each CsI layer; and (c) estimated MTF_O of the CsI layers, i.e., MTF due to optical factors, by dividing the MTF data in Fig. 10(a) by the calculated MTF_K shown in Fig. 10(b).

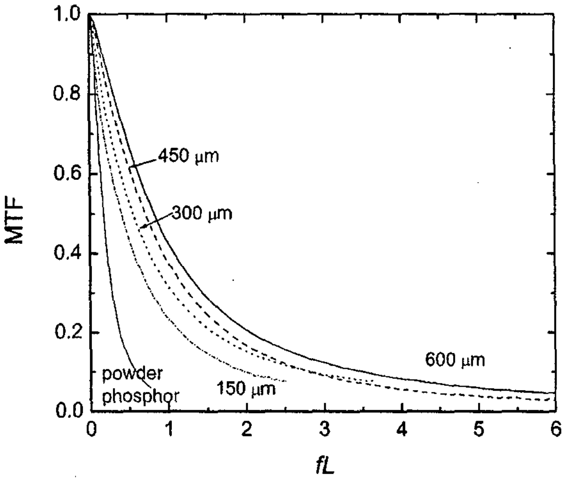

FIG. 11. Universal MTF plots for the HL CsI samples, i.e., MTF plotted as a function of the product of the spatial frequency f and the thickness of CsI L. Since the optical characteristics of the HR type is different from that of the HL, only the MTF for HL CsI layers are plotted to emphasize the thickness dependence. Plotted in the same graph for comparison is the universal MTF plot for a Kodak Lanex Regular powder phosphor screen (replotted from Ref. 1).

more than twice as high as the powder phosphor, demonstrating the advantage of the columnar structure. Figure 11 also shows that the universal MTF for CsI increases as a function of L, indicating that the benefit of the columnar structure is relatively more pronounced in thicker CsI layers. This is consistent with our hypothesis that each CsI sample consists of a structureless layer with a fixed thickness, which makes the fraction of columnar structure increases as a function of thickness.

C. DQE

In order to determine the DQE experimentally, the x-ray sensitivity and NPS measurements at different exposures are needed in addition to the MTF. Shown in Fig. 12 is the measured x-ray sensitivity of the 150 μm HL CsI layers with x-ray exposures from 0.14 to 20.9 mR. The same graph shows the best linear fit of the experimental data. Nonlinearity is observed in the detector response. Similar results were obtained from other CsI samples. We believe the nonlinearity is due to the response of the CMOS optical sensor, which has been reported previously,[17] although not as severe as observed in our experiments. The following approach was taken to correct for the effect of nonlinearity in the measurement of NPS: (1) performed flat-fielding of noise images as described in Sec. II C; (2) at each x-ray exposure, performed best linear fitting of the x-ray sensitivity with 3 data points (including the exposures just below and just above) using function $y=a+bx$; (3) corrected the flat-fielded images using:

$$CI_{i,j}=\frac{FF_{i,j}-a}{b}k_0, \tag{5}$$

where $CI_{i,j}$ and $FF_{i,j}$ were the nonlinearity corrected noise image and flat-fielded image with pixel coordinate of i and j, respectively, and k_0 was the overall x-ray sensitivity for the entire exposure range obtained from the best linear fitting as shown in Fig. 12; (4) used Fourier transform to calculate 2D NPS as described in Sec. II C. Figure 13 shows the calcu-

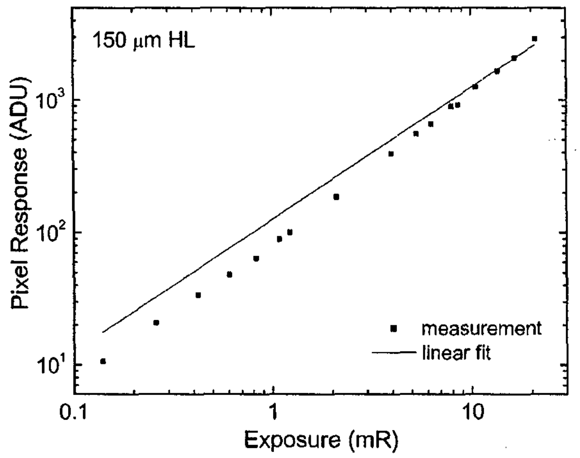

FIG. 12. An example of x-ray linearity measurements: Pixel response plotted as a function of x-ray exposure for the 150 μm HL CsI layer.

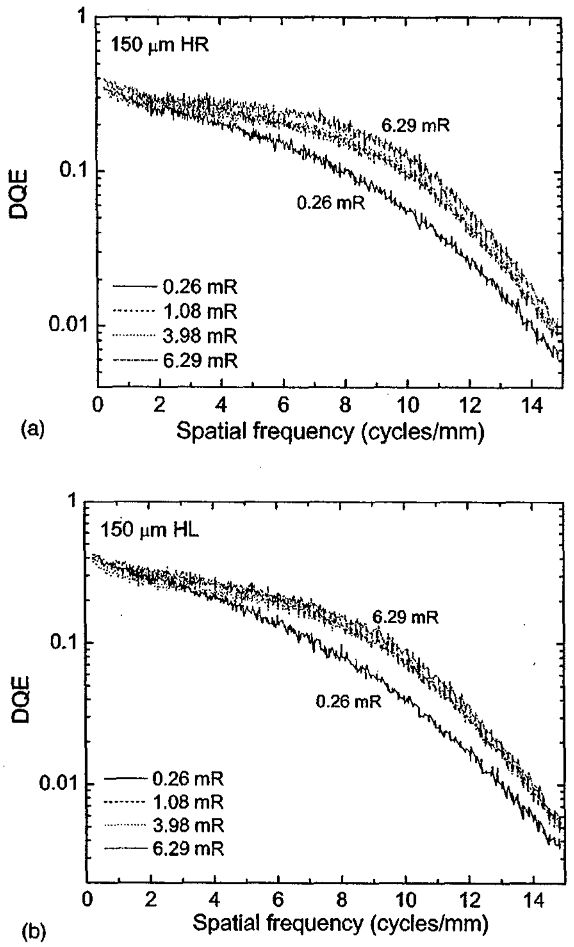

FIG. 14. DQE measurements at four different x-ray exposures for the 150 μm CsI layers: (a) HR; and (b) HL types.

lated NPS at four exposure levels for the 150 μm HR CsI layer, with 0.26 mR equivalent to the mean exposure to the detector in general radiography. Also shown is the measurement of the electronic noise power of the system (due to the electronic noise of the CMOS optical sensor). It shows that the electronic noise contributes significantly to the NPS at high spatial frequencies. Shown in Fig. 14(a) are the calculated DQE(f) of the same CsI layer. The results showed that DQE(0) measured at all exposures are essentially identical. However at high spatial frequencies, DQE is compromised by the electronic noise, especially at low exposures, which indicates that the low conversion of HR type CsI makes it more susceptible to electronic noise. For comparison, in Fig. 14(b) is the DQE measurement for the 150 μm HL CsI layer, which has higher conversion gain than the HR type. It shows that the DQE at high spatial frequencies reaches a limit for exposures of 1.08 mR and larger. The DQE(0) of both the HR and HL 150 μm layers are ~0.37, which confirms that the 150 μm HR and HL layers have similar x-ray absorption (mass loading) and Swank factor. These extrapolated DQE(0) values from the DQE(f) measurements also agree well with the independent PHS measurement of DQE(0) shown in Fig. 9 for the mean energy of 54 keV of the spectrum used in our imaging experiments.

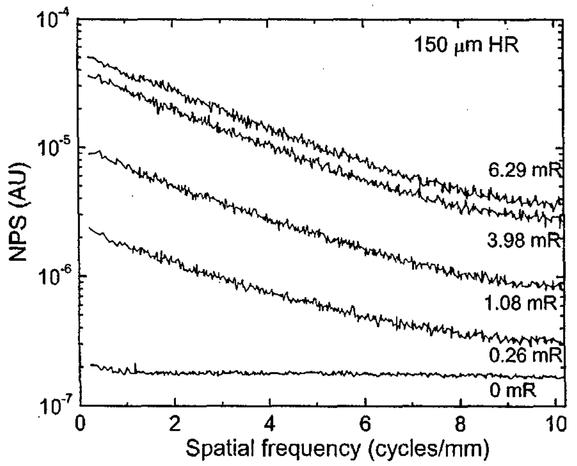

FIG. 13. NPS measurements in the dark and at four different x-ray exposure levels for the 150 μm HR CsI layer.

In order to determine the theoretical limit of the DQE of different CsI layers used in our experiments, and facilitate the comparison with DQE models, we subtracted the electronic noise from the NPS measurements at different exposures. This makes the DQE for each CsI layer exposure independent (within experimental error). For clarity only the subtracted results for the highest exposure are shown in Fig. 15.

D. DQE model

The results of DQE calculation using the linear system model are shown in Fig. 15 along with experimental measurements for comparison. The measured MTF and mass loading of each CsI layer were used for the calculation of DQE, and the model did not include the Lubberts effect. As shown in Fig. 15 for the 150 μm HR CsI, the modeled and measured DQE agree very well, which means that there is very little Lubberts effect in HR type CsI layer. For the HL CsI layers, the measured and modeled DQE agree well at

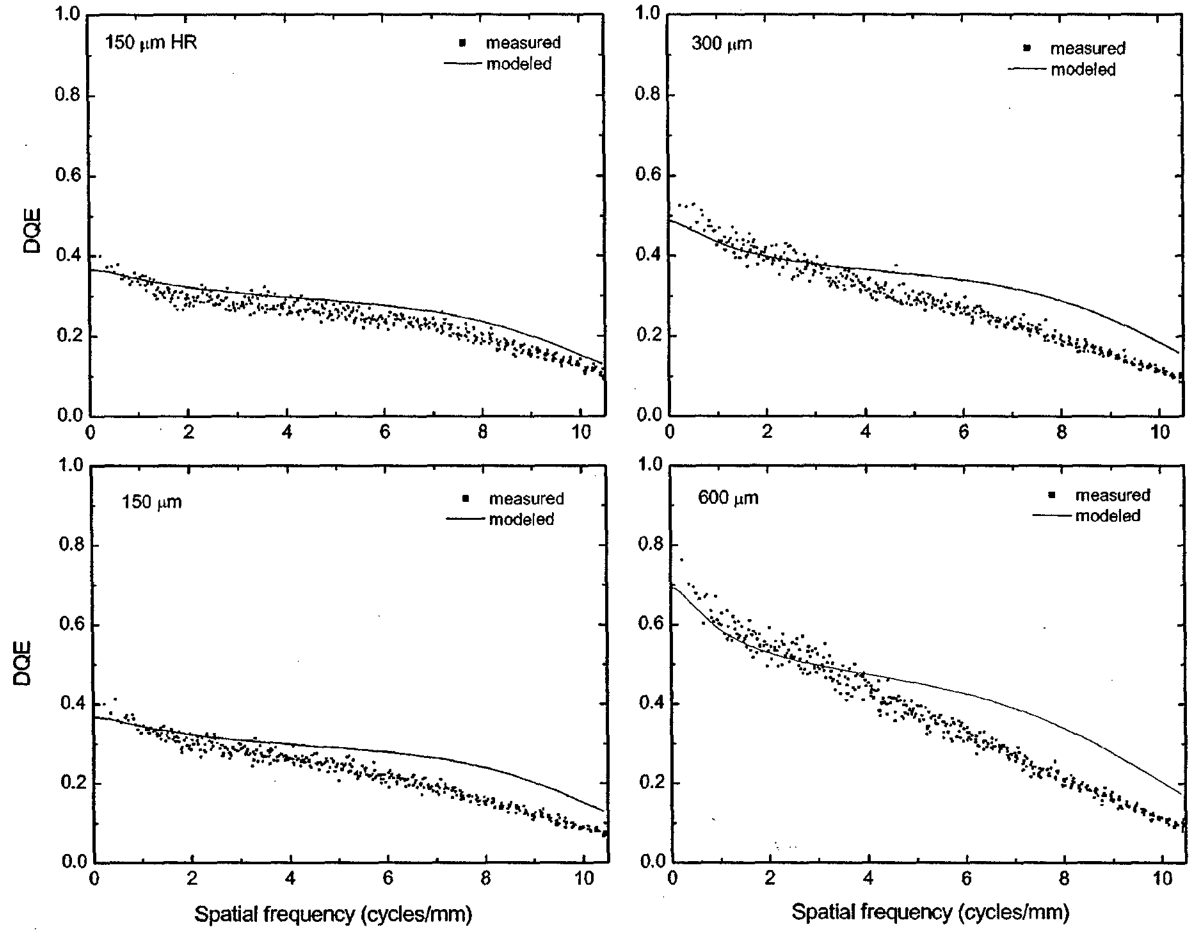

FIG. 15. Comparison between the measured and modeled DQE for four different CsI layers: The 150 μm HR and HL layers, the 300 μm and the 600 μm HL layers. (Since the mass loading and MTF for the 450 and 600 μm HL CsI layers are very similar, only the result for the 600 μm layer is shown.) After the electronic noise is subtracted from the measured DQE at different exposures, the DQE is no longer exposure dependent (within experimental errors). Hence for clarity only the subtracted results for the highest exposure level are shown.

low spatial frequencies. However at high spatial frequencies, the modeled DQE is considerably higher than the measured results. This indicates Lubberts effect in the HL type CsI. The difference between measured and modeled results increases as a function of the thickness of CsI, suggesting Lubberts effect is more severe in thicker HL CsI layers. Since the Lubberts effect arises as a consequence of different MTF for x-rays absorbed at different depths within the CsI, it can be concluded that these MTF variations are lowest for 150 μm HR layer and then increase both as the HL structure is adopted and then even further as layer thickness is increased.

Our results of DQE measurement and modeling indicate that compared to the widely used HL CsI, HR CsI has less Lubberts effect, which can lead to improved DQE at high spatial frequencies. However this is at the cost of greater susceptibility to electronic noise and compromised imaging performance at low dose. If additional gain can be obtained in indirect flat-panel detectors, e.g., through avalanche gain, HR CsI layers could be used to boost the DQE at high spatial frequencies.[28] This is particularly important for high resolution x-ray imaging applications, e.g., mammography.

Since our experiments are based on CsI samples from one manufacturer, who keeps many details of how the samples are prepared proprietary, it may be difficult to apply our findings directly to CsI made by other manufactures. Our hope is that through the establishment of a standard methodology for investigating CsI imaging properties, similar measurements can be performed by others for comparison. We also hope that our understanding of the physics behind the dependence of imaging properties on thickness and design types can lead to better modeling of the light channeling process in CsI, and provide a source of experimental data for model validation.

IV. CONCLUSIONS

In this paper, we presented our experimental study of the imaging performance of structured CsI. Both HR and HL type CsI, as well as HL CsI of different thicknesses were investigated. Our results showed that HR and HL CsI layers of the same thickness have essentially the same Swank factor. The HR CsI has less Lubberts effect compared to the HL, but at the cost of lower conversion gain, which leads to a greater susceptibility to electronic noise. The MTF of all the samples dropped rapidly at low spatial frequencies, and with a magnitude which was identical for all thicknesses. This suggests a similar components in all the samples which was hypothesized to be a transparent (unstructured) layer close to the FOP substrate. Although MTF of the HL CsI decreases as a function of thickness, on the universal MTF plot, i.e., MTF plotted as a function of the product of spatial frequency f and thickness L, MTF increases with thickness. This demonstrates that the advantage of columnar structure in CsI is more pronounced for thicker layers.

ACKNOWLEDGMENTS

We gratefully acknowledge technical assistance from G. DeCrescenzo, and financial support from the NIH (1 R01 EB002655-01). We are grateful to Y. Yamashita of Hamamatsu for providing the weight measurement of each CsI sample and additional information on the 300 and 600 μm samples.

---

[a] Telephone: 631-444-7639; Fax: 631-444-7538. Electronic mail: wei.zhao@sunysb.edu

[1] J. A. Rowlands and J. Yorkston, "Flat panel detectors for digital radiography," in *Medical Imaging. Volume 1 Physics and Psychophysics, Psychophysics*, edited by J. Beutel, H. L. Kundel, and R. L. Van Metter (SPIE, Bellingham, 2000), pp. 223–328.

[2] Ehsan Samei, "Image quality in two phosphor-based flat-panel digital radiographic detectors," Med. Phys. **30**, 1747–1757 (2003).

[3] K. W. Jee, L. E. Antonuk, Y. El-Mohri, and Q. Zhao, "System performance of a prototype flat-panel imager operated under mammographic conditions," Med. Phys. **30**, 1874–1890 (2003).

[4] C. Chaussat, J. Chabbal, T. Ducourant, V. Spinnler, G. Vieux, and R. Neyret, "New CsI/a-Si 17×17 in. x-ray flat-panel detector provides superior detectivity and immediate direct digital output for general radiography systems," Proc. SPIE **3336**, 45–56 (1998).

[5] P. R. Granfors, R. Aufrichtig, G. E. Possin, B. W. Giambattista, Z. S. Huang, J. Liu, and B. Ma, "Performance of a 41×41 cm^2 amorphous silicon flat panel x-ray detector designed for angiographic and R&F imaging applications," Med. Phys. **30**, 2715–2726 (2003).

[6] "FOS (Fiber Optic Plate with Scintillator) for Digital X-ray Imaging" Technical Information (Hamamatsu, Hamamatsu, Feb. 1996).

[7] J. A. Rowlands and K. W. Taylor, "Absorption and noise in cesium iodide x-ray image intensifiers," Med. Phys. **10**, 786–795 (1983).

[8] G. Lubberts, "Random noise produced by x-ray fluorescent screens," J. Opt. Soc. Am. **58**, 1475–1483 (1968).

[9] J. A. Rowlands, W. G. Ji, and Wei Zhao, "Effect of depth dependent modulation transfer function and k-fluorescence reabsorption on the detective quantum efficiency of indirect conversion flat panel x-ray imaging systems using CsI," Proc. SPIE **4320**, 257–267 (2001).

[10] R. K. Swank, "Calculation of modulation transfer function of x-ray fluorescent screens," Appl. Opt. **12**, 1865–1870 (1973).

[11] A. Badano and R. Reimbach, "Depth-dependent phosphor blur in indirect x-ray imaging sensors," Proc. SPIE **4682**, 94–106 (2002).

[12] Jean-Pierre Moy, "Image quality of scintillator based x-ray electronic imagers," Proc. SPIE **3336**, 187–194 (1998).

[13] R. K. Swank, "Absorption and noise in x-ray phosphors," J. Appl. Phys. **44**, 4199–4203 (1973).

[14] H. P. Chan and K. Doi, "Energy and angular dependence of x-ray absorption and its effect on radiographic response in screen-film systems," Phys. Med. Biol. **28**, 565–579 (1983).

[15] M. Drangova and J. A. Rowlands, "Optical factors affecting the detective quantum efficiency of radiographic screens," Med. Phys. **15**, 151 (1988).

[16] R. Fahrig, J. A. Rowlands, and M. J. Yaffe, "X-ray imaging with amorphous selenium: Detective quantum efficiency of photoconductive receptors for digital mammography," Med. Phys. **22**, 153–160 (1993).

[17] T. Graeve and G. P. Weckler, "High-resolution CMOS imaging detector," Proc. SPIE **4320**, 68–76 (2001).

[18] H. Fujita, D. Tsai, T. Itoh, K. Doi, J. Morishita, K. Ueda, and A. Ohtsuka, "A simple method for determining the modulation transfer function in digital radiography," IEEE Trans. Med. Imaging **11**, 34–39 (1992).

[19] James T. Dobbins III, David L. Ergun, Lois Rutz, Dean A. Hinshaw, Hartwig Blume, and Dwayne C. Clark, "DQE(f) of four generations of computed radiography acquisition devices," Med. Phys. **22**, 1581–1594 (1995).

[20] J. C. Dainty and R. Shaw, *Image Science* (Academic Press, New York, 1974), Chaps. 6 and 8.

[21] J. H. Siewerdsen, L. E. Antonuk, Y. El-Mohri, J. Yorkston, W. Huang, and I. A. Cunningham, "Signal, noise power spectrum, and detective quantum efficiency of indirect-detection flat-panel imagers for diagnostic radiology," Med. Phys. **25**, 614–628 (1998).

[22] I. A. Cunningham, "Linear-systems modeling of parallel cascaded stochastic processes: The NPS of radiographic screens with reabsorption of characteristic X radiation," Proc. SPIE **3336**, 220–230 (1998).

[23] M. Moszynski, M. Kapusta, M. Balcerzyk, D. Wolski, M. Szawlowski, and W. Klamra, "Low energy γ-rays scintillation detection with large area avalanche photodiodes," IEEE Trans. Nucl. Sci. **46**, 880–885 (1999).

[24] "NaI (Tl) and Polyscin NaI (Tl) sodium iodide scintillation material," Product Data Sheet for sodium iodide scintillation material, Saint-Gobain Crystalls and Detectors, Newbury, OH.

[25] Product Manual for PMT R6095, Hamamatsu Photonics, K.K., Hamamatsu City, Japan.

[26] L. E. Antonuk, K.-W. Jee, Y. El-Mohri, M. Maolinby, S. Nassif, X. Rong, Q. Zhao, J. H. Siewerdsen, R. A. Street, and K. S. Shah, "Strategies to improve the signal and noise performance of active matrix, flat-panel imagers for diagnostic x-ray applications," Med. Phys. **27**, 289–306 (2000).

[27] L. E. Antonuk, Y. El-Mohri, J. H. Siewerdsen, J. Yorkston, W. Huang, V. E. Scarpine, and R. A. Street, "Empirical investigation of the signal performance of a high-resolution, indirect detection, active matrix flat panel imager (AMPFI) for fluoroscopic and radiographic operation," Med. Phys. **24**, 51–70 (1997).

[28] Wei Zhao, D. C. Hunt, Kenkichi Tanioka, and J. A. Rowlands, "Indirect flat-panel detectors with avalanche gain," Proc. SPIE **5368** (to be published).

[29] Wei Zhao, W. G. Ji, and J. A. Rowlands, "Effects of characteristic x rays on the noise power spectra and detective quantum efficiency of photoconductive x-ray detectors," Med. Phys. **28**, 2039–2049 (2001).

[30] T. Jing, G. Cho, J. Drewery, I. Fujieda, S. N. Kaplan, A. Mireshghi, V. Perez-Mendez, and D. Wildermuth, "Enhanced columnar structure in CsI layer by substrate patterning," IEEE Trans. Nucl. Sci. **39**, 1195–1198 (1992).

APPENDIX 2

Indirect flat-panel detector with avalanche gain: Design and operation of the avalanche photoconductor

Wei Zhao,[1] Dan Li,[1] Alla Reznik,[2] Brian Lui,[2] D. C. Hunt,[2] Kenkichi Tanioka,[3] and J. A. Rowlands[2]
[1] Department of Radiology, State University of New York at Stony Brook
L-4, 120 Health Sciences Center
Stony Brook, New York 11793-8460
[2] Imaging Research, Sunnybrook and Women's Health Sciences Center
2075 Bayview Avenue
Toronto, Ontario, Canada M4N 3M5
[3] Advanced Imaging Devices Research Division
Science & Technical Research Laboratories
Japan Broadcasting Corporation
1-10-11 Kinuta, Setagaya-ku, Tokyo 157-8510 Japan

ABSTRACT

An indirect flat-panel imager (FPI) with avalanche gain is being investigated for low-dose x-ray imaging. It is made by optically coupling a structured x-ray scintillator CsI(Tl) to an amorphous selenium (a-Se) avalanche photoconductor called HARP. The final electronic image can be read out using either an array of thin film transistors (TFT) or field emitters (FE). The advantage of the proposed detector is its programmable gain, which can be turned on during low dose fluoroscopy to overcome electronic noise, and turned off during high dose radiography to avoid pixel saturation. This paper investigates the important design considerations for HARP such as avalanche gain, which depends on both the thickness d_{Se} and the applied electric field E_{Se}. To determine the optimal design parameter and operational conditions for HARP, we measured the E_{Se} dependence of both avalanche gain and optical quantum efficiency of an 8 μm HARP layer. The results were applied to a physical model of HARP as well as a linear cascaded model of the FPI to determine the following x-ray imaging properties in both the avalanche and non-avalanche modes as a function of E_{Se}: (1) total gain (which is the product of avalanche gain and optical quantum efficiency); (2) linearity; (3) dynamic range; and (4) gain non-uniformity resulting from thickness non-uniformity. Our results showed that a HARP layer thickness of 8 μm can provide adequate avalanche gain and sufficient dynamic range for x-ray imaging applications to permit quantum limited operation over the range of exposures needed for radiography and fluoroscopy.

1. INTRODUCTION

We previously proposed the concept of indirect flat-panel imagers (FPI) with avalanche gain by optically coupling a structured x-ray scintillator CsI(Tl) to an amorphous selenium (a-Se) avalanche photoconductor called HARP (High-gain Avalanche Rushing Photoconductor).[1] Shown in Figure 1 is a side view of the proposed detector. The photons emitted from the CsI are absorbed by the HARP layer and generate electron-hole pairs near the top interface (light entrance side). Under a sufficiently high electric field E_{Se} (i.e. applying a positive voltage on the top bias electrode of a-Se), holes move towards the bottom surface and undergo avalanche multiplication. The avalanche gain g_{av} can be as high as 1500 depending on E_{Se} and the thickness of the a-Se layer, d_{Se}. The holes are collected at the bottom surface of a-Se to form a charge image, which is read out electronically using either an active matrix thin film transistor (TFT) array or a field emitters array (FEA). We called the proposed detector with TFT readout SHARP-AMFPI (Scintillator HARP Active Matrix Flat Panel Imager) and with FEA readout SAPHIRE (Scintillator Avalanche Photoconductor with High resolution Emitter Readout). The advantage of the proposed detectors is its programmable gain, which can be turned on during low dose imaging procedures (e.g. fluoroscopy) to overcome electronic noise, and turned off during high dose imaging (e.g. radiography) to avoid pixel saturation. This paper investigates the important design parameters and operational conditions for HARP in order to ensure adequate dynamic range for both fluoroscopy and radiography.

Medical Imaging 2005: Physics of Medical Imaging, edited by Michael J. Flynn,
Proceedings of SPIE Vol. 5745 (SPIE, Bellingham, WA, 2005)
1605-7422/05/$15 · doi: 10.1117/12.597295

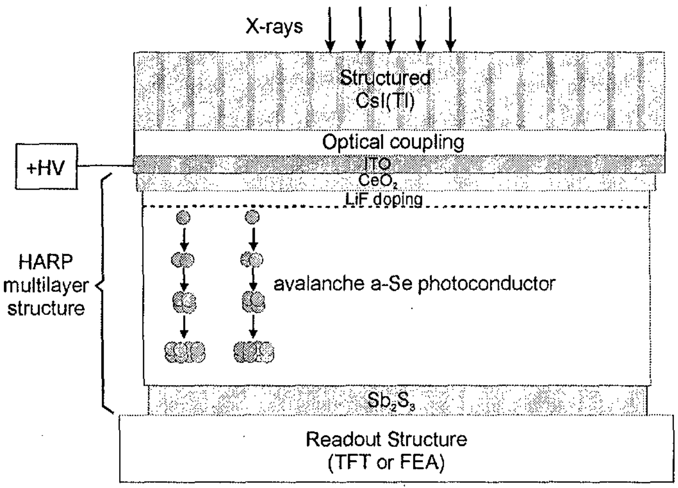

Figure 1: Side view showing the concept of indirect flat-panel detector with avalanche gain. (Note: thickness not to scale.) X-rays enter from the top with the ITO (top) electrode of HARP biased positively. The charge (hole) image collected on the bottom surface of the HARP is read out with either a TFT array or a FEA.

Since avalanche multiplication in a-Se was discovered over a decade ago, HARP tubes, which consist of a HARP layer read out with a scanning electron beam, have been commercialized for high sensitivity and high definition television applications. Stable and uniform avalanche multiplication has been observed with very little added noise.[2] The electric field E_{Se} under which avalanche multiplication occurs is > 70 V/μm, which is an order of magnitude higher than that typically used in direct FPI incorporating thick a-Se layers. To sustain an E_{Se} of this magnitude without a significant increase in dark current due to charge injection from the bias electrodes, blocking layers need to be developed for both electrode interfaces. As shown in Figure 1, the HARP sensor consists of a multi-layer structure.[3] It contains a transparent bias electrode indium tin oxide (ITO) that is biased positively during imaging, followed by a thin layer (~20 nm) of Cerium Oxide (CeO_2) and a thin layer of lithium fluoride (LiF) doped a-Se to block the injection of holes from the ITO bias electrode. The intrinsic a-Se photoconductor is usually 0.5 – 35 μm thick depending on the desired avalanche gain and doped with arsenic (As) to prevent the a-Se from recrystallizing. The bottom interface of the HARP structure is a sub-micron thin layer of antimony tri-sulfide (Sb_2S_3), which is used to block electron injection from the negative bias electrode (in a solid state detector with TFT readout) or the scanning electron beam (in HARP tubes or with FEA readout). Since the mobility of holes in a-Se is more than an order of magnitude higher than that of the electrons, only holes create a significant number of new carriers by impact ionization. Hence it is essential for light photons to enter from the positive bias side.

Our previous calculation using a preliminary linear system model of indirect FPI with avalanche gain predicted that a gain of 20 would be needed to produce x-ray quantum noise limited performance for fluoroscopy and low dose mammography (tomosynthesis). This requires a HARP layer thickness of 8 μm or more. To determine proper design parameters and operational conditions for HARP, we measured the E_{Se} dependence of both avalanche gain and optical quantum efficiency of an 8 μm HARP layer. The results were used in a physical model of HARP as well as a linear cascaded model of the FPI to determine the following x-ray imaging properties in both the avalanche and non-avalanche modes as a function of d_{Se} and E_{Se}: (1) total gain (which is the product of avalanche gain and optical quantum efficiency); (2) linearity; (3) dynamic range; and (4) gain non-uniformity resulting from thickness non-uniformity.

2. PHOTOSENSITIVTY OF HARP

The x-ray imaging performance of indirect FPI with avalanche gain relies on the photosensitivity of HARP. Understanding its dependence on E_{Se} and layer thickness d_{Se} is crucial for optimization of HARP design parameters and operational conditions for both the avalanche and non-avalanche modes. In this section, we will first present the experimental method and results of the photosensitivity measurements of HARP, and then describe the theory of E_{Se} dependence of photosensitivity, which is proportional to both the optical quantum efficiency (QE) η and the avalanche gain g_{av}. The theory and experimental data will then be used to determine η and g_{av} as a function of E_{Se} in the context of x-ray imaging.

2.1. Experimental measurement of photosensitivity

2.1.1. Method:

The experimental setup for the photosensitivity measurement is shown in Figure 2. A grating monochromator was used to generate optical photons of a single wavelength λ. The range of λ values used in our experiments was between 300-700 nm. The intensity of the output beam was attenuated by neutral-density (ND) filters. A beamsplitter was used to direct a fraction (90 %) of the attenuated beam to a silicon (Si) photodiode (PD), which monitored the beam intensity during experiment. The optical photons passing directly through the beam splitter (10 %) were detected by the HARP tube. Before sensitivity measurements the HARP input light intensity was calibrated for each λ in order to keep a constant input power. This was achieved by adjusting the ND filters and monitoring the light intensity using the Si PD.

For each λ and E_{Se}, the signal current S obtained by the HARP tube was recorded, and the photosensitivity was quantified as the number of signal charge carriers generated by one absorbed light photon. This quantity is referred to as the effective quantum efficiency η^*, and it is the product of η and g_{av}. The values of η^* was experimentally determined from the measurement of the HARP tube current S using:

$$\eta^* = \frac{S/e}{IT/h\nu} \tag{2}$$

where e was the electron charge, I was the HARP input light intensity power given in Watts (W), $h\nu$ was the energy of each incident photon, and T was the fraction of the incident photons (to HARP) reaching the a-Se layer. The correction factor T was due to light attenuation by both the ITO bias electrode and the CeO_2 blocking layer for HARP, and is a function of the wavelength λ. The value of T was experimentally measured for all λ used.

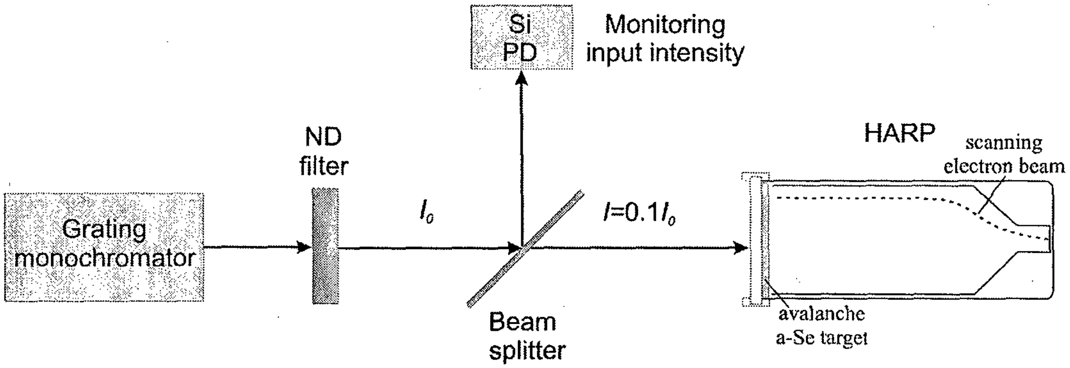

Figure 2: Experimental apparatus for measuring the photosensitivity of HARP.

2.1.2. Measurement results:

Shown in Figure 3 is the measured effective quantum efficiency η^* as a function of E_{Se} for an 8 μm thick HARP layer. It shows that for blue light (λ=400 nm), η^* reaches a plateau at $E_{Se} > 20$ V/μm. This corresponds to a saturation of optical quantum efficiency η at unity. With further increase in E_{Se} to > 80 V/μm, η^* starts to increase again, demonstrating the onset of avalanche. However for green light, the E_{Se} dependence of η^* is quite different. As shown in Figure 3 for λ=540 nm, which is the peak of the emission spectrum of CsI (Tl), η^* begins at a much smaller value compared to λ=400 nm. It then increases continuously with E_{Se} without saturation before avalanche starts at ~80 V/μm. This is because of the lower optical η for λ=540 nm compared to λ=400 nm. It does not saturate as a function of E_{Se} or reach unity until E_{Se} is well into the range of avalanche multiplication. To choose the proper operational condition for HARP in different x-ray imaging applications, we need to understand separately the E_{Se} dependence of η and g_{av}. This will be discussed in section 2.2.

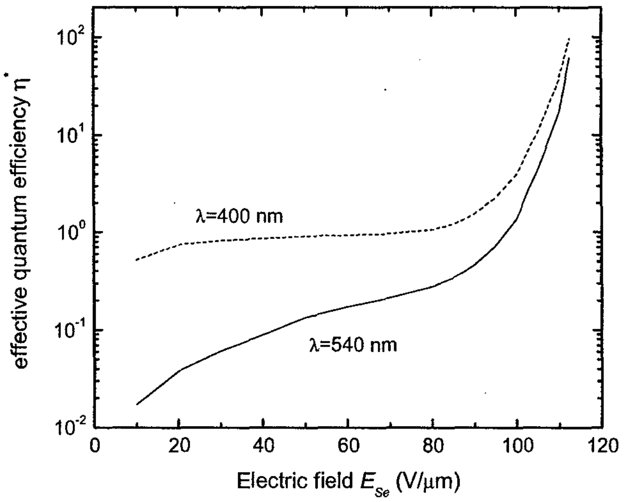

Figure 3: Measured effective quantum efficiency η^* as a function of E_{Se} for an 8 μm thick HARP layer.

2.2. Theory of photosensitivity of HARP: Quantum efficiency and avalanche gain

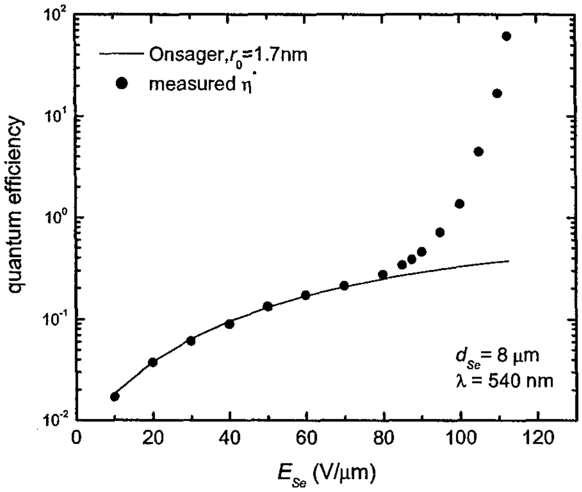

Figure 4: The optical quantum efficiency of a-Se calculated using Onsager theory and $r_0 = 1.7$ nm, compared with the measured effective quantum efficiency η^* at $\lambda = 540$ nm.

The effective quantum efficiency η^* of HARP is proportional to both η and g_{av}. The value of η in a-Se depends on both E_{Se} and the wavelength λ of the incident photon. It was found by Pai and Enck that the E_{Se} and λ dependence of photogeneration in a-Se follows the Onsager mechanism.[4] Onsager theory states that every absorbed photon creates a pair of thermalized carriers bound by their Coulombic attraction. The initial separation r_0 of the charge pair increases with incident photon energy. The probability of dissociation for the bound pairs into free carriers increases with r_0 and the applied external field E_{Se} with the relationship:

$$\eta = \phi_0 \frac{kT}{eE_{Se}r_0} e^{-A} e^{-eE_{Se}r_0/kT} \sum_{m=0}^{\infty} \frac{A^m}{m!} \sum_{n=0}^{\infty} \sum_{l=m+n+1}^{\infty} \left(\frac{eE_{Se}r_0}{kT}\right)^l \frac{1}{l!}, \text{ with } A = \frac{e^2}{4\pi\varepsilon\varepsilon_0 kT} \tag{1}$$

where ϕ_0 is defined as the efficiency of production of thermalized charge pairs per absorbed photon, and it is independent of E_{Se}. Pai and Enck showed that the room temperature measurement of η can be best fitted with the expression in Eq. 1 using $\phi_0=1$ and r_0 in the range between 0.8 – 7.0 nm for λ values between 620 and 400 nm. From now on we will focus on λ=540 nm, which is the peak of the emission spectrum for CsI (Tl). Shown in Figure 4 is the η calculated using Eq. 1 and r_0 = 1.7 nm. Also plotted in Figure 4 is the measured η^* at the same wavelength for d_{Se} = 8 μm. Figure 4 shows that the Onsager theory provides a reasonable prediction for the E_{Se} dependence of η^* in HARP for $E_{Se} \leq 70$ where g_{av} = 1. The calculated η using Onsager theory was then divided into the measured η^* so that the E_{Se} dependence of avalanche gain g_{av} could be obtained. The results are shown in Figure 5 (a), where g_{av} = 46 at E_{Se} = 110 V/μm. Figure 5 (a) shows that g_{av} increases very rapidly with E_{Se}. Hence choosing the right operating condition for HARP is crucial. To determine the x-ray response of the indirect FPI with avalanche gain, it is necessary to understand the continuous dependence of g_{av} on E_{Se}. This is because as image charge accumulates on the pixels, the voltage drop across the HARP layer will decrease. With the rapid change in g_{av} as a function of E_{Se} shown in Figure 5 (a), the value of g_{av} will decrease as a result of charge accumulation on the pixels. This will affect the x-ray sensitivity, linearity and dynamic range of the FPI.

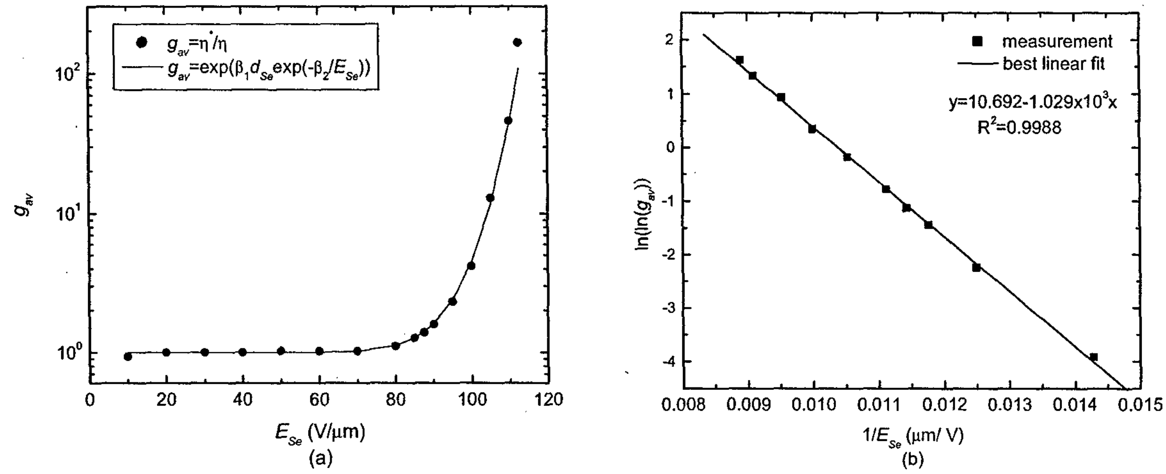

Figure 5: (a) Solid circles are the g_{av} for the 8 μm HARP layer calculated by dividing the measured η^* at 540 nm by the optical η predicted by the Onsager theory using r_0 = 1.7 nm. The solid line shows the g_{av} calculated using the fitted β_1 and β_2 values. (b) The plot of ln(ln(g_{av})) as a function of $1/E_{Se}$, and the best linear fit for the data.

The avalanche gain characteristics in HARP have been investigated as a function of d_{Se} and E_{Se}.[5] According to the theory of avalanche multiplication,[6] when E_{Se} across the thickness d_{Se} is uniform, and the distance through which avalanche occurs is equal to d_{Se} (which is true for HARP because photons are absorbed within 0.1 μm at the light entrance side of the a-Se layer), g_{av} is given by:

$$g_{av} = \frac{(\beta-\alpha)e^{d_{Se}(\beta-\alpha)}}{\beta-\alpha e^{d_{Se}(\beta-\alpha)}} \tag{2}$$

where α and β are the impact ionization rates of electrons and holes, respectively. Since in a-Se the drift mobility of holes (0.18 cm^2/Vs) is much higher than that of electrons (0.003 cm^2/Vs), β is much greater than α. Thus in HARP light always enters from the positive bias electrode to maximize the avalanche gain. Under the assumption that the impact ionization of electrons is negligible, Eq. 2 can be simplified to:

$$g_{av} = e^{d_{Se}\beta} \tag{3}$$

with β given by:

$$\beta = \beta_1 e^{\frac{-\beta_2}{E_{Se}}}. \tag{4}$$

The values for β_1 and β_2 can be determined by curve fitting of the experimental measurement of g_{av}. By taking the logarithm of Eq. 3 twice, we obtain:

$$\ln(\ln g_{av}) = \ln(\beta_1 d_{Se}) - \frac{\beta_2}{E_{Se}}, \quad (5)$$

which indicates that the quantity $\ln(\ln g_{av})$ is linearly related to $1/E_{Se}$. Shown in Figure 5 (b) is the experimentally determined g_{av} data [shown in Figure 5(a)] replotted in the form of $\ln(\ln g_{av})$ as a function of $1/E_{Se}$. The best linear fit for the experimental data is also shown in Figure 5 (b). From the intercept and the slope of the fitted curve we obtained $\beta_1=5.5 \times 10^3$ /μm and $\beta_2 = 1.029 \times 10^3$ V/μm. Using these β_1 and β_2 values and the analytical expression for g_{av} shown in Eqs. 3 and 4, the theoretical g_{av} values are calculated and shown in Figure 5 (a). The calculated g_{av} using the fitted parameters agrees well with experimentally determined g_{av} except for the highest E_{Se} of 112.5 V/μm. This could be seen from the relative large error in fitting for this data point in Figure 5 (b). Since g_{av} is related to β_2 through two exponential functions, a small error in the estimate of β_2 can result in a large error in the estimate of g_{av}. Nevertheless the quality of fitting for $E_{Se} \leq 110$ V/μm is excellent, and the fitted parameters β_1 and β_2 will be used in the following calculation of x-ray response.

3. X-RAY IMAGING PERFORMANCE

We have previously developed a cascaded linear system model for the indirect FPI with avalanche gain.[1] In this section, we will apply the E_{Se} dependence of g_{av} and η derived in the previous section to the cascaded linear system model to determine the x-ray response and the detective quantum efficiency, DQE(*f*), of the indirect FPI with avalanche gain. We will use the resolution and avalanche gain requirements for a radiography/fluoroscopy (R/F) detector as an example. It can be shown from the cascaded linear system model that the mean signal from each pixel of the detector is given by:[1]

$$\Phi_s = a_p{}^2 \alpha \eta g_{av} \sum_E \eta_x g(E) q_0(E) \quad (6)$$

where a_p is the pixel pitch of the detector, η_x is the x-ray quantum absorption efficiency of the CsI layer, $g(E)$ is the x-ray to light conversion gain of CsI that depends on the x-ray energy E and the energy required to generate an optical photon W, $q_0(E)$ is the incident x-ray spectrum (which is given in number of photons per unit area for a given exposure), and α is the optical coupling efficiency between the CsI and the a-Se layer. The DQE(*f*) of the detector is given by:[1]

$$\mathrm{DQE}(f) = \frac{T_a{}^2(f) T_b{}^2(f) T_c{}^2(f)}{[\frac{1}{\eta_x A_S} T_a{}^2(f) T_b{}^2(f) + \frac{(2g_{av}-1)}{g_{av} g \eta_x \alpha \eta}] T_c{}^2(f) + \frac{S_a}{(a_p{}^2 g_{av} g \eta_x \alpha \eta)^2 q_0}} \quad (7)$$

where A_S is the Swank factor of CsI, S_a is the added electronic noise, $T_a(f)$, $T_b(f)$ and $T_c(f)$ are the modulation transfer function (MTF) due to the CsI, the optical coupling between CsI and HARP, and the pixel aperture function, respectively.

Our previous investigation of the inherent x-ray imaging performance of CsI (Tl) has shown that a 600 μm CsI layer optimized for high light output (HL) could provide adequate performance for R/F applications.[7] Hence the measured imaging properties of this CsI layer were used in our cascaded linear system model. Table I summarizes the detector parameters and HARP operating conditions chosen for fluoroscopy and radiography.

Table I: Detector parameter and operating conditions chosen for different x-ray imaging applications.

	R/F detector	
	Fluoroscopy	Radiography
Pixel pitch a_p (μm)	200	
X-ray spectrum	RQA5	
Electronic noise	1500 electrons	
CsI (75% packing density)	600 μm HL	
W for CsI (eV)	18	
α	0.8	
Minimum exposure	0.1 μR	30 μR
E_{Se} (V/μm)	110	95
η	0.36	0.31
g_{av}	46	2.3

3.1. DQE(*f*)

Shown in Figure 6 (a) is the DQE(*f*) calculated using the cascaded linear system model for the detector with different g_{av} settings. The calculation was performed for the lowest exposure in fluoroscopy (0.1 μR), where the detector performance is most susceptible to electronic noise. It shows that $g_{av} = 46$ is sufficient to bring the DQE(*f*) to its theoretical limit (i.e. a detector without electronic noise). The DQE(*f*) for the next highest $g_{av} = 12$ measured at $E_{Se} = 105$ V/μm also provides reasonable DQE. Thus an E_{Se} between 105 and 110 V/μm will be adequate for fluoroscopy. Figure 6 (b) shows the DQE(*f*) calculated for the lowest radiographic exposure of 30 μR. It shows that $E_{Se} = 95$ V/μm can provide sufficient η and g_{av}. Hence the E_{Se} chosen in Table I is adequate for the dual-mode operation of an R/F detector.

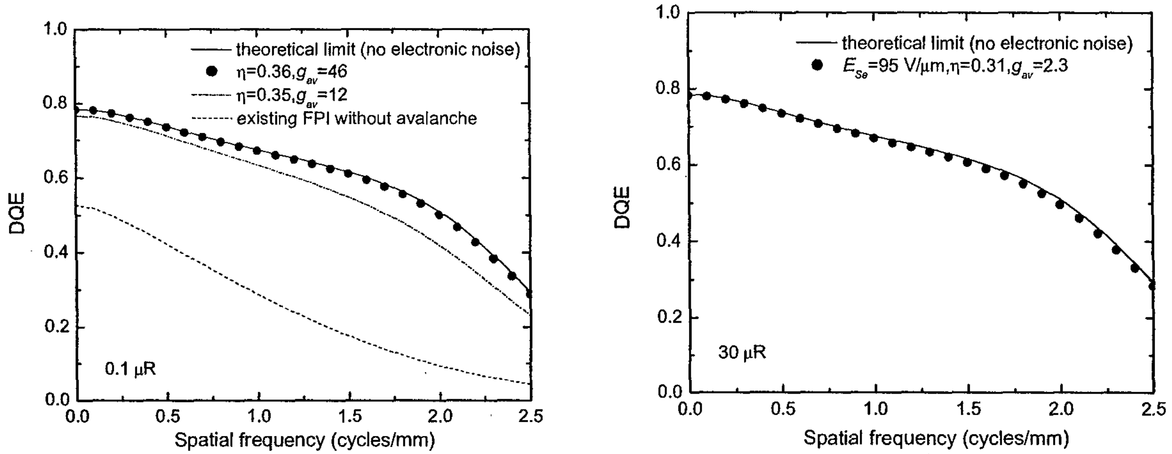

(a) (b)

Figure 6: Calculated DQE(*f*) using the detector parameters and operating conditions shown in Table I for a fluoroscopy detector at the x-ray exposure level of: (a) 0.1 μR; and (b) 30 μR.

3.2. Pixel x-ray response

Shown in Figure 7 is the calculated pixel x-ray response for the R/F detector under two different operational conditions. It was assumed that the dominant pixel capacitance was from the capacitance of the HARP layer. This condition results in the greatest drop in the potential across the HARP layer for a given x-ray exposure, and creates the largest effect on linearity. Figure 7 (a) shows that for fluoroscopy, the initial $E_{Se} = 110$ V/μm provides a g_{av} of 46. Within the regular exposure range of 0.1 – 10 μR/frame in fluoroscopy, the detector has very good linearity, i.e. an essentially constant g_{av}. With further increase in exposure, which corresponds to detector exposure around the edge of the human body or raw exposure to detector, the x-ray response becomes sublinear with a decrease in g_{av}. This decrease in g_{av} ensures a wide dynamic range for the detector because there is no "hard" saturation. The pixel potential will continue to increase as a function of x-ray exposure until it reaches the predetermined V_{max} for high voltage protection (for the TFT readout method). The method for high voltage protection is described in detail elsewhere[8] and will not be discussed here. The pixel potential for the exposure of 1 mR in the fluoroscopy mode is $V_P = 56$ V, which is safe for a-Si TFTs. Figure 7 (b) shows that with a much lower $g_{av} = 2.4$ programmed for radiography, the detector response for the regular detector exposure range of 30 – 3 mR is essentially linear with very little change in g_{av}. Comparing Figures 7 (a) and (b), the image charge on the pixel is in the same range despite their large difference in exposure range. This demonstrates the wide dynamic range (over 5 orders of magnitude) of the detector by varying g_{av} for different x-ray imaging applications. This is different from a detector with constant high gain, which has the problem with pixel saturation for radiographic applications.

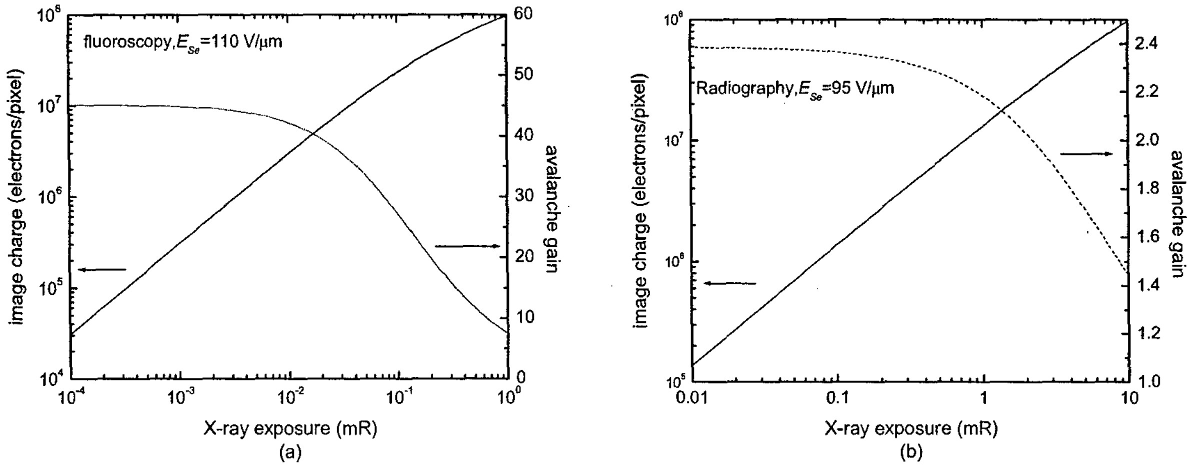

Figure 7: The calculated image charge on each pixel of the detector (left axis) and the corresponding avalanche gain (right axis) as a function of x-ray exposure for the detector operational setting of: (a) fluoroscopy; and (b) radiography

4. EFFECT OF HARP THICKNESS UNIFORMITY

An important issue for making a large area HARP is its thickness uniformity. Currently HARP films can be made very uniform for an area of 1-2" in diameter with essentially no visible gain variation in the images. The images currently produced by HARP for broadcast applications do not require any gain uniformity correction. The area of HARP needs to be increased significantly for x-ray imaging applications. Although uniform, large area a-Se films have been developed for direct FPI, the uniformity requirement for HARP in indirect FPI with avalanche gain is expected to be much higher. In this section we will derive the relationship between thickness non-uniformity and gain non-uniformity for HARP sensors so that the results can be used as a guideline for engineering of large area HARP layers for FPI.

During the operation of HARP, a constant potential V_b is applied to the top bias electrode (ITO). A non-uniformity in the thickness of HARP will result in a variation in E_{Se} and hence a gain non-uniformity. By substituting $E_{Se} = V_b/d_{Se}$ into Eq. 5 and differentiating both sides of the equation, we obtain:

$$\frac{1}{\ln g_{av}}\frac{\Delta g_{av}}{g_{av}} = \frac{\Delta d_{Se}}{d_{Se}} - \frac{\beta_2}{V_b}\Delta d_{Se}. \qquad (8)$$

Eq. 8 can be rewritten as:

$$\frac{\Delta g_{av}}{g_{av}} = \ln(g_{av})(1-\frac{\beta_2}{E_{Se}})\frac{\Delta d_{Se}}{d_{Se}}. \qquad (9)$$

Eq. 9 shows that the percentage variation in avalanche gain is proportional to $\ln(g_{av})$ and the percentage thickness variation. Shown in Figure 8 are the variations in g_{av} for both positive and negative change in d_{Se} around 8 μm. Three V_b values of 840 V, 864 V and 880 V were used, which corresponds to g_{av} of 12, 25 and 46, respectively. Figure 8 shows that g_{av} increases with decrease in d_{se}, which is due to an increase in E_{Se} under a constant V_b. The slope of the curve, i.e. percentage change in g_{av}, is much higher for negative change in d_{Se} than it is for positive. Hence when choosing the bias potential V_b for a desired E_{Se}, the smallest d_{Se} for the entire detector area should be used; so that the variation in thickness is positive from the reference thickness. If we assume the smallest d_{Se} = 8 μm, the percentage changes in g_{av} due to increase in d_{Se} of 1 % are 19 %, 23 % and 26 %, respectively, for the three V_b settings of 840 V, 864 V and 880 V. The change in g_{av} increases to 33 %, 40 %, and 44 %, respectively, when the variation in d_{Se} increases to 2 %. This range of variation in g_{av} due to thickness non-uniformity is certainly within the capability of gain correction and the dynamic range of the electronic circuits of FPI. With further increase in d_{Se} to 4 %, the value for g_{av} will decrease from the original setting of 46, 25 and 12 to 15, 10 and 6, respectively, which is a gain non-uniformity of 2 to 3 folds. Although the change in g_{av} is significant, it is not expected to cause significant degradation in the DQE performance, as can be seen in the example of $g_{av} = 46$ and 12 shown in Figure 6 (a). Hence we can conclude that a thickness non-uniformity of 2 % is desirable for a HARP layer, and a non-uniformity of 4 % is still reasonable.

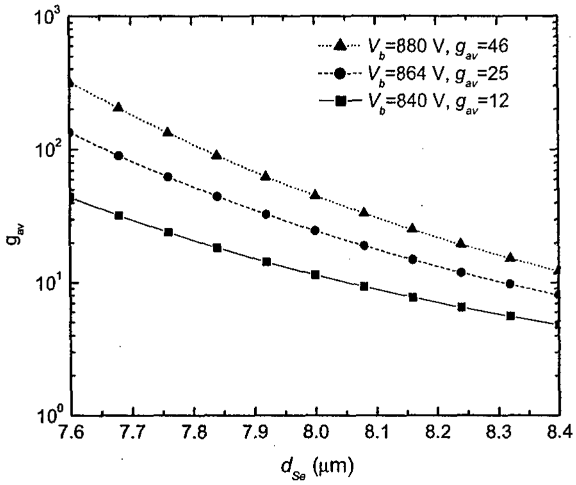

Figure 8: The avalanche gain g_{av} as a function of variation in the thickness of HARP under a constant bias potential V_b.

CONCLUSIONS

The feasibility of a new concept of indirect conversion flat-panel detector with avalanche gain is being investigated. The avalanche gain and quantum efficiency of an 8 μm thick HARP layer was investigated as a function of E_{Se}. The characteristics of HARP were applied to a cascaded linear system to determine the operating conditions for x-ray imaging. Our results showed that by varying the avalanche gain between 2 and 46, x-ray quantum noise limited performance and a wide dynamic range can be obtained for typical detector parameters chosen for an R/F detector. Due to the rapid increase in g_{av} as a function of E_{Se}, it is desirable to keep the thickness uniformity of a HARP layer within 2 %, which could keep the variation in g_{av} within ~ 40 %.

ACKNOWLEDGEMENTS

We gratefully acknowledge financial support from the NIH (1 R01 EB002655-01) and the U.S. Army Breast Cancer Research Program (W81XWH-04-1-0554).

REFERENCES

[1] Wei Zhao, D. C. Hunt, Kenkichi Tanioka and J. A. Rowlands, "Indirect flat-panel detectors with avalanche gain", Proc. SPIE **5368**, 150-161 (2004)

[2] T. Ohshima, K. Tsuji, K. Sameshima, T. Hirai, K. Shidara and K. Taketoshi, "Excess noise in amorphous selenium avalanche photodiodes", Japan. J. Appl. Phys. **30**, L1071-L1074 (1991)

[3] K. Tanioka, J. Yamazaki, K. Shidara, K. Taketoshi, T. Kawamura, T. Hirai and Y. Takasaki, "Avalanche-mode amorphous selenium photoconductive target camera tube", Adv. Electron. Electron Phys. **74**, 379-387 (1988)

[4] D. M. Pai and R. C. Enck, "Onsager mechanism of photogeneration in amorphous selenium", Phys. Rev. B **11**, 5163-5174 (1975)

[5] K. Tsuji, Y. Takasaki, T. Hiri, J. Yamazaki and K. Tanioka, "Avalanche phenomenon in amorphous selenium", Optoelectron. Devices Technol., **9**, 367-378 (1994)

[6] R. J. McIntyre, "Multiplication noise in uniform avalanche diodes", IEEE Trans. Electron Devices, **13**, 164-168 (1966)

[7] Wei Zhao, Goran Ristic and J. A. Rowlands, ""Inherent Imaging Performance of Cesium Iodide Scintillators", Med. Phys. **31**, 2594-2605 (2004)

[8] Wei Zhao, J. Law, D. Waechter, Z. Huang and J. A. Rowlands, "Digital Radiology Using Active Matrix Readout of Amorphous Selenium: Detectors with High Voltage Protection", Med. Phys. **25**, 539-549 (1998).

Indirect flat-panel detector with avalanche gain: Fundamental feasibility investigation for SHARP-AMFPI (Scintillator HARP Active Matrix Flat Panel Imager)

Wei Zhao and Dan Li

Department of Radiology, State University of New York at Stony Brook

L-4, 120 Health Sciences Center

Stony Brook, New York 11793-8460

Alla Reznik, B. J. M. Lui, D. C. Hunt and J. A. Rowlands

Imaging Research, Sunnybrook and Women's Health Sciences Center

2075 Bayview Avenue

Toronto, Ontario, Canada M4N 3M5

Yuji Ohkawa and Kenkichi Tanioka

Advanced Imaging Devices Research Division

Science & Technical Research Laboratories

Japan Broadcasting Corporation

1-10-11 Kinuta, Setagaya-ku, Tokyo 157-8510 Japan

ABSTRACT

An indirect flat-panel imager (FPI) with avalanche gain is being investigated for low-dose x-ray imaging. It is made by optically coupling a structured x-ray scintillator CsI(Tl) to an amorphous selenium (a-Se) avalanche photoconductor called HARP (High-gain Avalanche Rushing Photoconductor). The final electronic image is read out using an active matrix array of thin film transistors (TFT). We call the proposed detector SHARP-AMFPI (Scintillator HARP Active Matrix Flat Panel Imager). The advantage of the SHARP-AMFPI is its programmable gain, which can be turned on during low dose fluoroscopy to overcome electronic noise, and turned off during high dose radiography to avoid pixel saturation. The purpose of this paper is to investigate the important design considerations for SHARP-AMFPI such as avalanche gain, which depends on both the thickness d_{Se} and the applied electric field E_{Se} of the HARP layer. To determine the optimal design parameter and operational conditions for HARP, we measured the E_{Se} dependence of both avalanche gain and optical quantum efficiency of an 8 μm HARP layer. The results were used in a physical model of HARP as well as a linear cascaded model of the FPI to determine the following x-ray imaging properties in both the avalanche and non-avalanche modes as a function of E_{Se}: (1) total gain (which is the product of avalanche gain and optical quantum efficiency); (2) linearity; (3) dynamic range; and (4) gain non-uniformity resulting from thickness non-uniformity; and (5) effects of direct x-ray interaction in HARP. Our results showed that a HARP layer thickness of 8 μm can provide adequate avalanche gain and sufficient dynamic range for x-ray imaging applications to permit quantum limited operation over the range of exposures needed for radiography and fluoroscopy.

Key words: flat-panel detectors, avalanche gain, amorphous selenium, cesium iodide.

I. INTRODUCTION

An active matrix flat-panel imager (AMFPI) based on thin film transistor (TFT) arrays is the most promising technology for digital x-ray imaging due to its compact size, rapid readout and superior performance compared to screen-films.[1] Based on the materials used for x-ray detection, AMFPI are categorized as either *direct* or *indirect* based on the materials used for x-ray detection (x-ray photoconductors or scintillators, respectively). Direct AMFPI have the advantages of higher image resolution and a simpler TFT array structure that can be manufactured in a standard facility for active matrix liquid crystal displays (AMLCD). Despite their differences, both types of AMFPI offer better image quality than screen-films and computed radiography (CR).

However before AMFPI can equal the performance of the x-ray image intensifier (XRII) in fluoroscopy, two major difficulties must be overcome: (i) the ability to produce good image quality at very low dose, such as in the dark part of a fluoroscopy image (~0.1 μR per frame),[2,3] and (ii) the ability to produce images at a high frame rate without artifacts, especially when the radiation exposure is switched from radiographic to fluoroscopic.[4,5] Even in well established radiographic applications, AMFPI are facing new challenges because their rapid readout and freedom from geometric distortion have generated a renewed interest in advanced clinical applications. One example is digital tomosynthesis,[6] in which a rapid sequence of images is taken from different angles, and tomographic slices at different depths of the patient anatomy are reconstructed. The application of AMFPI in cone-beam computed tomography[7,8] (CT) is also under intensive investigation. Such advanced applications of AMFPI pose new challenges for the development of the next generation of detectors, primarily regarding the ability of AMFPI to generate high quality images that are quantum noise limited and free from artifacts at low x-ray exposures and high frame rates. It has been shown that the detective quantum efficiency (DQE) of AMFPI is inferior to XRII at the lower end of the dose range (0.1 – 1 μR per frame) encountered in fluoroscopy.[9] In mammography, the detector is not x-ray quantum noise limited behind dense breast, where the average exposure is ~1 mR, and the DQE of the detector is severely compromised by the electronic noise.[10,11].

The strategies for improving the low dose performance of AMFPI can be divided into two categories: one is to increase the x-ray to image charge conversion gain so that the x-ray quantum noise can overcome the electronic noise; and the other is to decrease the electronic noise. These strategies are common to both types of AMFPI since they have approximately the same conversion gain and pixel electronic noise.[1] Several investigations are taking place to increase the gain for direct AMFPI by developing other x-ray photoconductors. Promising results have been shown for lead iodide (PbI_2) and mercuric iodide (HgI_2).[12] The conversion gain of these two materials is 5-7 times higher than that of current systems. The challenges for this technology are to develop deposition techniques for large area detectors with good imaging properties, and to ensure that both electrons and holes have adequate range to reduce the probability of charge trapping.[13] To reduce electronic noise, several investigators have proposed advanced pixel designs, which incorporate pixel amplification by adding at least two more TFTs at each pixel.[14,15,16] The electronic noise can thus be reduced to ~700 electrons per pixel, which is a factor of 2-4 lower than existing AMFPI. A challenge for this approach is the practical implementation of the complex pixel design over a large area with consistent and uniform imaging performance because each pixel operates as an analog amplifier circuit as opposed to the simple switching device (digital) in existing AMFPI. Due to these practical challenges none of the above approaches for increased gain and reduced electronic noise has been implemented in commercial large area AMFPI.

We are proposing a new concept of AMFPI by adding avalanche gain to an indirect AMFPI, as shown in Figure 1. The optical photons emitted from the CsI layer upon absorption of x-rays are detected and amplified by an avalanche a-Se photoconductor called HARP (High-gain Avalanche Rushing Photoconductor). Light photons absorbed by the HARP layer generate electron-hole pairs near the top interface (<0.1 μm). Under a sufficiently high E_{Se} (produced by applying positive voltage on the top bias electrode of a-Se), holes moving towards the bottom surface will undergo avalanche multiplication and create more holes and electrons. The avalanche gain g_{av} ranges from unity up to ~1000 times depending on E_{Se} and the thickness of the a-Se layer, d_{Se}.[17] The electrons move to the top bias electrode while holes are collected by the pixel electrodes and form a charge image, which is read out with a two-dimensional array of TFTs, similar to that in existing AMFPI. The proposed detector is named SHARP-AMFPI (Scintillator-HARP Active Matrix Flat-panel Imager). Rougeot and Possin have suggested a similar concept,[18] but it has not been implemented. The only other indirect AMFPI approach involving an a-Se photoconductor as an optical sensor did not have avalanche gain.[19]

Compared to existing indirect FPI, SHARP-AMFPI has the following advantages: (1) x-ray quantum noise limited at a much lower x-ray exposure level; (2) better temporal performance, i.e. lower lag and ghosting because of the lower trap density in a-Se (compared to a-Si) and the much higher electric field E_{Se}; (3) compatibility with standard TFT array manufacturing facility for AMLCD; (4) ability to use high-resolution (HR) type CsI, which cannot be used in existing AMFPI due to its lower light output. Compared to the high conversion gain x-ray photoconductors being developed for direct FPI, the proposed detector has the following advantages: (1) *programmable* gain by changing the electric field E_{Se} as opposed to the fixed high conversion gain of HgI_2 or PbI_2. One of the practical problems of having a fixed high gain is that the large signal charge (at high exposure) requires a large pixel storage capacitor (>15 pF), which is impractical to make especially for small pixel sizes. This means that a detector that is optimized for low dose (fluoroscopic) x-ray imaging applications will not work properly at high radiographic dose levels. With SHARP-AMFPI, by appropriately decreasing the E_{Se} during high exposure applications, the signal charge is comparable to that at low dose with avalanche gain. This simplifies the TFT array pixel design and permits a detector with wide dynamic range. (2) better temporal performance because both charge carriers in a-Se have adequate range and the probability of charge trapping is low. This is in contrast to the very short range of one type of carriers in PbI_2 (electrons) and HgI_2 (holes) which results in significant charge trapping and ghosting. The advantages described above make the proposed detector suitable for all x-ray imaging modalities (i.e. radiography and fluoroscopy). The purpose of this paper is to investigate the important design parameters for HARP and to establish the operational conditions that ensure adequate dynamic range for both fluoroscopy and radiography.

Since avalanche multiplication in a-Se was discovered over a decade ago the HARP video tube, which consist of a HARP layer read out with a scanning electron beam, has been commercialized for high sensitivity and high definition television applications. Stable and uniform avalanche multiplication has been demonstrated with very little added noise.[20] No correction for fixed pattern noise is necessary. The electric field E_{Se} under which avalanche multiplication occurs is > 70 V/um, which is an order of magnitude higher than that typically used in direct AMFPI incorporating thick a-Se layers. To sustain E_{Se} of this high magnitude without a significant increase in dark current due to charge injection from the bias electrodes, blocking layers are required for both electrode interfaces. As shown in Figure 1 (b), the HARP sensor is a multi-layer structure.[17] It contains a transparent indium tin oxide (ITO) electrode which is biased positively during imaging, followed by a thin layer (~20 nm) of cerium oxide (CeO_2) and a thin layer of lithium fluoride (LiF) doped a-Se to block injection of holes from the ITO. The intrinsic a-Se photoconductor is from 0.5 to 35 μm thick depending on the desired avalanche gain. The bottom interface of the HARP structure is a sub-micron thin layer of antimony tri-sulfide (Sb_2S_3), which is used to block electron injection from the negative bias electrode (i.e. pixel electrodes of the TFT array). Since the mobility of holes in a-Se is more than 30 times higher than that of electrons, only holes create a significant number of new carriers by impact ionization. Hence it is essential for light photons to enter from the positive bias electrode.

Our previous calculation using a preliminary linear system model of indirect FPI with avalanche gain predicted that an avalanche gain of $g_{av} = 20$ is needed to produce x-ray quantum noise limited performance for fluoroscopy and low dose mammography (tomosynthesis).[21] This requires a HARP layer thickness of 4 μm or above. For the present paper we investigated the effects of the optical imaging properties of HARP on the x-ray imaging performance of SHARP-AMFPI, so that appropriate design parameters and operational conditions could be determined. We measured the E_{Se} dependence of both avalanche gain and optical quantum efficiency of an 8 μm HARP layer. The results were used in a physical model of HARP as well as a linear cascaded model of the FPI to determine the following x-ray imaging properties in both the avalanche and non-avalanche modes as a function of d_{Se} and E_{Se}: (1) total gain (which is the product of avalanche gain and optical quantum efficiency); (2) linearity; (3) dynamic range; (4) gain non-uniformity resulting from thickness non-uniformity; and (5) the effects of direct x-ray interaction in HARP.

II. PHOTOSENSITIVITY OF HARP

The x-ray imaging performance of indirect FPI with avalanche gain relies on the photosensitivity of HARP. Understanding the dependence of photosensitivity on E_{Se} and the layer thickness d_{Se} is crucial for guiding the choice of HARP design parameters and operational conditions for both the avalanche and non-avalanche modes. In this section, we will first present the experimental method and results of the HARP photosensitivity measurements, and then describe the theory of E_{Se} dependence of photosensitivity, which is proportional to both the optical quantum efficiency (QE) η and the avalanche gain g_{av}. The theory and experimental data will then be used to determine η and g_{av} as a function of E_{Se} in the context of x-ray imaging.

A. Experimental Measurement of Photosensitivity

1. Method

The experimental apparatus for photosensitivity measurement is shown in Figure 2. A grating monochromator was used to generate optical photons of a single wavelength λ. The values of λ used in our experiments were in the ranged of 380-600 nm. The intensity of the output beam was attenuated by neutral-density (ND) filters. A beamsplitter was used to direct a fraction (90 %) of the attenuated beam to a silicon (Si) photodiode (PD), which was used to monitor the beam intensity during the experiment. The optical photons passing directly through the beam splitter (10 %) were detected by the HARP video tube. Before photosensitivity measurements the input light intensity to the HARP was calibrated such that a constant input power was used for each λ. This was achieved by adjustment of the ND filters based on the light intensity monitored by the Si PD.

For each λ and E_{Se}, the signal current S from the HARP tube was recorded. The photosensitivity was quantified as the number of signal charge carriers generated per absorbed light photon. This is referred to as the effective quantum efficiency η^*, and it is the product of η and g_{av}. The values of η^* were experimentally determined from the measurement of HARP tube current S using:

$$\eta^* = \frac{S/e}{IT/h\nu} \quad (2)$$

where e is the electron charge, I is the HARP input light intensity power given in Watts (W), $h\nu$ is the energy of each incident photon, and T is the fraction of the photons incident on the HARP tube reaching the a-Se layer. The correction factor T represents the light attenuation by the glass faceplate, the ITO bias electrode and the CeO_2 blocking layer for HARP. The value of T is a function of the wavelength λ and was experimentally measured.

2. *Measurement results:*

The measured effective quantum efficiency η^* is shown in Figure 3 as a function of E_{Se} for an 8 μm thick HARP layer. For blue light (λ=400 nm), η^* reaches a plateau at $E_{Se} > 20$ V/μm. This corresponds to a saturation of optical quantum efficiency η at unity. With further increase in E_{Se} to > 80 V/μm, η^* starts to increase again, which shows the onset of avalanche. However for green light, the E_{Se} dependence of η^* is quite different. As shown in Figure 3 for λ=540 nm, which is the peak of the emission spectrum of CsI (Tl), η^* starts at a much smaller value compared to that for blue light. It then increases continuously with E_{Se} without reaching a plateau before avalanche begins at ~80

V/μm. This is because the optical η for green light is lower and does not reach unity until E_{Se} is well into the range of avalanche multiplication. To choose the proper operational condition for HARP in different x-ray imaging applications, we need to understand separately the E_{Se} dependence of η and g_{av}. This will be discussed in section IIB.

B. Determination of Quantum Efficiency and Avalanche Gain

The effective quantum efficiency η^* of HARP is proportional to both η and g_{av}. The value of η in a-Se depends on both E_{Se} and the wavelength λ of the incident photon. It was found by Pai and Enck that the E_{Se} and λ dependence of photogeneration in a-Se follow the Onsager mechanism.[22] Onsager theory states that every absorbed photon creates a pair of thermalized carriers bound by their Coulombic attraction. The initial separation r_0 of the charge pair increases with incident photon energy. The probability of dissociation for the bound pairs into free carriers increases with r_0 and the applied external field E_{Se} with the relationship:

$$\begin{aligned} &\eta = \phi_0 \frac{kT}{eE_{Se}r_0} e^{-A} e^{-eE_{Se}r_0/kT} \sum_{m=0}^{\infty} \frac{A^m}{m!} \sum_{n=0}^{\infty} \sum_{l=m+n+1}^{\infty} \left(\frac{eE_{Se}r_0}{kT}\right)^l \frac{1}{l!}, \\ &\text{with} \quad A = \frac{e^2}{4\pi\varepsilon\varepsilon_0 kT} \end{aligned} \qquad (1)$$

where ϕ_0 is defined as the efficiency of production of thermalized charge pairs per absorbed photon and is independent of E_{Se}. Pai and Enck showed that the room temperature measurement of η can be best fitted with the expression in Eq. 1 using ϕ_0=1 and r_0 in the range between 0.8 – 7.0 nm for λ values between 620 and 400 nm. For the rest of the discussion in this paper, we will focus on λ=540 nm, which is the peak of the emission spectrum for CsI (Tl). Shown in Figure 4 are the values of η calculated using Eq. 1 and r_0 = 1.7 nm. Also plotted in Figure 4 are the η^* measured at the same wavelength for $d_{Se} = 8$ μm. These results show that the Onsager theory provides a reasonable prediction for the E_{Se} dependence of η^* in HARP for $E_{Se} \leq 70$ where $g_{av} = 1$. The calculated η using Onsager theory was then divided into the measured η^* so that the E_{Se} dependence of avalanche gain g_{av} can be obtained. The results are shown in Figure 5 (a), where $g_{av} = 46$ at $E_{Se} = 110$ V/μm. Figure 5 (a) shows that g_{av} increases very rapidly with E_{Se}, hence choosing the appropriate E_{Se} for HARP is crucial. To determine the x-ray response of SHARP-AMFPI it is necessary to understand the continuous dependence of g_{av} on E_{Se} because as image charge accumulates on the pixels, the voltage drop across the HARP layer will decrease. This change in E_{Se} will produce a corresponding change in g_{av} and affect the x-ray sensitivity, linearity and dynamic range of the FPI.

The avalanche gain characteristics in HARP have been investigated as a function of d_{Se} and E_{Se}.[23] According to the theory of avalanche multiplication,[24] when E_{Se} across the thickness d_{Se} is uniform, and the distance through which avalanche occurs is equal to d_{Se} (which is true for an 8 μm HARP because photons are absorbed within 0.1 μm at the entrance side of the a-Se layer), g_{av} is given by:

$$g_{av} = \frac{(\beta-\alpha)e^{d_{Se}(\beta-\alpha)}}{\beta-\alpha e^{d_{Se}(\beta-\alpha)}} \qquad (2)$$

where α and β are the impact ionization coefficients of electrons and holes, respectively. The value of β is much greater than α since in a-Se the drift mobility of holes (0.18 cm^2/Vs) is much higher than that of electrons (0.003 cm^2/Vs). This is why in HARP light always enters from the positive bias electrode to maximize avalanche gain. Under the assumption that the contribution of electrons to avalanche gain is negligible, Eq. 2 can be simplified to:

$$g_{av} = e^{d_{Se}\beta} \qquad (3)$$

with β given by:

$$\beta = \beta_1 e^{\frac{-\beta_2}{E_{Se}}}. \tag{4}$$

The values for β_1 and β_2 can be determined by curve fitting of experimental measurement of g_{av}. By taking the logarithms of both sides of Eq. 3 twice, we obtain:

$$\ln(\ln g_{av}) = \ln(\beta_1 d_{Se}) - \frac{\beta_2}{E_{Se}}, \tag{5}$$

which indicates that the quantity $\ln(\ln g_{av})$ is linearly related to $1/E_{Se}$. Shown in Figure 5 (b) is the experimentally determined g_{av} data from Figure 5(a) replotted in the form of $\ln(\ln g_{av})$ as a function of $1/E_{Se}$. The best linear fit to the experimental data is also shown in Figure 5 (b). From the intercept and the slope of the fitted line we obtained β_1=5.5 x 10^3 μm^{-1} and β_2 = 1.029 x 10^3 V/μm. Using these β_1 and β_2 values and the analytical expression for g_{av} shown in Eqs. 3 and 4, the fitted g_{av} values were calculated and are shown in Figure 5 (a). It shows that the calculated g_{av} using the fitted parameters agrees well with experimentally determined g_{av} for $E_{Se} \leq 110$ V/μm. Hence the fitted parameters β_1 and β_2 will be used in the following investigation of the potential x-ray imaging performance of SHARP-AMFPI.

III. POTENTIAL X-RAY IMAGING PERFORMANCE

A. Cascaded Linear System Model for SHARP-AMFPI

Previously we have developed a cascaded linear system model for indirect FPI with avalanche gain.[21] This preliminary investigation did not include K-fluorescence reabsorption in CsI or direct x-ray interaction in HARP. We showed that the DQE(*f*) is related to the avalanche gain g_{av} through:

$$\mathrm{DQE}(f)=\frac{T_b^2(f)T_c^2(f)T_a^2(f)}{[\frac{1}{\eta_x A_S}T_b^2(f)T_c^2(f)+\frac{(2g_{av}-1)}{g_{av}g\eta_x\alpha\eta}]T_a^2(f)+\frac{S_n}{(a_p^2 g_{av}g\eta_x\alpha\eta)^2 q_0}}, \qquad (6)$$

where q_0 is the number of incident x-ray photons per unit area, $T_b(f)$, $T_c(f)$, and $T_a(f)$ are the MTFs due to blur in CsI, the optical coupling between CsI and HARP, and the pixel aperture function, respectively. A_S, η_x, and g are the Swank factor, x-ray quantum absorption efficiency and x-ray to photon conversion gain of the CsI layer, respectively. The factors related to the TFT array are the electronic noise S_n and the pixel width a_p. The denominator of Eq. 6 is the dose normalized NPS. The first term is the x-ray quantum noise, the second term is the secondary quantum noise associated with the variance in gain in the conversion and the avalanche process, and the third term is the contribution from the electronic noise of the TFT array. This expression shows that the electronic noise is more important at low dose, and is inversely proportional to g_{av}^2. Therefore introducing avalanche gain is an effective method for reducing noise at low dose. The secondary quantum noise for $g_{av} >> 1$ is approximately twice that for $g_{av} = 1$, assuming η is the same in both cases. This excess secondary quantum noise is the penalty for avalanche gain. However for SHARP-AMFPI with high conversion gain g and efficient optical coupling between CsI and HARP, i.e. $g\eta_x\alpha\eta \gg 2$, the secondary quantum noise is negligible compared to the x-ray quantum noise. Hence the DQE of SHARP-AMFPI will not be degraded by the noise associated with avalanche gain. This has been demonstrated experimentally by coupling a HARP tube to the output of an x-ray image intensifier (XRII) and measuring the DQE as a function of avalanche gain g_{av}.[25] It was shown that DQE remains essentially constant as a function of g_{av} (with electronic noise negligible in all cases).

In a later investigation of the inherent imaging performance of CsI layers, we included the effect of K-fluorescence reabsorption of CsI in the cascaded linear system model for indirect AMFPI.[26] Our results showed that the K-fluorescence reabsorption in CsI has two effects: (1) degradation of the Swank factor for x-ray energies above the K-edges; and (2) additional image blur, which accounts for a drop in presampling MTF of 20 – 30 % at 10 cycles/mm for CsI thickness between 150 – 600 μm. For the present paper, a more complete cascaded linear system model was developed that includes the effect of direct x-ray interaction in HARP. Shown in Figure 6 are the serial and parallel cascaded stages involved in the formation of an x-ray image by SHARP-AMFPI. Each stage can be categorized as one of the following six processes: (1) gain or selection, (2) stochastic blurring, (3) deterministic blurring, (4) aliasing, (5) addition, and (6) parallel processes. There are two parallel processes: one associated with the probability of K-fluorescence generation and reabsorption in CsI, and the other with direct interaction of x-rays in the HARP layer. We have previously described in detail the transfer of spatial frequency dependent signal, $\Phi(f)$, and NPS, $S(f)$ through all the stages except direct x-ray interaction in the HARP layer. This process will be described in Section C of this paper.

Using the cascaded linear system model shown in Figure 6, we investigated two important aspects of the x-ray imaging performance of SHARP-AMFPI. One is the pixel x-ray response of the detector, i.e. the linearity and dynamic range, for both the avalanche and non-avalanche operational modes; the other is the effect of direct x-ray interaction in HARP on the DQE of the detector. These will be described in Sections B and C, respectively.

B. Pixel X-ray Response

In this section, we will apply the E_{Se} dependence of g_{av} and η derived previously in Section II (B) to the cascaded linear system model to determine the x-ray response of SHARP-AMFPI. Due to the difference in resolution and avalanche gain requirement for mammography and radiography/fluoroscopy (R/F), the calculation will be performed separately for these two imaging applications. From the cascaded linear system model the mean signal from each pixel of the detector is given by:

$$\Phi_s = \frac{a_p{}^2 \alpha \eta g_{av} E_{ab}}{W} \tag{7}$$

where W is the energy required to generate an optical photon in CsI, and E_{ab} is the x-ray energy absorbed by CsI per unit area. E_{ab} includes contributions from all three parallel paths associated with K-fluorescence:

$$E_{ab} = \sum_E q_0(E)\eta_x(E)[(1-P_k)E + (E-E_k)P_k + E_k P_k f_k] \tag{8}$$

where $q_0(E)$ is the incident x-ray photons per unit area as a function of energy E for a given x-ray spectrum, P_k is the probability of K-fluorescence, E_k is the energy of the K-fluorescence photon, and f_k is the fraction of K-fluorescence reabsorbed in the CsI layer. Each of the K-fluorescence related terms in Eq. 8 were determined separately for the K_α and K_β photons from both Cs and I atoms and integrated to obtain the final result of E_{ab}.

Our previous investigation of the inherent x-ray imaging performance of CsI (Tl) has shown that the high resolution (HR) type has essentially no depth dependent blur and as a result provides better DQE(f) at high spatial frequencies compared to the CsI optimized for high light output (HL).^{26} This was achieved at the cost of a lower light output (60 %) for the HR compared to the HL CsI. For the calculation in this paper, we used 150 μm HR CsI for mammography and 600 μm HL CsI for R/F applications. Our previously measured values for A_S, W and presampling MTF of these CsI layers were used in the cascaded linear system model. Since we have not yet implemented the depth dependent blur of CsI in our cascaded linear system model, the DQE(f) at high frequencies for the 600 μm HL CsI layer (for R/F) will be overestimated. Table I summarizes the detector parameters and HARP operating conditions chosen for each application. For mammography, we consider two different image acquisition modes: screening mammography and tomosynthesis (where several images of the breast are acquired from different viewing angles for tomographic reconstruction of 3D images).

1. Radiography/Fluoroscopy

Shown in Figure 7 (a) is the DQE(f) calculated using the cascaded linear system model for the detector with different g_{av} settings. The calculation was performed for the lowest exposure in fluoroscopy (0.1 μR), where the detector performance is most susceptible to electronic noise. It shows that $g_{av} = 46$ is sufficient to bring the DQE(f) to its theoretical limit (i.e. a detector without electronic noise). The DQE(f) for the next highest $g_{av} = 12$ measured at $E_{Se} = 105$ V/μm also provides reasonable DQE. Thus an E_{Se} between 105 and 110 V/μm will be adequate for fluoroscopy. Figure 7 (b) shows the DQE(f) calculated for the lowest radiographic exposure of 30 μR. It shows that $E_{Se} = 95$ V/μm can provide sufficient η (0.31) and g_{av} (2.3). Hence the E_{Se} chosen in Table I is adequate for the dual-mode operation of a R/F detector.

Shown in Figure 8 are the calculated pixel x-ray responses for the R/F detector under two different operational conditions. Here we assumed that the dominant pixel capacitance is the capacitance of the HARP layer. This condition results in the largest drop in the potential across the HARP layer for a given x-ray exposure, and creates the biggest effect on linearity. Figure 8 (a) shows that for fluoroscopy, the initial $E_{Se} = 110$ V/μm provides a g_{av} of 46. Within the regular exposure range of 0.1 – 10 μR per frame in fluoroscopy, the detector has good linearity, i.e. an essentially constant g_{av}. With further increase in exposure, which corresponds to the exposure near or beyond the edge of the human body, the x-ray response becomes sublinear with a decrease in g_{av}. This decrease in g_{av} ensures a wide dynamic range for the detector because there is no "hard" saturation. The pixel potential will continue to increase as a function of x-ray exposure until it reaches the predetermined V_{max} for high voltage protection of the TFTs. The method for high voltage protection was described in detail elsewhere.[27]. The pixel potential for the exposure of 1 mR in the fluoroscopy mode is $V_P =$ 56 V, which is safe for a-Si TFTs. Figure 8 (b) shows that with a much lower $g_{av} = 2.3$ programmed for radiography, the detector response for the regular exposure range of 30 μR – 3 mR is essentially linear with very little change in g_{av}. Comparing Figures 8 (a) and (b), the image charge on the pixel is in the same range despite their large difference in exposure range. This demonstrates the wide dynamic range (over 5 orders of magnitude) of the detector that is made possible by varying g_{av} for different x-ray imaging applications. This is an advantage over detectors with constant high gain, which have the problem of pixel saturation for radiographic applications.

2. Mammography

Figure 9 (a) and (b) shows the DQE calculated for mammography using the detector parameters and operating conditions listed in Table I for tomosynthesis and screening applications. Figure 9 shows that the choice of E_{Se} for both operational modes is adequate to achieve the theoretical limit of DQE without electronic noise.

The pixel x-ray response for mammography was calculated using Eq. 7 and the results are shown in Figures 10 (a) and (b) for tomosynthesis and screening mammography, respectively. Two sets of curves are shown in each graph of Figure 10, one without additional pixel storage capacitance, and the other with a storage capacitor of $C_{st} = 0.5$ pF. The minimum exposure in each graph of Figure 10 corresponds to the detector exposure behind dense breast tissue, and the maximum corresponds to raw exposure. Figure 10 shows that when there is no additional storage capacitance, the signal increases sublinearly as a function of the x-ray exposure. This is because the pixel capacitance due to the HARP layer for mammography is only ~0.03 pF with $a_p = 70$ μm, which is much smaller than that for the R/F detector (0.28 pF). Hence the signal accumulated on each pixel creates a much more significant drop in E_{Se}, which causes a rapid decrease in g_{av}. The maximum image charge shown in Figures 10 (a) and 10 (b) corresponds to a pixel potential of ~100 and 210 V, respectively. These potentials exceed the maximum safe voltage for the TFTs. One method for alleviating this problem while maintaining the same dynamic range is to add a pixel storage capacitance C_{st}. With $C_{st} = 0.5$ pF, the pixel potential rises much more slowly and the x-ray response of the detector becomes more linear, as shown in Figure 10. The pixel potential corresponding to the maximum exposures in Figures 10 (a) and (b) is only 25 and 50 V, respectively, both of which are safe for the TFTs.

C. Direct X-ray Interaction in HARP

In indirect AMFPI using phosphor and a-Si photodiodes, direct interaction of x-rays in the photodiodes produces additional noise.[28] This is because the x-ray to charge conversion gain in the photodiodes is 45 times higher than that in the phosphors, and therefore each direct interaction x-ray produces much higher signal (and noise) than that absorbed in the phosphor. For our proposed detector, the HARP sensor (e.g. $d_{Se} = 8$ μm) is much thicker than the a-Si photodiodes (~ 1 μm) in existing indirect FPI, hence there will be more direct x-ray interaction events. Fortunately the x-ray to charge conversion gain in HARP[29] ($W_{Se} = 16$ eV at $E_{Se} = 100$ V) is very similar to that in CsI, thus direct x-ray interaction in HARP is not expected to add additional noise at low spatial frequencies. At high spatial frequencies, however, the effect of direct x-ray interaction could be more significant. This is because both the signal and the NPS due to x-rays absorbed in CsI decrease as a function of spatial frequency due to blur in CsI, whereas the signal and NPS due to direct x-ray interaction in HARP are essentially white (without including the effect of K-fluorescence). Furthermore, when HARP is operated in the avalanche mode, the x-rays absorbed by HARP will experience different avalanche gain depending on their depth of interaction. As shown in Figure 11, x-rays absorbed in HARP at a depth x from the top (light entrance) interface have an effective thickness for avalanche multiplication of $(d_{Se} - x)$. This could lead to a depth dependent variation in g_{av}, and add additional noise.[30] In the following we will derive the propagation of signal and noise due to direct x-ray interaction in HARP using the flow diagram shown in Figure 6, and investigate its effect on the DQE of SHARP-AMFPI.

1. Signal and noise propagation for direct x-ray interaction

As shown in Figure 6, the input to the parallel path for direct x-ray interaction in HARP is the x-rays transmitted through the CsI layer, q_1, which is a function of x-ray energy. For clarity we assume a monoenergetic x-ray beam in the following derivation of theory, although we used the full x-ray spectrum in our calculation of direct x-ray interaction. We ignored the effect of K-fluorescence reabsorption in HARP. Under this assumption, both the signal and NPS for direct x-ray interaction are white prior to the pixel aperture function, hence we could omit the frequency dependence in the following derivation. The x-ray signal produced at depth x into the HARP layer by a small thickness dx of a-Se is given by:

$$\Phi(x) = q_1 e^{-\mu x} g_{av}(x) g_{Se} \mu \, dx\,, \tag{9}$$

where μ is the linear attenuation coefficient of a-Se, and g_{Se} is the average x-ray to charge conversion gain which is equal to E/W_{Se}. The depth dependence in g_{av} can be derived from Eq. 3 as $g_{av}(x) = \exp[\beta(d_{Se} - x)]$. The NPS due to direct interaction as a function of depth, $S(x)$, is given by:[30]

$$S(x) = q_1 \, \mathrm{e}^{-\mu x}[(g_{Se}{}^2 + \sigma^2{}_{g_{Se}}) g_{av}{}^2(x) + g_{Se} \sigma^2{}_{g_{av}}(x)] \mu dx\,. \tag{10}$$

Integrating both Eqs. 9 and 10 with respect to x from 0 to d_{Se}, we obtain the total signal and NPS due to direct x-ray interaction:

$$\Phi = \frac{q_1 \mu g_{Se}(e^{\beta d_{Se}} - e^{-\mu d_{Se}})}{\mu + \beta} \tag{11}$$

and:

$$S = \frac{q_1 \mu (g_{Se}{}^2 + \sigma^2{}_{g_{Se}})(e^{2\beta d_{Se}} - e^{-\mu d_{Se}})}{\mu + 2\beta}\,. \tag{12}$$

2. Calculation results

Using Eqs. 11 and 12, we calculated the contribution to the total signal and NPS by the direct interaction of x-rays in HARP using the parameters shown in Table I for an R/F detector. With a RQA5 x-ray spectrum and a 600 μm HL layer of CsI, the fraction of x-rays transmitted through the CsI layer is 13.2%, out of which ~1 % is absorbed by the HARP layer. Shown in Figure 12 (a) is a comparison between the presampling signal spectra (before the pixel aperture function) due to x-rays absorbed in CsI and direct x-ray interaction in HARP. At low frequencies, the signal due to direct x-ray interaction is less than 0.2 % of that due to x-ray absorbed in CsI. This is consistent with the difference in x-ray quantum efficiency between CsI and HARP. At high frequencies (e.g. 5 cycles/mm), the signal from CsI decreases due to the blur in CsI, however the signal from direct x-ray interaction in HARP stays constant. But the latter is still negligible. Shown in Figure 12 (b) is the NPS (before pixel aperture function) comparison. At 5 cycles/mm, the NPS due to direct x-ray interaction becomes significant (~17 % of the NPS due to CsI). However below the Nyquist frequency of 2.5 cycles/mm, it is still negligible (< 3 %). This is why there is no significant change in DQE after including the direct x-ray interaction events in HARP, as shown in Figure 13. Therefore we can conclude that direct x-ray interaction in HARP in an indirect FPI with avalanche gain has no degradation effect on DQE of the detector.

IV. EFFECT OF HARP THICKNESS UNIFORMITY

An important issue for making a large area HARP is its thickness uniformity. Currently HARP films can be made very uniform for an area of 1-2" in diameter with essentially no visible gain variation in the images. The images currently produced by HARP for broadcast applications do not require any gain uniformity correction. The area of HARP needs to be increased significantly for x-ray imaging applications. Uniform, large area a-Se films have already been developed for direct FPI, however the uniformity requirement for HARP in indirect FPI with avalanche gain is expected to be much higher. In this section we will derive the relationship between thickness non-uniformity and gain non-uniformity for HARP sensors so that the results can be used as a guideline for engineering of large area HARP layers for FPI.

A. Relationship between HARP Avalanche Gain and Thickness Uniformity

During the operation of HARP, a constant potential V_b is applied to the top ITO bias electrode, as shown in Figure 1 (b). After each image readout, the TFT array resets the potential on pixel electrodes to $V_p = 0$ V. A non-uniformity in the thickness of HARP will result in a variation in E_{Se} and hence a spatial non-uniformity in gain. An increase in d_{Se} under a constant V_b causes a decrease in E_{Se}. Although on one hand an increase in d_{Se} tends to increase g_{av} (Eq. 3), it also results in a simultaneous decrease in E_{Se} under a constant V_b. The overall effect is a decrease in g_{av} because of its additional exponential dependence on E_{Se} shown in Eq. 4. By substituting $E_{Se} = V_b/d_{Se}$ into Eq. 5 and differentiating both sides, we obtain:

$$\frac{1}{\ln g_{av}} \frac{\Delta g_{av}}{g_{av}} = \frac{\Delta d_{Se}}{d_{Se}} - \frac{\beta_2}{V_b} \Delta d_{Se} . \tag{13}$$

Eq. 13 can be rewritten as:

$$\frac{\Delta g_{av}}{g_{av}} = \ln(g_{av})(1 - \frac{\beta_2}{E_{Se}}) \frac{\Delta d_{Se}}{d_{Se}} . \tag{14}$$

Eq. 14 shows that with $\beta_2 > E_{Se}$, which is true for HARP, a positive change in d_{Se} results in a negative change in g_{av}. Eq. 14 also shows that the percentage variation in avalanche gain is proportional to $\ln(g_{av})$ and the percentage thickness variation, hence HARP layers operated with higher g_{av} are more susceptible to gain non-uniformity caused by thickness non-uniformity.

B. Calculation of Gain Non-uniformity

Using Eqs. 3 and 4, and the values for β_1 and β_2 determined in Section II, the variations in g_{av} were calculated for both positive and negative change in d_{Se} around 8 μm, and results are shown in Figure 14. Three V_b values of 840 V, 864 V and 880 V were used, which corresponds to g_{av} of 12, 25 and 46, respectively. Figure 14 shows that the slope of the curve, i.e. percentage change in g_{av}, is much higher for negative change in d_{Se}, which causes an increase in g_{av}, than it is for positive. Hence when choosing the bias potential V_b of HARP for a desired E_{Se}, the smallest d_{Se} for the entire detector area should be used, so that the variation in thickness is positive from the reference thickness. If we assume the smallest d_{Se} = 8 μm, the percentage changes in g_{av} due to an increase in d_{Se} of 1 % are 19 %, 23 % and 26 %, respectively, for the three V_b settings of 840 V, 864 V and 880 V. The change in g_{av} increases to 33 %, 40 %, and 44 %, respectively, when the variation in d_{Se} increases to 2 %. This range of g_{av} non-uniformity is certainly within the capability of gain correction and the dynamic range of the electronic circuits of FPI. With further increase in d_{Se} to 4 %, the value for g_{av} will decrease from the original setting of 46, 25 and 12 to 15, 10 and 6, respectively, which is a gain non-uniformity of 2 to 3 folds. Although the variation in g_{av} is significant, it is not expected to cause significant degradation in the DQE performance, as can be seen in the example of g_{av} = 46 and 12 shown in Figure 7 (a). However this will pose a greater challenge for the uniformity correction algorithm. Hence we can conclude that a thickness non-uniformity of 2 % is desirable for a HARP layer, and 4 % non-uniformity could still possibly be tolerated.

V. CONCLUSIONS

The feasibility of a new concept of indirect conversion flat-panel detector with avalanche gain is being investigated. The avalanche gain and quantum efficiency of an 8 μm thick HARP layer were investigated experimentally as function of E_{Se}. These characteristics of HARP were applied to a cascaded linear system to determine the optimal operating conditions required for x-ray imaging. Our results showed that by varying the avalanche gain between 2 and 46, x-ray quantum noise limited performance and a wide dynamic range can be obtained for both R/F and mammographic imaging applications. Direct x-ray interaction in HARP was shown not to affect the imaging performance. Due to the rapid increase in g_{av} as a function of E_{Se}, a small variation in d_{Se} can cause significant non-uniformity in avalanche gain. It is necessary to keep the thickness uniformity of a HARP layer within 4 %, which could maintain a high DQE across the entire detector and make the variation in g_{av} correctable using gain calibration.

ACKNOWLEDGEMENTS

We gratefully acknowledge financial support from the NIH (1 R01 EB002655-01) and the U.S. Army Breast Cancer Research Program (W81XWH-04-1-0554).

REFERENCES

[1] J.A. Rowlands and J. Yorkston, "Flat panel detectors for digital radiography," In: ***Medical Imaging. Volume 1 Physics and Psychophysics*, *Psychophysics*** Edited by: J Beutel, HL Kundel and RL Van Metter pp. 223-328. (SPIE, Bellingham, 2000).

[2] Wei Zhao and J. A. Rowlands, "Digital Radiology Using Active Matrix Readout of Amorphous Selenium: Theoretical Analysis of Detective Quantum Efficiency", Med. Phys. **24**, 1819-1833 (1997)

[3] L. E. Antonuk, K. –W. Jee, Y. El-Mohri, M. Maolinby, S. Nassif, X. Rong, Q. Zhao, J. H. Siewerdsen, R. A. Street and K. S. Shah, "Strategies to improve the signal and noise performance of active matrix, flat-panel imagers for diagnostic x-ray applications", Med. Phys. **27**, 289-306 (2000)

[4] J. H. Siewerdsen and D. A. Jaffray, "A ghost story: Spatio-temporal response characteristics of an indirect-detection flat-panel imager", Med. Phys. **26**, 1624-1641 (1999)

[5] M. Overdick, T. Solf and H. Wischmann, "Temporal artifacts in flat dynamic x-ray detectors", Proc. SPIE **4320**, 47-58 (2001)

[6] L. T. Niklason, B. T. Christian, L. E. Niklason, D. B. Kopans, *et.al.* "Digital tomosynthesis in breast imaging", Radiology **205**, 399-406 (1997)

[3] D. A. Jaffery and J. H. Siewerdsen, "Cone-beam computed tomography with a flat-panel imager: Initial performance characterization", Med. Phys. **27**, 1311-1323 (2000)

[8] Biao Chen and Ruola Ning, "Cone-beam volume CT breast imaging: Feasibility study", Med. Phys. **29**, 755-770 (2002)

[9] A. Koch, J-M Macherel, T. Wirth, P. de Groot, T. Ducourant, D. Couder, J-P Moy, E. Calais, "Detective quantum efficiency of an x-ray image intensifier chain as a benchmark for amorphous silicon flat panel detectors", Proc. SPIE **4320**, 115-120 (2001)

[10] S. Vedantham, A. Karellas, S. Suryanarayanan, D. Albagli, S. Han, E. J. Tkaczyk, C. E. Landberg, P. R. Granfors, I. Levis, C. J. D'Orsi and R. E. Hendrick, "Full breast digital mammography with an amorphous silicon-based flat-panel detector: Physical characteristics of a clinical prototype", Med. Phys. **27**, 558-567 (2000)

[11] Wei Zhao, W. G. Ji, Anne Debrie and J. A. Rowlands, "Imaging performance of amorphous selenium based flat-panel detectors for digital mammography: Characterization of a small area prototype detector", Med. Phys. **30**, 254-263 (2003)

[12] R. A. Street, S. E. Ready, K. Van Schuylenbergh, J. Ho, J. B. Boyce, P. Nylen, K. Shah, L. Melekhov and H. Hermon, "Comparison of PbI_2 and HgI_2 for direct detection active matrix x-ray image sensors", J. Appl. Phys. **91**, 3345-3355 (2002)

[13] M. Zahangir Kabir and S. O. Kasap, "Charge collection and absorption-limited sensitivity of x-ray photoconductors: Applications to a-Se and HgI_2", Appl. Phys. Lett. **80**, 1664-1666 (2002)

[14] N. Matsuura, Wei Zhao, Z. Huang and J. A. Rowlands, "Digital radiology using active matrix readout: Amplified pixels for fluoroscopy", Med. Phys. **26**, 672-681 (1999)

[15] K. S. Karim, Y. K. Vygranenko, D. A. Striakhilev, A. Nathan, S. Germann, J. A. Rowlands, G. Belev, C. Koughia, R. Johanson and S. O. Kasap, "Active pixel image sensor for large-area medical imaging", Proc. SPIE **5030**, 38-47 (2003)

[16] J.P. Lu, K. Van Schuylenbergh, J. Ho, Y. Wang, J. B. Boyce, and R. A. Street, "Flat panel imagers with pixel level amplifiers based on polycrystalline silicon thin-film transistor technology", Appl. Phys. Lett., **80**, 4656 (2002)

[17] K. Tanioka, J. Yamazaki, K. Shidara, K. Taketoshi, T. Kawamura, T. Hirai and Y. Takasaki, "Avalanche-mode amorphous selenium photoconductive target camera tube", Adv. Electron. Electron Phys. **74**, 379-387 (1988)

[18] H. M. Rougeot and G. E. Possin, "Radiation image detector with optical gain selenium photosensors", United States Patent 5,198,673.

[19] A. Jean, L. Laperriere, A. Legros, H. Mani, Z. Shukri and H. Rougeot, "New cesium iodide-selenium x-ray detector structure for digital radiography and fluoroscopy", Proc. SPIE **3659**, 298-306 (1999)

[20] T. Ohshima, K. Tsuji, K. Sameshima, T. Hirai, K. Shidara and K. Taketoshi, "Excess noise in amorphous selenium avalanche photodiodes", Japan. J. Appl. Phys. **30**, L1071-L1074 (1991)

[21] Wei Zhao, D. C. Hunt, Kenkichi Tanioka and J. A. Rowlands, "Indirect flat-panel detectors with avalanche gain", Proc. SPIE **5368**, 150-161 (2004)

[22] D. M. Pai and R. C. Enck, "Onsager mechanism of photogeneration in amorphous selenium", Phys. Rev. B **11**, 5163-5174 (1975)

[23] K. Tsuji, Y. Takasaki, T. Hiri, J. Yamazaki and K. Tanioka, "Avalanche phenomenon in amorphous selenium", Optoelectron. Devices Technol., **9**, 367-378 (1994)

[24] R. J. McIntyre, "Multiplication noise in uniform avalanche diodes", IEEE Trans. Electron Devices, **13**, 164-168 (1966)

[25] D. C. Hunt, Wei Zhao and J. A. Rowlands, "X-ray imaging using amorphous selenium: Excess avalanche multiplication noise in indirect flat-panel detectors", Med. Phys., to be submitted.

[26] W Zhao, G Ristic and JA Rowlands, "Inherent imaging performance of cesium iodide scintillators", Med. Phys. **31**, 2594-2605 (2004)

[27] Wei Zhao, J. Law, D. Waechter, Z. Huang and J. A. Rowlands, "Digital radiology using active matrix readout of amorphous selenium: Detectors with high voltage protection", Med. Phys. **25**, 539-549 (1998).

[28] A. Koch, "Influence of optical gaps on signal and noise properties of luminescent screen x-ray detectors", Proc. SPIE **5368**, 221-225 (2004)

[29] D. C. Hunt, S. S. Kirby and J. A. Rowlands, "X-ray imaging with amorphous selenium: X-ray to charge conversion gain and avalanche multiplication", Med. Phys. **29**, 2464-2471 (2002)

[30] D. C. Hunt, B. Lui and J. A. Rowlands, "An experimentally validated theoretical model of avalanche multiplication x-ray noise in amorphous selenium", Proc. SPIE **3977**, 106-116 (2000)

Table I: SHARP-AMFPI detector design parameters and operating conditions chosen for different x-ray imaging applications.

	Mammography detector		R/F detector	
	tomosynthesis	screening	Fluoroscopy	radiography
Pixel pitch a_p (μm)	70		200	
X-ray spectrum	28 kVp Mo/Mo, 4cm PMMA		RQA5	
Electronic noise	2000 electrons		1500 electrons	
CsI (75% packing)	150 μm HR		600 μm HL	
W for CsI (eV)	30		18	
α	0.8		0.8	
Minimum exposure	0.1 mR	1 mR	0.1 μR	30 μR
E_{Se} (V/μm)	110	105	110	95
η	0.36	0.35	0.36	0.31
g_{av}	46	12	46	2.3

Figure Caption

Figure 1: (a) Diagram showing the concept of SHARP-AMFPI, where an avalanche photoconductor is used to detector light photons generated by CsI. (b) Side view showing the multilayer structure of the detector (thickness not drawn to scale).

Figure 2: Experimental apparatus for measuring the photosensitivity of HARP.

Figure 3: Measured effective quantum efficiency η^* as a function of E_{Se} for an 8 μm thick HARP layer.

Figure 4: The optical quantum efficiency of a-Se calculated using Onsager theory and $r_0 = 1.7$ nm, compared with the measured effective quantum efficiency η^* at $\lambda = 540$ nm.

Figure 5: (a) Solid circles are the g_{av} for the 8 μm HARP layer calculated by dividing the measured η^* at 540 nm by the optical η predicted by the Onsager theory using $r_0 = 1.7$ nm. The solid line shows the g_{av} calculated using the fitted β_1 and β_2 values. (b) The plot of $\ln(\ln(g_{av}))$ as a function of $1/E_{Se}$, and the best linear fit for the data.

Figure 6: Flow diagram showing the serial and parallel stages of the cascaded linear system model for SHARP-AMFPI.

Figure 7: Calculated DQE(f) using the detector parameters and operating conditions shown in Table I for a fluoroscopy detector at the x-ray exposure level of: (a) 0.1 μR; and (b) 30 μR.

Figure 8: The calculated image charge on each pixel of the detector and the corresponding avalanche gain as a function of x-ray exposure for the detector operational setting of: (a) fluoroscopy; and (b) radiography.

Figure 9: Calculated DQE(f) using the detector parameters and operating conditions shown in Table I for mammography: (a) tomosynthesis with minimum exposure of 0.1 mR; and (b) screening with minimum exposure of 1 mR.

Figure 10: The calculated image charge on each pixel of the mammography detector and the corresponding avalanche gain as a function of x-ray exposure with or without the addition of a pixel

storage capacitor. The results are for detector operating conditions chosen for: (a) tomosynthesis image acquisition; and (b) screening mammography.

Figure 11: Diagram showing the depth dependent gain for direct x-ray interaction in HARP. For the x-rays absorbed in CsI, the light photons created enter the top interface of HARP, where holes are generated and undergo avalanche multiplication for the entire thickness of HARP d_{Se}. For the x-rays interacting directly with HARP at depth x from the top interface, the holes generated undergo avalanche for the thickness of $(d_{Se} - x)$, which causes depth dependence avalanche gain variation.

Figure 12: Comparison of the presampling signal and NPS (before pixel aperture function) due to x-ray absorbed in CsI and direct x-ray interaction in HARP: (a) signal spectra, where the signal due to direct interaction is negligible; and (b) NPS, where the NPS due to direct interaction under the Nyquist frequency of 2.5 cycles/mm is negligible.

Figure 13: Comparison between the DQE of SHARP-AMFPI with and without consideration of direct x-ray interaction in HARP.

Figure 14: The avalanche gain g_{av} calculated as a function of the thickness of HARP, which varies around 8 μm, under a constant bias potential V_b of 840, 864 and 880 V.

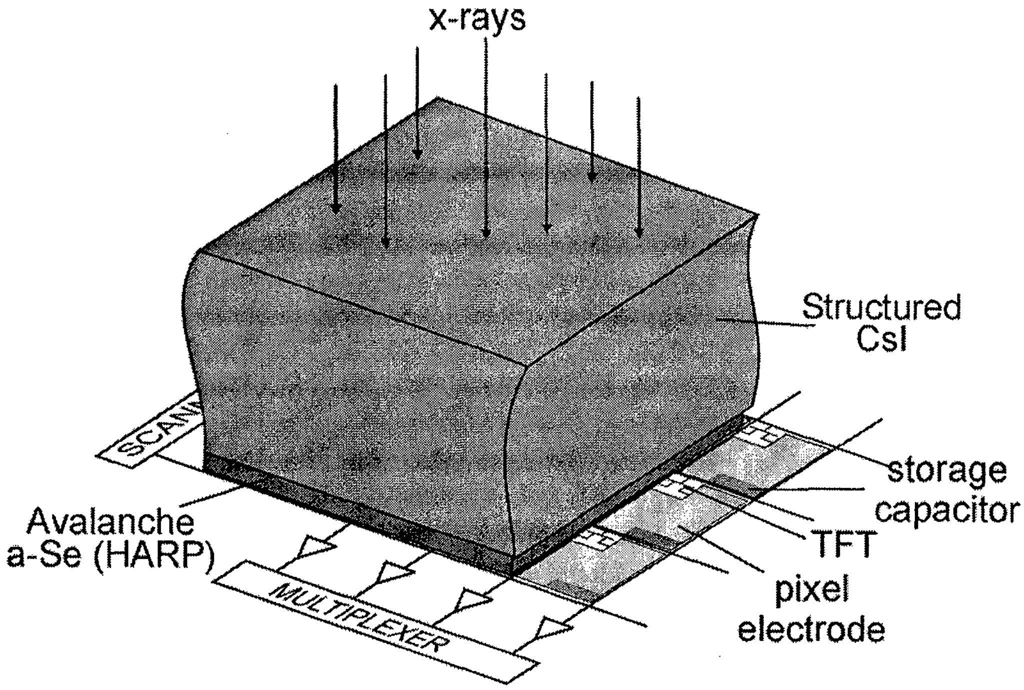
x-rays
Structured CsI
SCAN
storage capacitor
TFT
pixel electrode
Avalanche a-Se (HARP)
MULTIPLEXER

(a)

FIG. 1 (a)

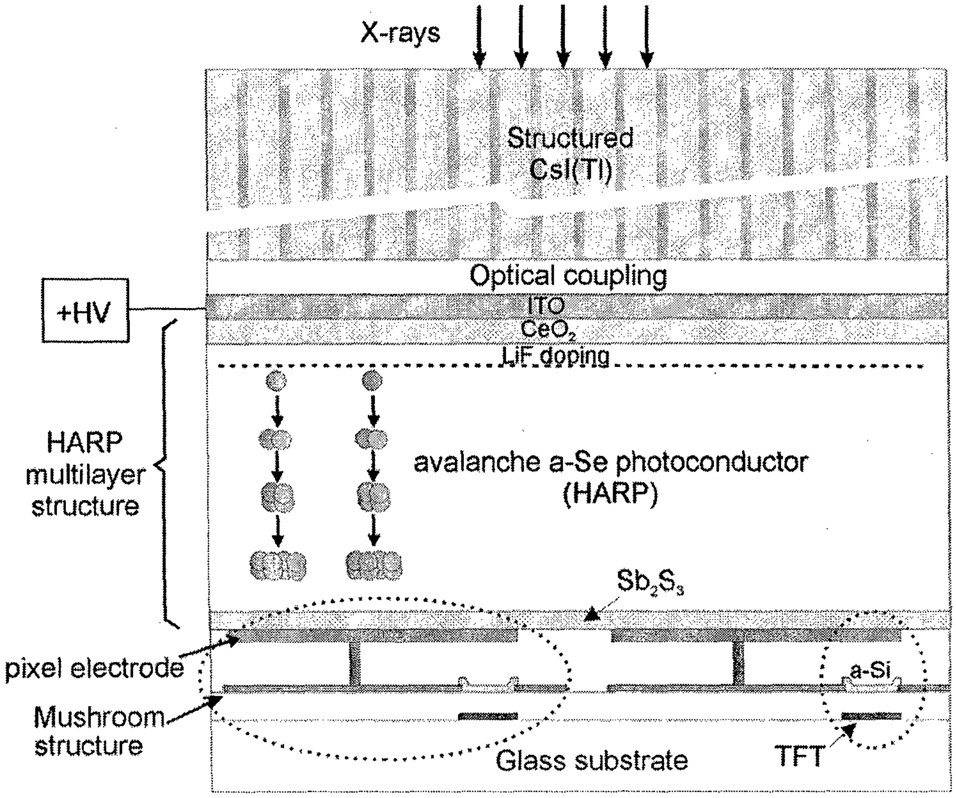
X-rays
Structured
CsI(Tl)
Optical coupling
+HV
ITO
CeO_2
LiF doping
HARP
multilayer
structure
avalanche a-Se photoconductor
(HARP)
Sb_2S_3
pixel electrode
a-Si
Mushroom
structure
Glass substrate
TFT

(b)

FIG. 1 (b)

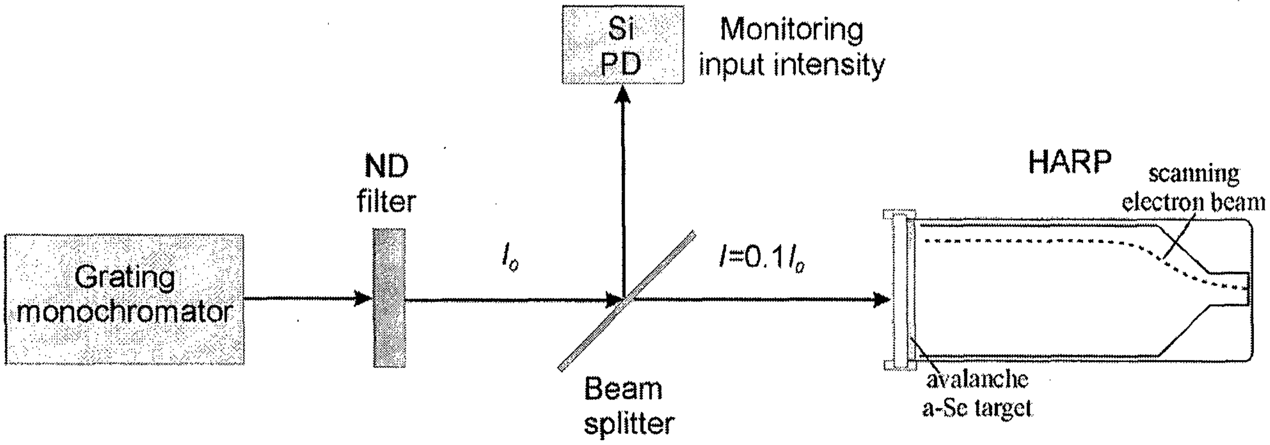

Figure 2: Experimental apparatus for measuring the photosensitivity of HARP.

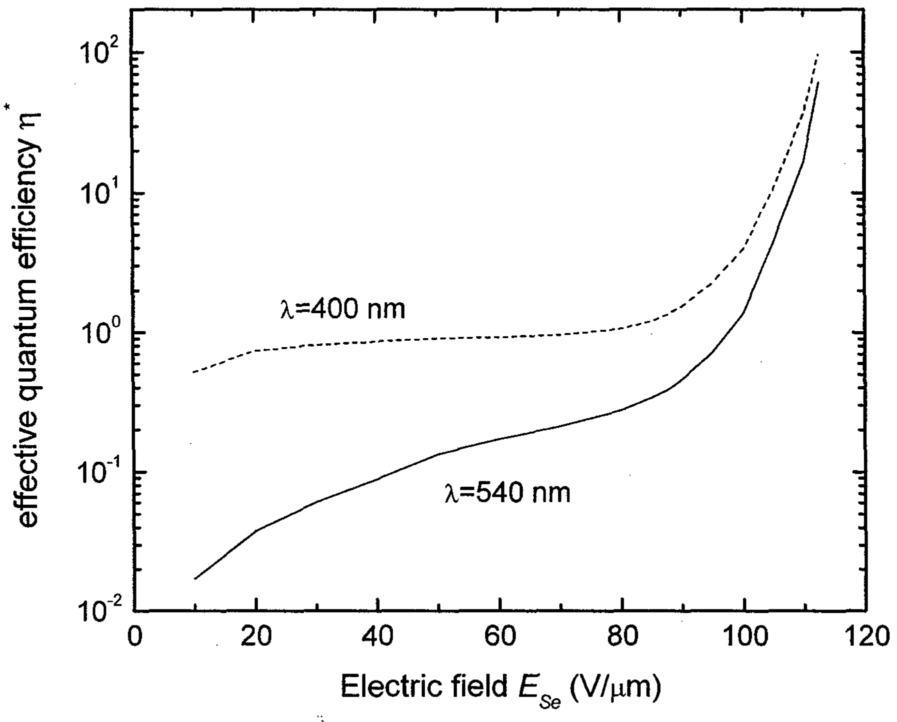

Figure 3: Measured effective quantum efficiency η^* as a function of E_{Se} for an 8 μm thick HARP layer.

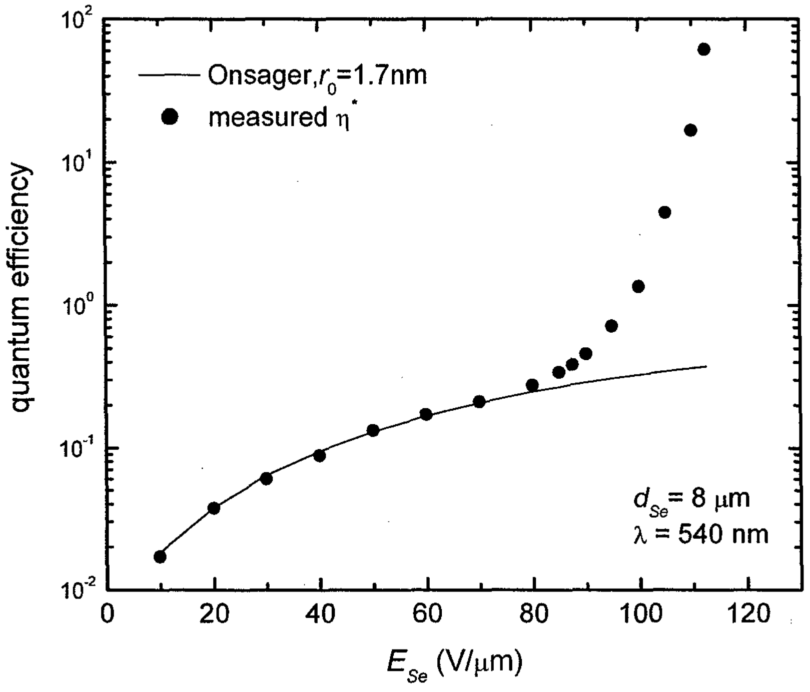

Figure 4: The optical quantum efficiency of a-Se calculated using Onsager theory and $r_0 = 1.7$ nm, compared with the measured effective quantum efficiency η^* at $\lambda = 540$ nm.

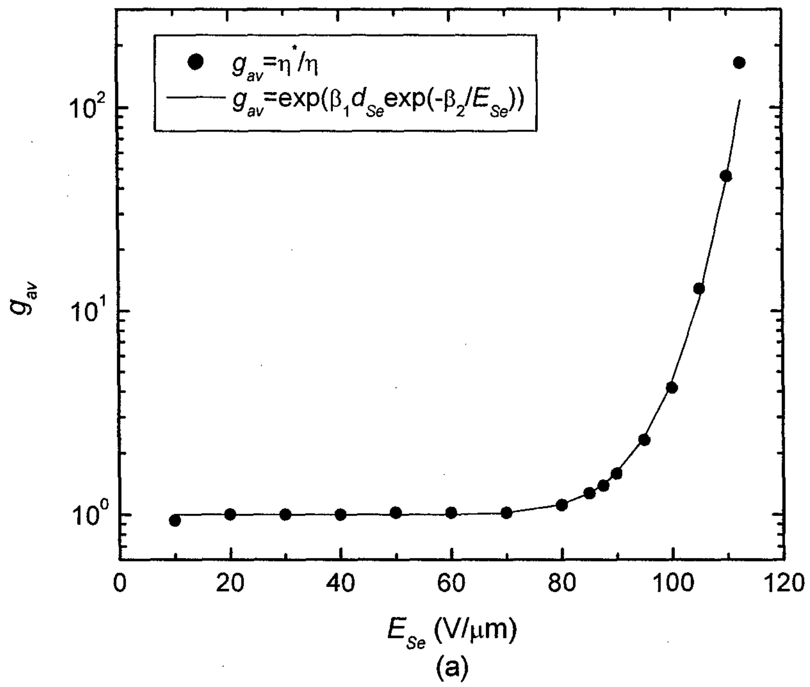
● $g_{av}=\eta^*/\eta$
— $g_{av}=\exp(\beta_1 d_{Se}\exp(-\beta_2/E_{Se}))$
10^2
10^1
10^0
g_{av}
0
20
40
60
80
100
120
E_{Se} (V/μm)
(a)

FIG. 5 (a)

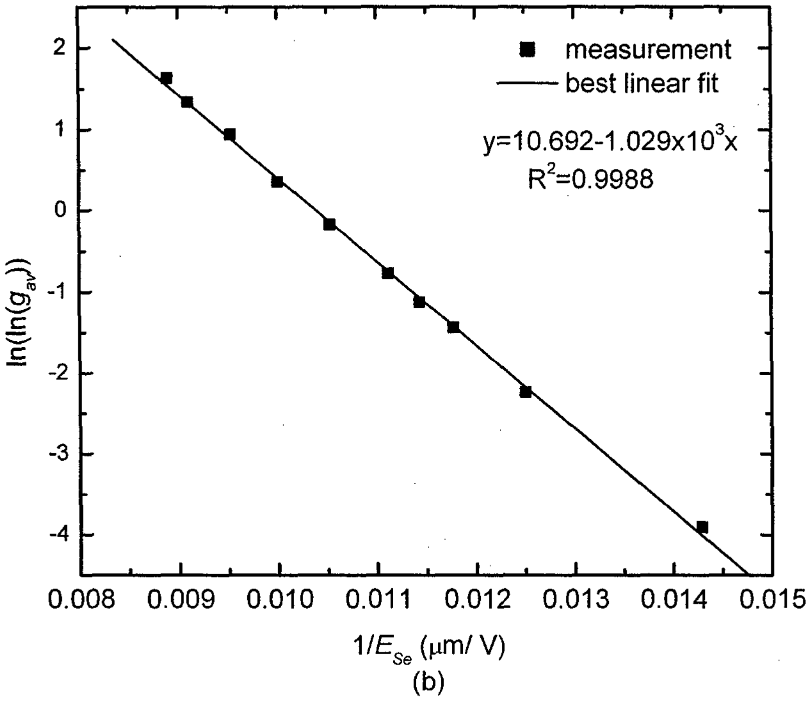

■ measurement
—— best linear fit
y=10.692-1.029x10^{3}x
R^2=0.9988
ln(ln(g_{av}))
2
1
0
-1
-2
-3
-4
0.008
0.009
0.010
0.011
0.012
0.013
0.014
0.015
1/E_{Se} (μm/ V)
(b)

FIG. 5 (b)

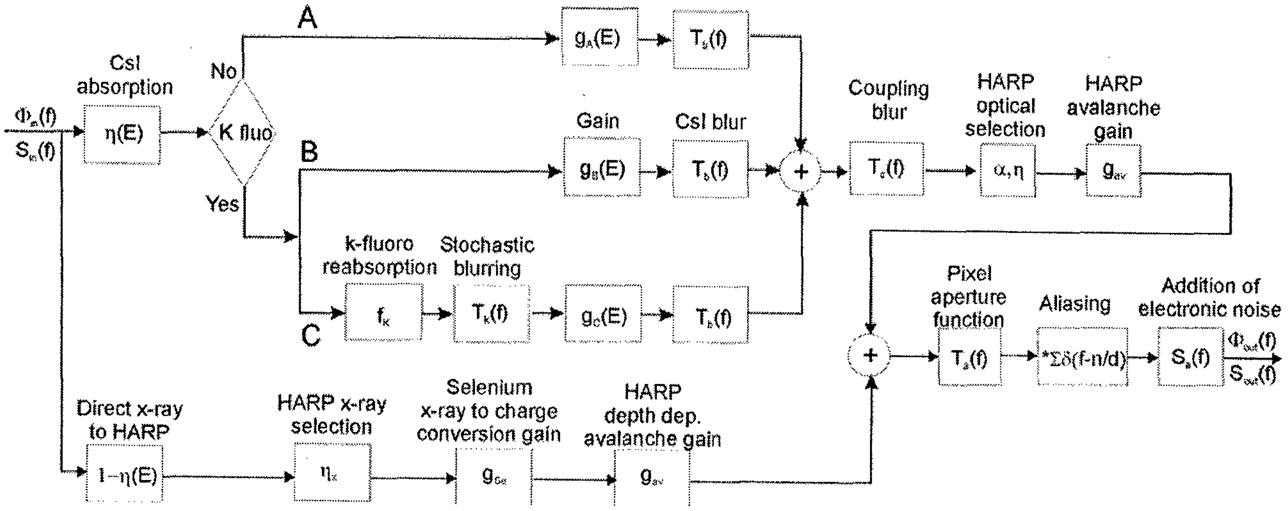A
$g_A(E)$
$T_b(f)$
CsI absorption
No
$\Phi_{in}(f)$
$S_{in}(f)$
$\eta(E)$
K fluo
Gain
CsI blur
Coupling blur
HARP optical selection
HARP avalanche gain
B
$g_B(E)$
$T_b(f)$
+
$T_c(f)$
α, η
g_{av}
Yes
k-fluoro reabsorption
Stochastic blurring
f_K
$T_K(f)$
$g_C(E)$
$T_b(f)$
C
Pixel aperture function
Aliasing
Addition of electronic noise
+
$T_a(f)$
$*\Sigma\delta(f-n/d)$
$S_e(f)$
$\Phi_{out}(f)$
$S_{out}(f)$
Direct x-ray to HARP
HARP x-ray selection
Selenium x-ray to charge conversion gain
HARP depth dep. avalanche gain
$1-\eta(E)$
η_x
g_{Se}
g_{av}

FIG. 6

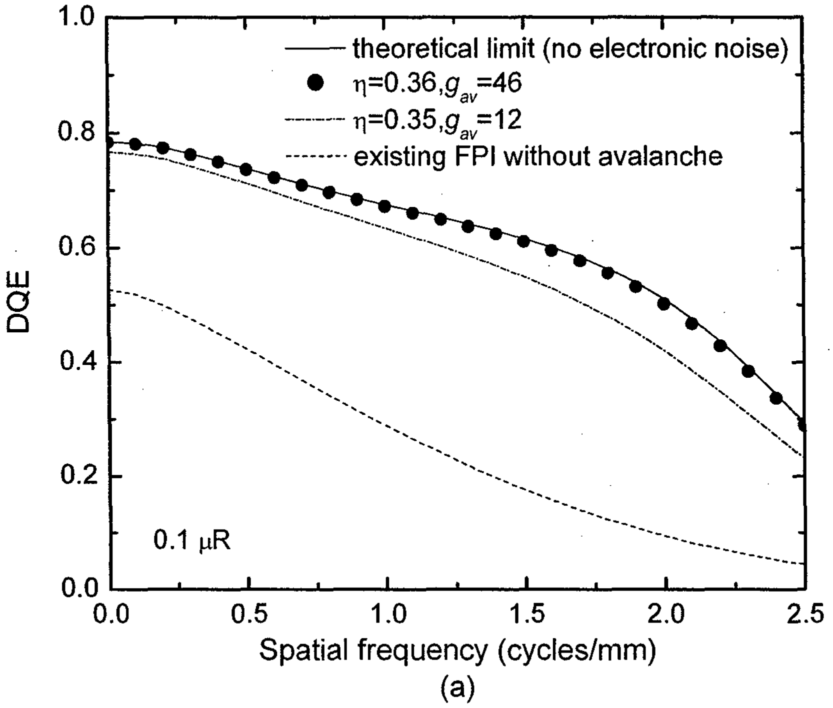

1.0
0.8
0.6
0.4
0.2
0.0
DQE
0.0
0.5
1.0
1.5
2.0
2.5
Spatial frequency (cycles/mm)
(a)
theoretical limit (no electronic noise)
η=0.36,g_av=46
η=0.35,g_av=12
existing FPI without avalanche
0.1 μR

FIG. 7 (a)

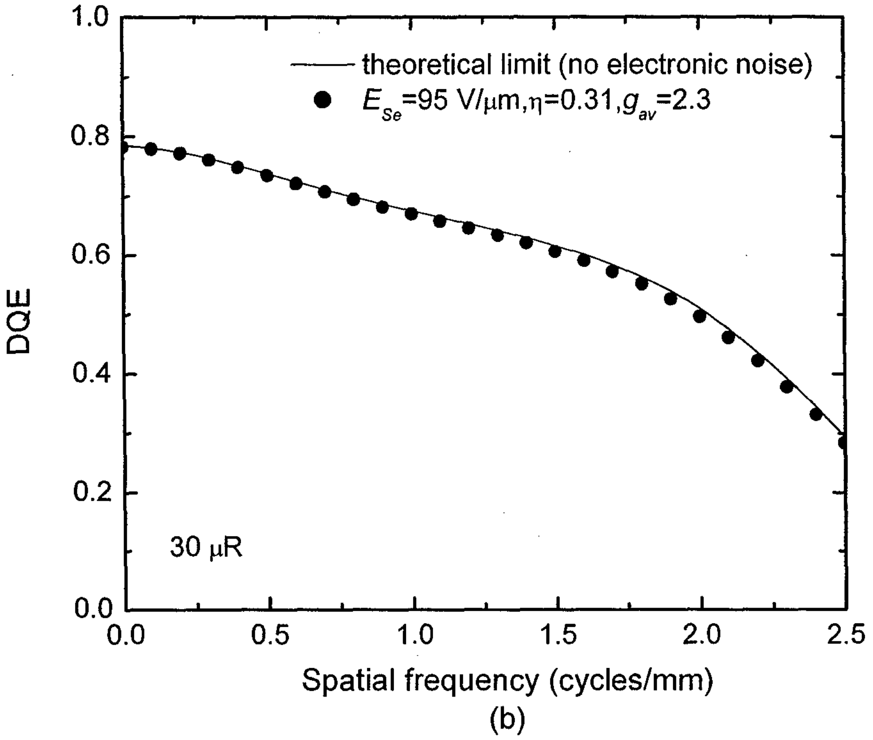

1.0
0.8
0.6
0.4
0.2
0.0
DQE
theoretical limit (no electronic noise)
● E_{Se}=95 V/μm,η=0.31,g_{av}=2.3
30 μR
0.0
0.5
1.0
1.5
2.0
2.5
Spatial frequency (cycles/mm)
(b)

FIG. 7 (b)

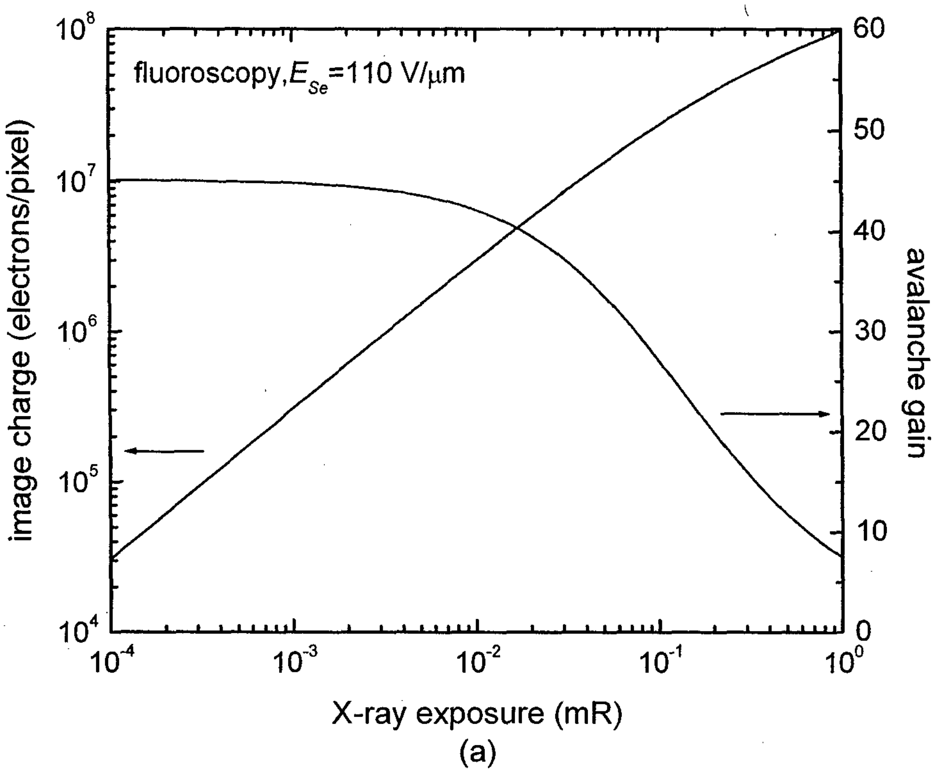
fluoroscopy,E_{Se}=110 V/μm
image charge (electrons/pixel)
avalanche gain
X-ray exposure (mR)
10^4
10^5
10^6
10^7
10^8
0
10
20
30
40
50
60
10^{-4}
10^{-3}
10^{-2}
10^{-1}
10^0
(a)

FIG. 8 (a)

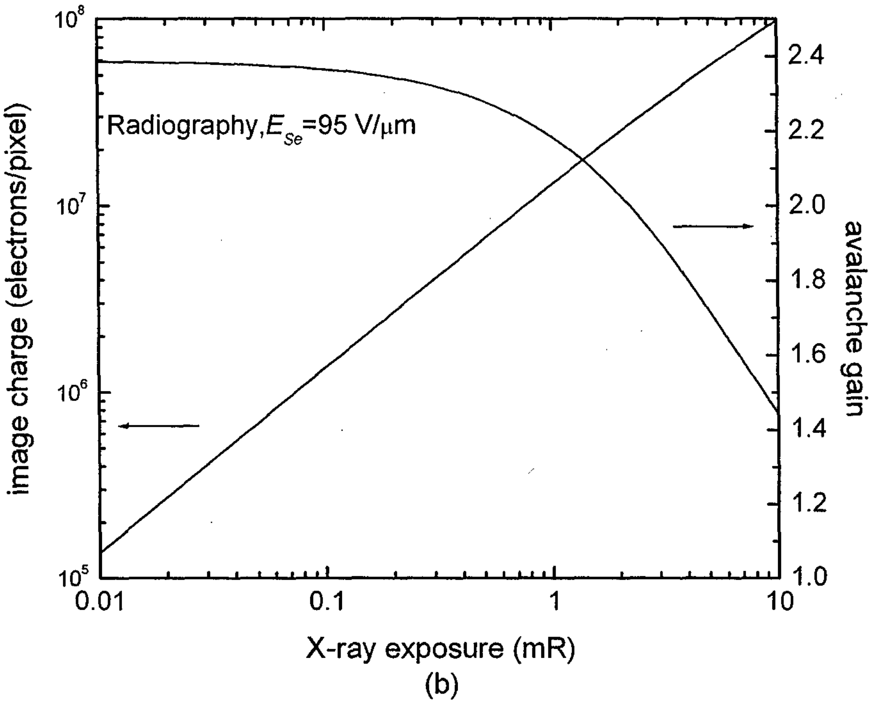

Radiography, E_{Se}=95 V/μm
image charge (electrons/pixel)
avalanche gain
X-ray exposure (mR)
(b)
10^8
10^7
10^6
10^5
0.01
0.1
1
10
2.4
2.2
2.0
1.8
1.6
1.4
1.2
1.0

FIG. 8 (b)

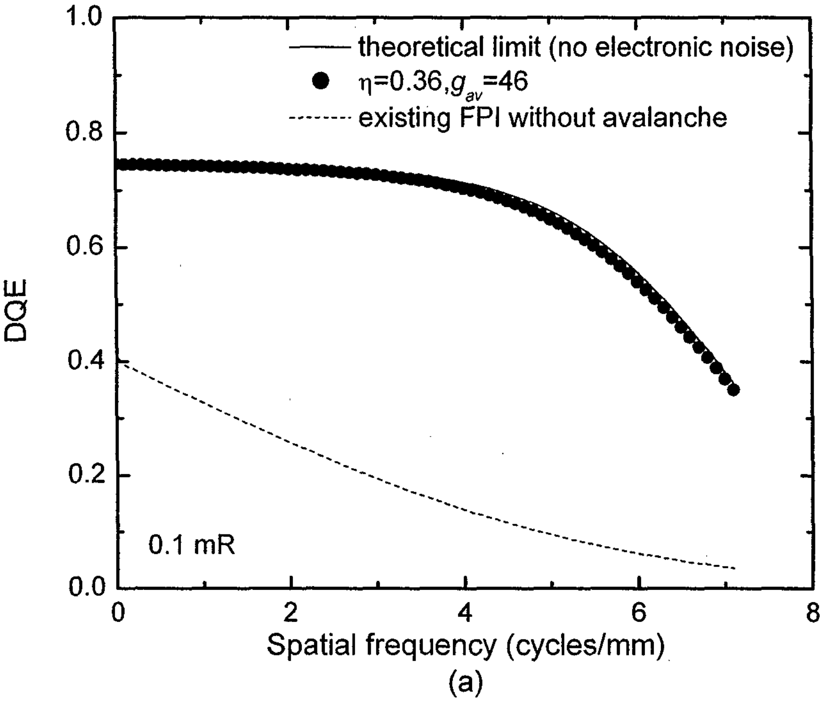
1.0
0.8
0.6
0.4
0.2
0.0
DQE
0
2
4
6
8
Spatial frequency (cycles/mm)
(a)
theoretical limit (no electronic noise)
● η=0.36,g_{av}=46
existing FPI without avalanche
0.1 mR

FIG. 9 (a)

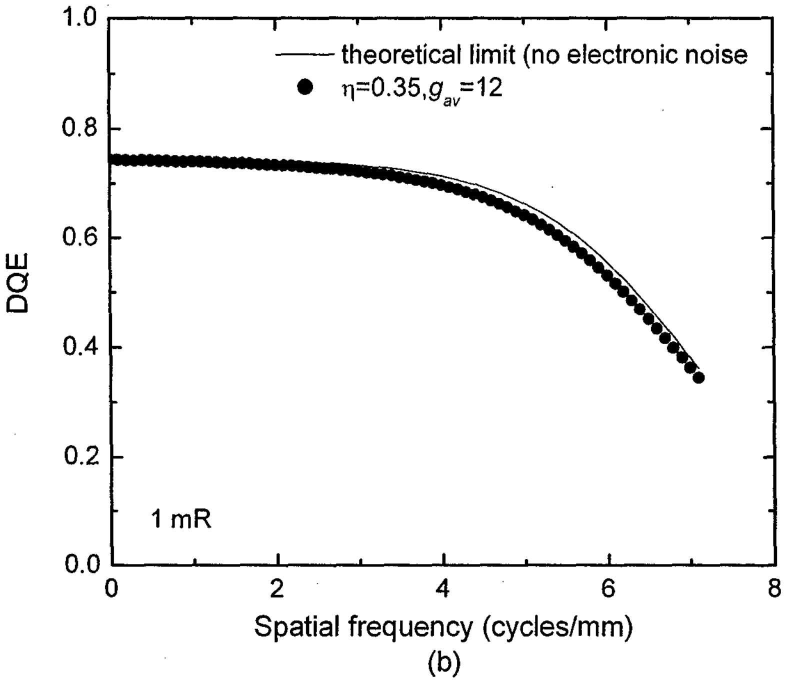

1.0
0.8
0.6
0.4
0.2
0.0
DQE
theoretical limit (no electronic noise
● η=0.35,g_{av}=12
1 mR
0
2
4
6
8
Spatial frequency (cycles/mm)
(b)

FIG. 9 (b)

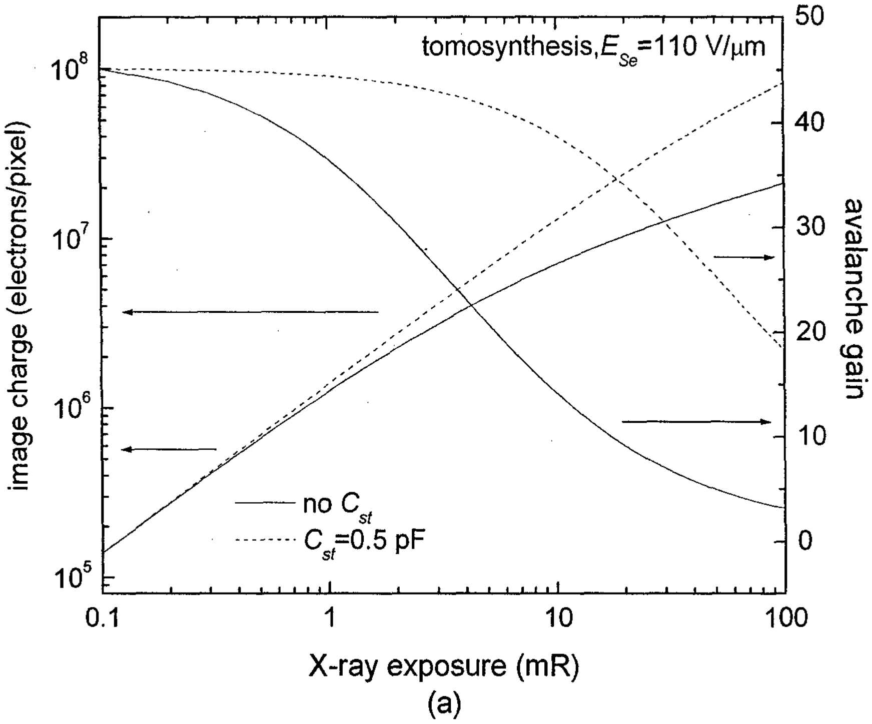
tomosynthesis, E_{Se}=110 V/μm
image charge (electrons/pixel)
avalanche gain
10^8
10^7
10^6
10^5
50
40
30
20
10
0
0.1
1
10
100
X-ray exposure (mR)
no C_{st}
C_{st}=0.5 pF
(a)

FIG. 10 (a)

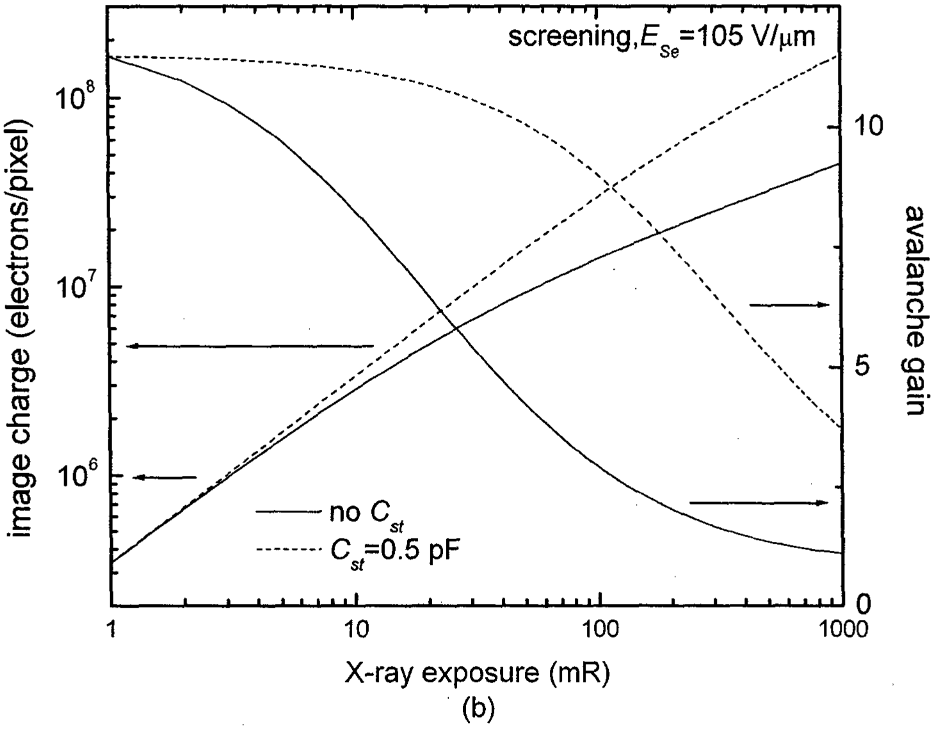

screening, E_{Se}=105 V/μm
image charge (electrons/pixel)
10^8
10^7
10^6
avalanche gain
10
5
0
no C_{st}
C_{st}=0.5 pF
1
10
100
1000
X-ray exposure (mR)
(b)

Figure 10 (b)

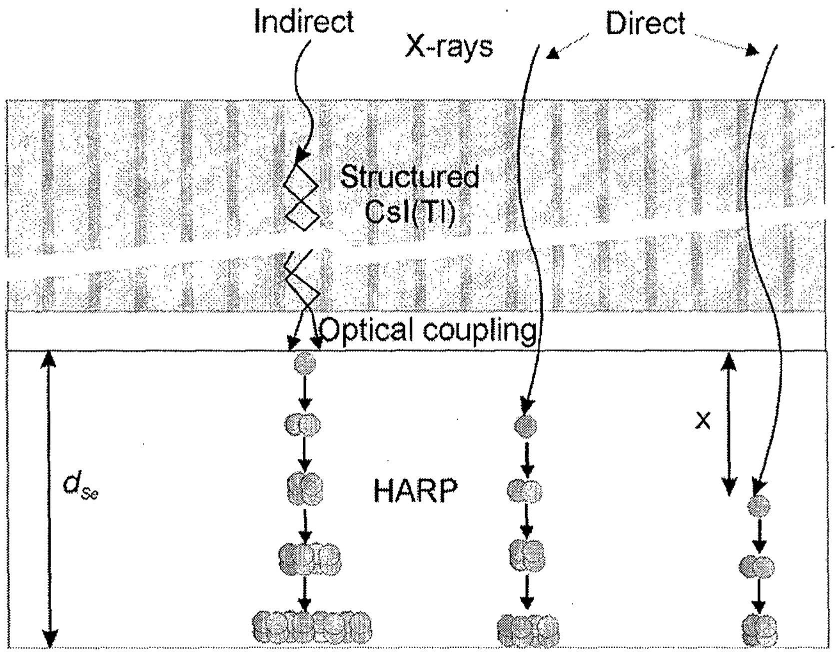
Indirect
X-rays
Direct
Structured
CsI(Tl)
Optical coupling
d_{Se}
HARP
x

FIG. 11

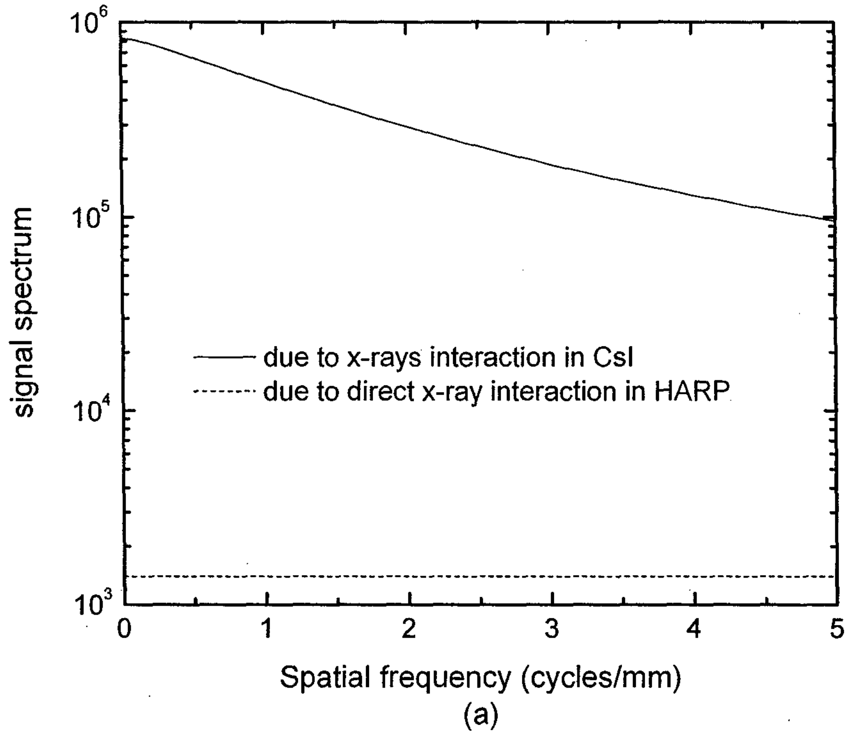

10^6
10^5
10^4
10^3
signal spectrum
due to x-rays interaction in CsI
due to direct x-ray interaction in HARP
0
1
2
3
4
5
Spatial frequency (cycles/mm)
(a)

FIG. 12 (a)

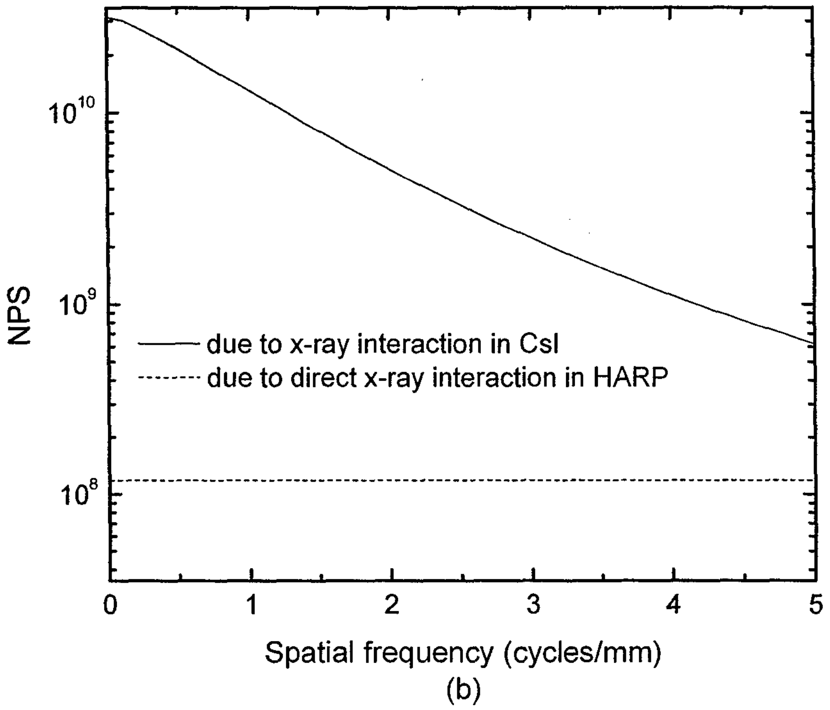
NPS
10^{10}
10^9
10^8
due to x-ray interaction in CsI
due to direct x-ray interaction in HARP
0
1
2
3
4
5
Spatial frequency (cycles/mm)
(b)

FIG. 12 (b)

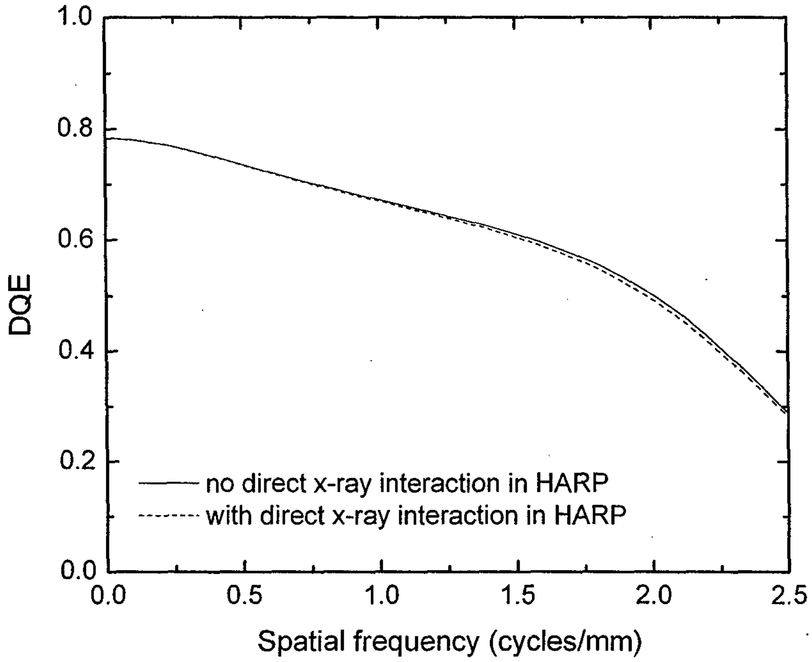
1.0
0.8
0.6
0.4
0.2
0.0
DQE
0.0
0.5
1.0
1.5
2.0
2.5
Spatial frequency (cycles/mm)
no direct x-ray interaction in HARP
with direct x-ray interaction in HARP

FIG. 13

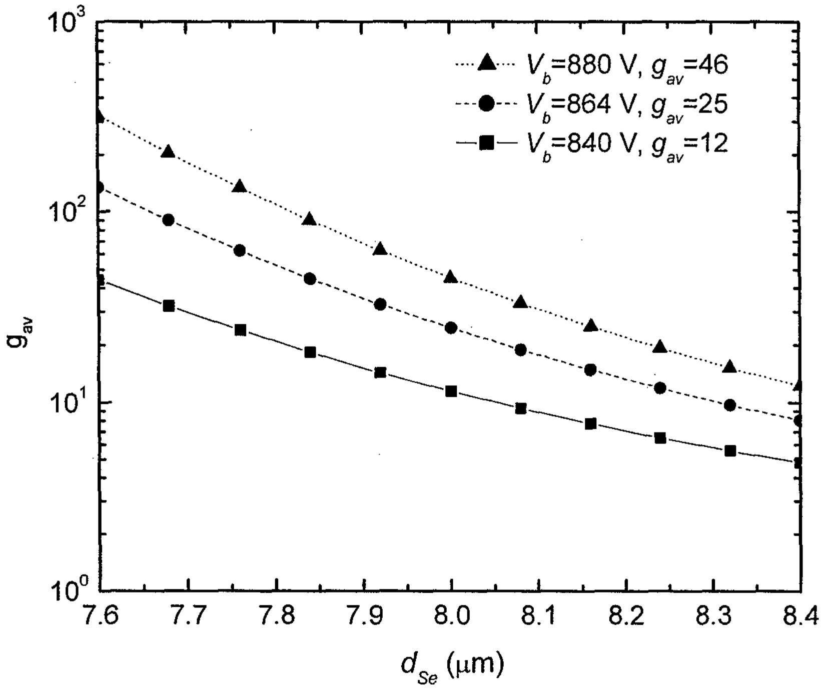

10^3
10^2
10^1
10^0
g_{av}
V_b=880 V, g_{av}=46
V_b=864 V, g_{av}=25
V_b=840 V, g_{av}=12
7.6
7.7
7.8
7.9
8.0
8.1
8.2
8.3
8.4
d_{Se} (μm)

FIG. 14